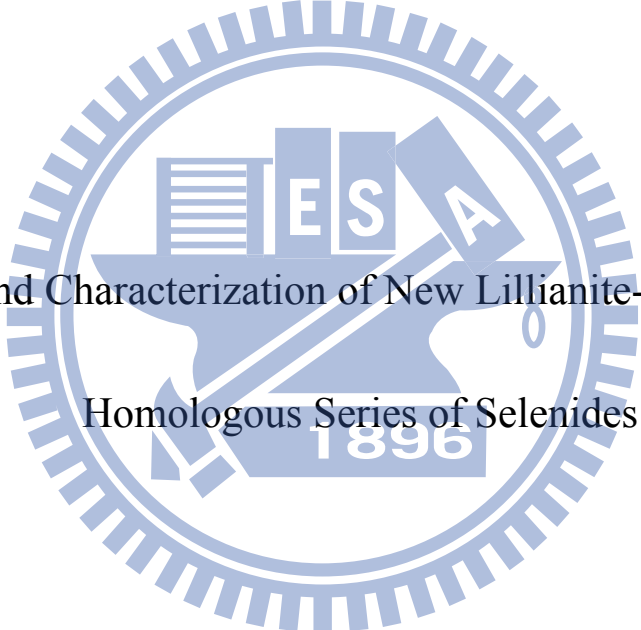


國立交通大學

應用化學研究所

博士論文

新穎四元硫鉍鉛礦型結構硒化物的合成與特性鑑定



Synthesis and Characterization of New Lillianite-type Quaternary
Homologous Series of Selenides

研究生：陳奎伯

指導教授：李積琛 博士

中華民國九十九年五月

新穎四元硫鉍鉛礦型結構硒化物的合成與特性鑑定

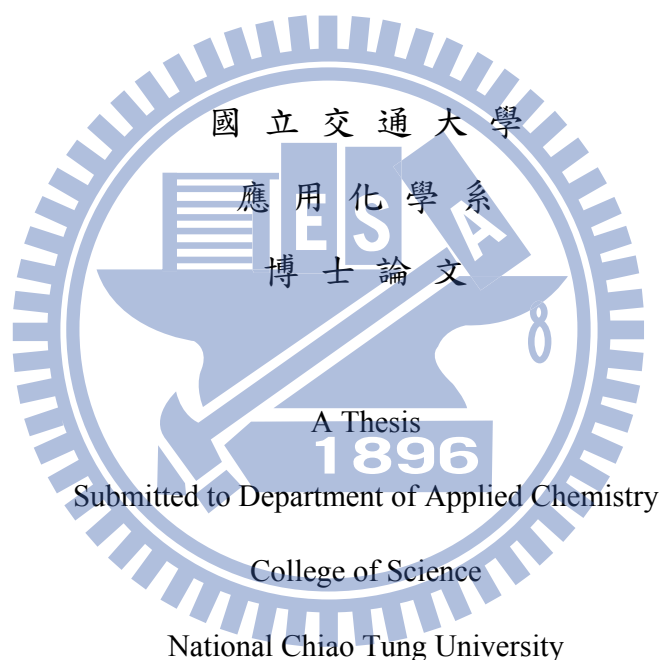
Synthesis and Characterization of New Lillianite-type Quaternary
Homologous Series of Selenides

研究生：陳奎伯

Student : Kuei-Bo Chen

指導教授：李積琛

Advisor : Chi-Shen Lee



in partial Fulfillment of the Requirements

for the Degree of

Doctor of Philosophy

in

Applied Chemistry

May 2010

Contents	Page
Chinese Abstract	vi
English Abstract	viii
Acknowledgments	x
List of Tables	xi
List of Figures	xiv
Chapter 1 Introduction	1
1.1. Thermoelectric materials	1
1.2. Homologous series	9
1.3 Motivation and goal of this thesis	12
Chapter 2	14
Experimental and Theoretical Studies of $\text{Sn}_{3-\delta}\text{Pb}_\delta\text{Bi}_2\text{Se}_6$ ($\delta = 0.0 - 0.7$)	
2.1 Experiments	15
2.1.1 Synthesis	15
2.1.2 Single-crystal X-ray Diffraction (XRD)	16
2.1.3 Characterization	25
2.1.4 Physical Property Measurements	25
2.1.5 Theoretical Calculations	26
2.2 Results and Discussion	27
2.2.1 Crystal Structure	27
2.2.2 Electronic Structure	31
2.2.3 Physical Properties	34
2.2.4 Thermoanalysis	35
2.3 Conclusions	37
Chapter 3	38
Experimental and Theoretical Studies of $(\text{Pb}_x\text{Sn}_{1-x})_6\text{Bi}_2\text{Se}_9$ ($x = 0 - 4.36$)	
3.1 Experiments	39
3.1.1 Synthesis	39
3.1.2 Single-crystal X-ray diffraction (XRD)	39
3.1.3 Characterization	42

3.1.4 Physical Property Measurements	43
3.1.5 Calculation of the Electronic Structure	43
3.2 Results and Discussion	44
3.2.1 Synthesis and Structure Analysis	44
3.2.2 Crystal Structure	48
3.2.3 Electronic Structure	50
3.2.4 Physical Properties	52
3.2.5 Thermoanalysis	54
3.3 Conclusions	55
Chapter 4 Synthesis and Characterization of Quaternary Selenides	56
$\text{Sn}_2\text{Pb}_5\text{Bi}_4\text{Se}_{13}$ and $\text{Sn}_{8.65}\text{Pb}_{0.35}\text{Bi}_4\text{Se}_{15}$	
4.1 Experiments	57
4.1.1 Synthesis	57
(a) $\text{Sn}_2\text{Pb}_5\text{Bi}_4\text{Se}_{13}$	57
(b) $\text{Sn}_{8.65}\text{Pb}_{0.35}\text{Bi}_4\text{Se}_{15}$	58
4.1.2 Single-crystal X-ray diffraction (XRD)	60
(a) $\text{Sn}_2\text{Pb}_5\text{Bi}_4\text{Se}_{13}$	60
(b) $\text{Sn}_{8.65}\text{Pb}_{0.35}\text{Bi}_4\text{Se}_{15}$	61
4.1.3 Characterization	64
4.1.4 Calculation of the Electronic Structure	65
4.1.5 Physical Property Measurements	65
4.2 Results and Discussion	66
4.2.1 Description of the structure	66
(a) $\text{Sn}_2\text{Pb}_5\text{Bi}_4\text{Se}_{13}$	66
(b) $\text{Sn}_{8.65}\text{Pb}_{0.35}\text{Bi}_4\text{Se}_{15}$	67
4.2.2 Electronic Structure	69
(a) $\text{Sn}_2\text{Pb}_5\text{Bi}_4\text{Se}_{13}$	69
(b) $\text{Sn}_{8.65}\text{Pb}_{0.35}\text{Bi}_4\text{Se}_{15}$	70
4.2.3 Physical Properties	73
4.2.3 Thermoanalysis	73
4.3 Conclusions	76
Chapter 5 Synthesis and Characterization of Quaternary Selenides	77

$\text{Pb}_{12.92}\text{Sb}_{2.08}\text{Bi}_2\text{Se}_{19}$	
5.1 Experiments	78
5.1.1 Synthesis	78
5.1.2 Single-crystal X-ray diffraction (XRD)	79
5.1.3 Characterization	83
5.1.4 Physical Property Measurements	84
5.1.5 Calculation of the Electronic Structure	84
5.2 Results and Discussion	85
5.2.1 Crystal structure	85
5.2.2 Electronic Structure	87
5.2.3 Physical Properties	88
5.2.4 Thermoanalyses	89
5.3 Conclusions	90
Chapter 6 Synthesis and Characterization of Quaternary Selenides	91
$\text{Sn}_4\text{Bi}_{10}\text{Se}_{19}$ and $\text{Sn}_{8.5}\text{Pb}_{1.5}\text{Bi}_{18}\text{Se}_{37}$	
Synthesis	92
Single-crystal X-ray diffraction (XRD)	93
Structure description	98
Chapter 7 Conclusions	99
References	101
Appendix	105

新穎四元硫鉍鉛礦型結構硒化物的合成與特性鑑定

學生：陳奎伯

指導教授：李積琛 博士

國立交通大學應用化學研究所

摘要

我們使用固態燒合成四元鉍鉛礦型結構硒化物，藉由單晶繞射解析並研究其晶體結構。利用能帶計算與物理性質量測來證明這類化合物均具有半導體性質。

在第一部份中合成出具有相寬的四元化合物 $\text{Sn}_{3-x}\text{Pb}_x\text{Bi}_2\text{Se}_6$ ($x = 0 - 0.7$)，此結構為 *Pnma* (No. 62) 空間群之斜方晶系，與礦物中的硫鉍鉛礦 $\text{Pb}_3\text{Bi}_2\text{S}_6$ (Lillinite) 的結構相似。差異在於接近 trochochemical cell-twinning 面上之原子並非呈現鏡面對稱，而是滑動對稱。單晶結果顯示，當鉛的含量增加時，原子逐漸往 trochochemical cell-twinning 面上移動，由理論計算出來的結果顯示，當不是放在 trochochemical cell-twinning 面上時具有較強的鍵結能與較低的結構總能量。此一結果會影響解晶時所選擇空間群的正確性。

第二部份為具有相寬的四元化合物 $\text{Pb}_x\text{Sn}_{6-x}\text{Bi}_2\text{Se}_9$ ($x=0 - 4$)，此結構為空間群 *Cmcm* (No. 63) 之斜方晶系，與 $\text{Pb}_6\text{Bi}_2\text{S}_9$ 結構相同。此化合物為 NaCl-(311) 層狀結構所組成，標示為 *L(7, 7)*，表示孳晶面兩邊各由七層八面體的寬度沿著 [010] 的方向組成。

第三部份中， $\text{Sn}_2\text{Pb}_5\text{Bi}_4\text{Se}_{13}$ 與 $\text{Sn}_{8.65}\text{Pb}_{0.35}\text{Bi}_4\text{Se}_{15}$ 為不具有相寬之四元化合物，其空間群均為 *C2/m* (No.12) 斜方晶系。兩者結構上均具有硫鉍鉛礦系列的特性，於同系列的分類法標示分別為 *L(4, 5)* 與 *L(4, 7)* 由導電度與理論計算的結果證實具有狹窄能隙之半導體， $\text{Sn}_2\text{Pb}_5\text{Bi}_4\text{Se}_{13}$ 和 $\text{Sn}_{8.65}\text{Pb}_{0.35}\text{Bi}_4\text{Se}_{15}$ 的 Seebeck 係數分別為 -80 和 178 ($\mu\text{V/K}$)。

最後， $\text{Pb}_{13}\text{Sb}_{2.08}\text{Bi}_{1.92}\text{Se}_{19}$ 為新結構的化合物，屬於 *C2/m* (No. 12) 空間群之單斜晶系，

晶胞常數為 $a = 14.127(3) \text{ \AA}$, $b = 4.2625(8) \text{ \AA}$, $c = 34.477(6) \text{ \AA}$, $\beta = 96.329(4)^\circ$, 最後所得之 R 值為 $R_1/wR_2/\text{GOF} = 0.0351/0.0822/1.045$, $\text{Pb}_{13}\text{Sb}_{2.08}\text{Bi}_{1.92}\text{Se}_{19}$ 有 NaCl-(311)層狀結構, 於同系列的分類法標示為 L(7, 8)。並經由理論計算與導電度、Seebeck 係數的量測, 證實為具有半導體性質的材料。



Synthesis and Characterization of New Lillianite-type Quaternary Homologous Series of Selenides

Student: Kuei-Bo Chen

Advisor: Dr. Chi-Shen Lee

Department of Applied Chemistry
National Chiao Tung University

Abstract

In this dissertation, all selenide compounds were synthesized by solid state method. These structures were determined and investigated with X-ray diffraction of single crystals. Calculations of the density of states, measurements of Seebeck coefficient and electrical conductivity confirm that these compounds are p- or n-type semiconductors with a narrow band gaps.

Firstly, New ternary and quaternary chalcogenides $\text{Sn}_{3-x}\text{Pb}_x\text{Bi}_2\text{Se}_6$ ($x = 0 - 0.7$) were synthesized and crystallize in the orthorhombic space group *Pnma* (No. 62). The structure for these compounds is related to $\text{Pb}_3\text{Bi}_2\text{S}_6$ with an atomic position near the cell-twinning plane with lillianite homologous series $L(4, 4)$. The ternary phase contains partially occupied Sn site and a quaternary system exhibits a phase width in the range of $0 \leq x \leq 0.7$. Single-crystal structure analysis indicates that there is a correlation between the Pb composition and position shift of M5 site from the cell-twinning plane. Band structure calculations confirmed that the structure is more stable when the position of M5 site is shifted away the cell-twinning plane.

Secondly, quaternary chalcogenides $\text{Pb}_x\text{Sn}_{6-x}\text{Bi}_2\text{Se}_9$ ($x=0 - 4$) crystallizes in

orthorhombic space group *Cmcm* (No. 62) and isostructural to the mineral heyrovskyite, $\text{Pb}_6\text{Bi}_2\text{S}_9$. The $\text{Pb}_x\text{Sn}_{6-x}\text{Bi}_2\text{Se}_9$ features a three-dimensional framework containing slabs of NaCl-(311) type with lillianite homologous series L(7, 7). $\text{Pb}_x\text{Sn}_{6-x}\text{Bi}_2\text{Se}_9$ exhibits identical layers of 7 octahedra wide slabs and each slab is composed of fused rectangular $[\text{M}_{12}\text{Se}_{12}]$ rod units that are expanded along direction [010].

In the third section, quaternary selenides $\text{Sn}_2\text{Pb}_5\text{Bi}_4\text{Se}_{13}$ and $\text{Sn}_{8.65}\text{Pb}_{0.35}\text{Bi}_4\text{Se}_{15}$ were synthesized and crystallize in monoclinic space group *C2/m* (No.12). These compounds exhibit topochemical cell-twinning of NaCl-type structures with lillianite homologous series L(4, 5) and L(4, 7) for $\text{Sn}_2\text{Pb}_5\text{Bi}_4\text{Se}_{13}$ and $\text{Sn}_{8.65}\text{Pb}_{0.35}\text{Bi}_4\text{Se}_{15}$, respectively. Measurements of electrical conductivity indicate that these materials are semiconductors with narrow band gaps; $\text{Sn}_2\text{Pb}_5\text{Bi}_4\text{Se}_{13}$ is *n*-type, whereas $\text{Sn}_{8.65}\text{Pb}_{0.35}\text{Bi}_4\text{Se}_{15}$ is a *p*-type semiconductor with Seebeck coefficients -80(5) and 178(7) $\mu\text{V/K}$ at 300K, respectively.

Finally, quaternary chalcogenides $\text{Pb}_{13}\text{Sb}_{2.08}\text{Bi}_{1.92}\text{Se}_{19}$ was synthesized and crystallize in monoclinic space group *C2/m* (No.12), with lattice parameters of $\text{Pb}_{13}\text{Sb}_{2.08}\text{Bi}_{1.92}\text{Se}_{19}$: $a = 14.127(3) \text{ \AA}$, $b = 4.2625(8) \text{ \AA}$, $c = 34.477(6) \text{ \AA}$, $\beta = 96.329(4)^\circ$, $R_1/wR_2 = 0.0351/0.0822$ and $GOF = 1.045$. These structures reveal novel structure type. $\text{Pb}_{13}\text{Sb}_{2.08}\text{Bi}_{1.92}\text{Se}_{19}$ features a three-dimensional framework containing alternate layers of 7 and 8 octahedra wide slabs of NaCl-(311) type with lillianite homologous series L(7, 8). The semiconductor properties are confirmed with electronic calculations, Seebeck coefficient and electrical conductivity measurements.

Acknowledgments

漫長的碩博八年時間一轉眼就結束，這段時間內經歷了很多，也學習了很多。能夠完成這本博士論文，首先要感謝的就是我的指導老師 李積琛教授的諄諄教誨，讓我對科學研究與人生的價值有了更進一步的瞭解。此外也要感謝百忙中撥空參加口試的裘性天 教授、陳登銘 教授、許火順 教授，以及中正大學的廖儒修 教授，對於論文內容提供了許多寶貴的意見。

在實驗室裡，最感謝明芳同學，在我需要的任何時間、事情，不論是生活上、課業上，都毫不猶豫的給予援手，如果沒有你的幫忙，能不能畢業應該還是個大問題。已經畢了業的翊媚、靜宜、芳卿、冠程、大毛、偉印、香蕉、翔翔，一起度過研究生生活的時光不曾忘記。實驗室的博班成員呆呆、阿明、郝哥、文亨，感謝你們在實驗上的幫助，實驗室的未來就靠你們了。另外，佳芬、家瑜、俊明、俊超、蝌蚪、書維等學弟妹，活潑的個性使實驗室充滿了歡樂的氣氛。好友亞玄、韋達、盈真，因為我的固執堅持害你們吃不少苦，謝謝你們對我這麼大的信任。

當然不忘感謝我的家人無條件的為我付出，不管在經濟上還是精神上，對我來說都是相當重要的，尤其是母親對我的支持已不是用筆墨所能表達我對她的感謝。

最後，這本論文要獻給天國的子怡，我有努力在執行當年的承諾。我深信，帶著我對大家的感謝及大家對我的支持，可以讓我更堅強的面對未來的種種挑戰。

List of Tables

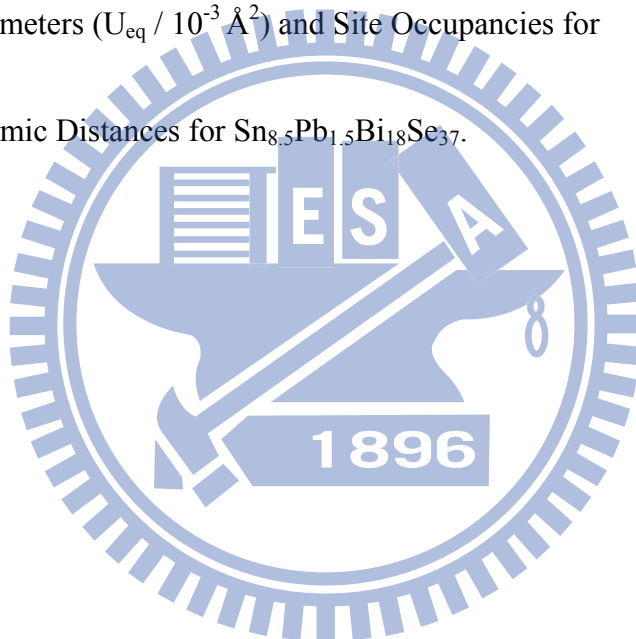
	Page
Chapter 1	
Table 1.1 The sulfosalts with known structures of lillianite family	11
Chapter 2	
Table 2.1 Crystallographic Data for $\text{Sn}_{2.67}\text{Bi}_{2.26}\text{Se}_6$ and $\text{Sn}_{3-\delta}\text{Pb}_\delta\text{Bi}_2\text{Se}_6$. ($\delta = 0, 0.1, 0.3, 0.5, 0.7$)	21
Table 2.2 Selected Interatomic Distances in Å for $\text{Sn}_{3-\delta}\text{Pb}_\delta\text{Bi}_2\text{Se}_6$	22
Table 2.3a Fractional Atomic Coordinates and Equivalent Isotropic Atomic Displacement Parameters (U_{eq} in 10^{-3} \AA^2) and Site Occupancies for $\text{Sn}_3\text{Bi}_2\text{Se}_6$	22
Table 2.3b Fractional Atomic Coordinates and Equivalent Isotropic Atomic Displacement Parameters (U_{eq} in 10^{-3} \AA^2) and Site Occupancies for $\text{Sn}_{3-\delta}\text{Pb}_\delta\text{Bi}_2\text{Se}_6$. ($\delta = 0.1$)	23
Table 2.3c Fractional Atomic Coordinates and Equivalent Isotropic Atomic Displacement Parameters (U_{eq} in 10^{-3} \AA^2) and Site Occupancies for $\text{Sn}_{3-\delta}\text{Pb}_\delta\text{Bi}_2\text{Se}_6$. ($\delta = 0.3$)	23
Table 2.3d Fractional Atomic Coordinates and Equivalent Isotropic Atomic Displacement Parameters (U_{eq} in 10^{-3} \AA^2) and Site Occupancies for $\text{Sn}_{3-\delta}\text{Pb}_\delta\text{Bi}_2\text{Se}_6$. ($\delta = 0.5$)	24
Table 2.3e Fractional Atomic Coordinates and Equivalent Isotropic Atomic Displacement Parameters (U_{eq} in 10^{-3} \AA^2) and Site Occupancies for $\text{Sn}_{3-\delta}\text{Pb}_\delta\text{Bi}_2\text{Se}_6$. ($\delta = 0.7$)	24
Table 2.4 Three models with varied assignments of metal sites for LMTO calculations	26
Table 2.5 Bond valence for $\text{Sn}_{3-\delta}\text{Pb}_\delta\text{Bi}_2\text{Se}_6$ ($\delta = 0 - 0.7$)	30
Chapter 3	
Table 3.1 Crystallographic Data for $\text{Pb}_x\text{Sn}_{6-x}\text{Bi}_2\text{Se}_9$ ($x=0, 1.78, 4.36$)	40
Table 3.2a Fractional Atomic Coordinates and Equivalent Isotropic Atomic Displacement Parameters ($U_{\text{eq}} / 10^{-3} \text{ \AA}^2$) and Site Occupancies for $\text{Sn}_6\text{Bi}_2\text{Se}_9$	41

Table 3.2b Fractional Atomic Coordinates and Equivalent Isotropic Atomic Displacement Parameters ($U_{eq} / 10^{-3} \text{ \AA}^2$) and Site Occupancies for $\text{Pb}_{1.78}\text{Sn}_{4.22}\text{Bi}_2\text{Se}_9$	41
Table 3.2c Fractional Atomic Coordinates and Equivalent Isotropic Atomic Displacement Parameters ($U_{eq} / 10^{-3} \text{ \AA}^2$) and Site Occupancies for $\text{Pb}_{1.78}\text{Sn}_{4.22}\text{Bi}_2\text{Se}_9$	41
Table 3.3 Interatomic Distances for $\text{Pb}_x\text{Sn}_{6-x}\text{Bi}_2\text{Se}_9$ ($x=0, 1.78, 4.36$)	42
Table 3.4a Anisotropic Displacement Parameter ($U / 10^{-3} \text{ \AA}^2$) for $\text{Pb}_{4.36}\text{Sn}_{1.64}\text{Bi}_2\text{Se}_9$.	41
Table 3.4b Anisotropic Displacement Parameter ($U / 10^{-3} \text{ \AA}^2$) for $\text{Pb}_{1.78}\text{Sn}_{4.22}\text{Bi}_2\text{Se}_9$	42
Table 3.5 Three models with varied assignment of metal sites for the LMTO calculations	50
Table 3.6 ICOHP values by integrating the area of the COHP curves	52
Chapter 4	
Table 4.1 Crystallographic Data for $\text{Sn}_2\text{Pb}_5\text{Bi}_4\text{Se}_{13}$ and $\text{Sn}_{8.65}\text{Pb}_{0.35}\text{Bi}_4\text{Se}_{15}$	62
Table 4.2 Fractional Atomic Coordinates and Equivalent Isotropic Atomic Displacement Parameters ($U_{eq} / 10^{-3} \text{ \AA}^2$) and Site Occupancies for $\text{Sn}_2\text{Pb}_5\text{Bi}_4\text{Se}_{13}$	63
Table 4.3 Fractional Atomic Coordinates and Equivalent Isotropic Atomic Displacement Parameter ($U_{eq} / 10^{-3} \text{ \AA}^2$), and Site Occupancies for $\text{Sn}_{8.65}\text{Pb}_{0.35}\text{Bi}_4\text{Se}_{15}$	63
Table 4.4 Interatomic Distances for $\text{Sn}_2\text{Pb}_5\text{Bi}_4\text{Se}_{13}$	64
Table 4.5 Selected Distances in Å for $\text{Sn}_{8.65}\text{Pb}_{0.35}\text{Bi}_4\text{Se}_{15}$	64
Table 4.6 Four models with varied assignment of metal sites for the LMTO calculations	70
Chapter 5	
Table 5.1 Crystallographic Data for $\text{Pb}_{13}\text{Sb}_{2.08}\text{Bi}_{1.92}\text{Se}_{19}$	78
Table 5.2 Fractional Atomic Coordinates and Equivalent Isotropic Atomic Displacement Parameters ($U_{eq} / 10^{-3} \text{ \AA}^2$) and Site Occupancies for $\text{Pb}_{12.92}\text{Sb}_{2.08}\text{Bi}_2\text{Se}_{19}$	82

Table 5.3 Interatomic Distances for $\text{Pb}_{13}\text{Sb}_{2.08}\text{Bi}_{1.92}\text{Se}_{19}$	82
Table 5.4 Anisotropic Displacement Parameter ($U/10^{-3} \text{ \AA}^2$) for $\text{Pb}_{13}\text{Sb}_{2.08}\text{Bi}_{1.92}\text{Se}_{19}$	83

Chapter 6

Table 6.1. Crystallographic Data for $\text{Pb}_4\text{Bi}_{10}\text{Se}_{19}$ and $\text{Sn}_{8.5}\text{Pb}_{1.5}\text{Bi}_{18}\text{Se}_{37}$	95
Table 6.2. Fractional Atomic Coordinates and Equivalent Isotropic Atomic Displacement Parameters ($U_{\text{eq}} / 10^{-3} \text{ \AA}^2$) and Site Occupancies for $\text{Sn}_4\text{Bi}_{10}\text{Se}_{19}$	96
Table 6.3 Interatomic Distances for $\text{Sn}_4\text{Bi}_{10}\text{Se}_{19}$.	96
Table 6.4. Fractional Atomic Coordinates and Equivalent Isotropic Atomic Displacement Parameters ($U_{\text{eq}} / 10^{-3} \text{ \AA}^2$) and Site Occupancies for $\text{Sn}_{8.5}\text{Pb}_{1.5}\text{Bi}_{18}\text{Se}_{37}$	97
Table 6.5. Interatomic Distances for $\text{Sn}_{8.5}\text{Pb}_{1.5}\text{Bi}_{18}\text{Se}_{37}$.	97



List of Figures

	Page
Chapter 1	
Figure 1.1 Schematic of thermoelectric module operation (left) cooling mode; (right) heating mode	3
Figure 1.2 Thermoelectric circuit made of conductors A and B with junction temperatures T_1 and T_2 . Z is the coordinate along the conductors joining the two exits a and b of the voltmeter.	4
Figure 1.3 The Seebeck coefficients, electrical conductivity and thermal conductivity trend of metals, semiconductors, and insulators.	5
Figure 1.4 Relationship between power generating performance index of thermoelectric power generating module and theoretical generating efficiency	6
Figure 1.5 Temperature dependencies on non-dimensional power generating performance index of main thermoelectric conversion materials	7
Figure 1.6 Lillianite $Pb_3Bi_2S_6$ structure projected on (001) direction	10
Chapter 2	
Figure 2.1 (a) Experimental and simulated powder X-ray patterns for $Sn_{3-\delta}Pb_\delta Bi_2Se_6$ ($\delta = 0-0.7$). (b) The refined unit cell volume as a function of Pb composition.	17
Figure 2.2 Lattice parameters for $Sn_{3-\delta}Pb_\delta Bi_2Se_6$ ($0 \leq \delta \leq 0.7$) as a function of the Pb composition	18
Figure 2.3 The crystal structure of $Sn_{3-\delta}Pb_\delta Bi_2Se_6$ as a projection along the crystallographic b -axis [010]. The slabs exhibit NaCl (311) tilt planes and the atoms along the cell-twinning plane exhibit glide arrayal. Δx indicates the shift in position of the M5 atom from the cell-twinning plane.	28
Figure 2.4 The electronic distributions at the five cation sites (a) and variations with the fractional coordinate x of the M5 site (b) in the $Sn_{3-\delta}Pb_\delta Bi_2Se_6$ ($\delta = 0-0.7$) systems. The standard deviations are smaller than the symbols shown.	29
Figure 2.5 Theoretical calculations for the $Sn_3Bi_2Se_6$ model vs. the fractional	31

coordinate x of the M5 sites. The black line is the difference in total energy; the energy at $x = 0.25$ was set to zero for this curve. The blue line shows the ICOHP for the M5 atom vs. fractional coordinate x . The gray area corresponds to single-crystal results for the $\text{Sn}_{3-\delta}\text{Pb}_\delta\text{Bi}_2\text{Se}_6$ ($\delta = 0-0.7$) system.

Figure 2.6 Densities of states and partial densities of states for selected M-Se bonds (Sn: red line, Pb: blue line, total DOS: black line) for the $\text{Sn}_3\text{Bi}_2\text{Se}_6$ (left), $\text{Sn}_2\text{PbBi}_2\text{Se}_6$ (middle), and $\text{Pb}_3\text{Bi}_2\text{Se}_6$ (right) models. The horizontal dashed line denotes the Fermi energy (E_F). 32

Figure 2.7 Crystal-orbital Hamiltonian populations (COHP) for selected M-Se interaction curves (M1-Se and M2-Se: black line, M3-Se and M4-Se: red line, and M5-Se: blue line) for $\text{Sn}_3\text{Bi}_2\text{Se}_6$ (left), $\text{Sn}_2\text{Pb}_1\text{Bi}_2\text{Se}_6$ (middle), and $\text{Pb}_3\text{Bi}_2\text{Se}_6$ (right). 33

Figure 2.8 Temperature dependence of electrical conductivity (a) and thermoelectric power (b) of $\text{Sn}_{3-\delta}\text{Pb}_\delta\text{Bi}_2\text{Se}_6$ for $\delta = 0$ (light blue), $\delta = 0.1$ (black), $\delta = 0.3$ (red), $\delta = 0.5$ (green) and $\delta = 0.7$ (dark blue). 35

Figure 2.9 Thermal analysis (TG/DTA scans) of $\text{Sn}_{3-\delta}\text{Pb}_\delta\text{Bi}_2\text{Se}_6$ ($\delta = 0, 0.1, 0.3, 0.5, 0.7$) 36

Chapter 3

Figure 3.1 (a) Experimental and simulated X-ray powder patterns for $\text{Pb}_{6-x}\text{Sn}_x\text{Bi}_2\text{Se}_9$ ($x=0-6$). (b) The unit cell volume and lattice parameters as a function of Lead composition in $\text{Pb}_x\text{Sn}_{6-x}\text{Bi}_2\text{Se}_9$ ($x=0-5$). 47

Figure 3.2 The electronic distributions at the five cation sites in the $\text{Pb}_x\text{Sn}_{6-x}\text{Bi}_2\text{Se}_9$ ($x = 0-4.36$) systems. The standard deviations are smaller than the symbols shown. 47

Figure 3.3 Crystal structures of $\text{Pb}_x\text{Sn}_{6-x}\text{Bi}_2\text{Se}_9$ (a) projection along [100] direction with slightly perspective and (b) representation using octahedra chains with the same slab thickness. 49

Figure 3.4 DOS/PDS for series of models: $\text{Pb}_{6-x}\text{Sn}_x\text{Bi}_2\text{Se}_9$ ($x = 0, 3, 6$). The black, red, and blue lines refer to total, Sn and Pb atoms, respectively. The horizontal dashed line denotes the Fermi energy (E_F). 51

Figure 3.5 Temperature dependence of electrical conductivity (a) and 53

thermoelectric power (b) of $\text{Pb}_x\text{Sn}_{6-x}\text{Bi}_2\text{Se}_9$ ($x=0, 2$ and 4).

Figure 3.6 Thermal analysis (TG/DTA scans) of $\text{Pb}_{6-x}\text{Sn}_x\text{Bi}_2\text{Se}_9$ ($x=0, 2$ and 4) 54

Chapter 4

Figure 4.1 Experimental and simulated X-ray powder patterns for a) $\text{Sn}_2\text{Pb}_5\text{Bi}_4\text{Se}_{13}$ and b) $\text{Sn}_{8.65}\text{Pb}_{0.35}\text{Bi}_4\text{Se}_{15}$. 59

Figure 4.2 Crystal structures of $\text{Sn}_2\text{Pb}_5\text{Bi}_4\text{Se}_{13}$ (a) and $\text{Sn}_{8.65}\text{Pb}_{0.35}\text{Bi}_4\text{Se}_{15}$ (b) 66
in a projection along the crystallographic b -axis [010], showing slabs **I**, **II**
and **III** of NaCl (113) tilt planes.

Figure 4.3 Density of states (left), partial density of states, and 69
crystal-orbital hamiltonian populations (COHP) for selected M-Se (M1-Se :
black line, M2-Se : red dashed line, and M6-Se : blue line) interactions
(right) curves of $\text{Sn}_2\text{Pb}_5\text{Bi}_4\text{Se}_{13}$. The horizontal dashed line denotes the Fermi
energy (E_F). The contributions from slab **I** (M3 (Bi) + M4 (Pb)) and slab **II**
(M1(Bi) + M2(Bi) + M5(Pb)) are denoted with red and blue lines.

Figure 4.4 DOS/PDOS for series of models: $\text{Sn}_x\text{Pb}_{9-x}\text{Bi}_4\text{Se}_{15}$ ($x = 0, 2, 4, 9$). 71
The black, red, and green lines refer to total, Sn and Pb atoms, respectively.

Figure 4.5 Density of states (left), partial density of states, and 72
crystal-orbital hamiltonian populations (COHP) for selected M-Se (M1-Se :
black line, M3-Se : blue line, M5-Se : red line and M7-Se : green line)
interactions (right) curves of $\text{Sn}_7\text{Pb}_2\text{Bi}_4\text{Se}_{15}$. The horizontal dashed line
denotes the Fermi energy (E_F).

Figure 4.6 PDOS and COHP plots for $\text{Sn}_9\text{Bi}_4\text{Se}_{15}$ (red) and $\text{Sn}_7\text{Pb}_2\text{Bi}_4\text{Se}_{15}$ 72
(blue). a) PDOS for M7 (M = Sn, Pb). b) COHP for M7-Se contact. The
horizontal dashed line denotes the Fermi energy (E_F).

Figure 4.7 Temperature dependence of electrical conductivity (a) and 74
thermoelectric power (b) of $\text{Sn}_2\text{Pb}_5\text{Bi}_4\text{Se}_{13}$ (black) and $\text{Sn}_{8.65}\text{Pb}_{0.35}\text{Bi}_4\text{Se}_{15}$
(red).

Figure 4.8 Thermal analysis (TG/DSC scans) of $\text{Sn}_2\text{Pb}_5\text{Bi}_4\text{Se}_{13}$ (a) and 75
 $\text{Sn}_{8.65}\text{Pb}_{0.35}\text{Bi}_4\text{Se}_{15}$ (b)

Chapter 5

Figure 5.1 Experimental and simulated X-ray powder patterns for $\text{Pb}_{13}\text{Sb}_{2.08}\text{Bi}_{1.92}\text{Se}_{19}$ 79

Figure 5.2 Crystal structures of $\text{Pb}_{13}\text{Sb}_{2.08}\text{Bi}_{1.92}\text{Se}_{19}$ (a) projection along [010] direction with slightly perspective and (b) representation using octahedra chains with different slab thickness. 86

Figure 5.3 Density of states (left), partial density of states, and crystal-orbital hamiltonian populations (COHP) for selected M-Se (M2-Se : blue line, M3-Se : black dashed line, and M6-Se : red line) interactions (right) curves of $\text{Pb}_{13}\text{Sb}_{2.08}\text{Bi}_{1.92}\text{Se}_{19}$. The horizontal dashed line denotes the Fermi energy (E_F). The contributions from slab **I** (M1 (Pb) + M2 (Pb) + M3 (Bi) + M4 (Pb)) and slab **II** (M5 (Pb) + M6 (Sb) + M7 (Pb) + M8 (Pb)) are denoted with blue and red lines. 88

Figure 5.4 Electrical conductivity and thermal power of $\text{Pb}_{13}\text{Sb}_{2.08}\text{Bi}_{1.92}\text{Se}_{19}$ 89

Figure 5.5 Thermal analysis (TG/DTA scans) of $\text{Pb}_{13}\text{Sb}_{2.08}\text{Bi}_{1.92}\text{Se}_{19}$ 90

Chapter 6

Figure 6.1 show the structure of $\text{Sn}_4\text{Bi}_{10}\text{Se}_{19}$ and $\text{Sn}_{8.5}\text{Pb}_{1.5}\text{Bi}_{18}\text{Se}_{37}$ in a projection along the crystallographic b -axis [010]. 98

Chapter 1

Introduction

1.1. Thermoelectric materials

Energy plays a crucial role in modern society. We all depend on a constant and reliable supply of energy—for our homes, businesses, and for transport. It is therefore not surprising that global warming and fast-rising energy costs have seriously affected our daily life. In particular, the increase in carbon dioxide emissions from the burning of fossil fuels is believed to be the origin of irreversible climate change. Approximately 90% of the world's electric power is generated by engines that use fossil fuels and typically operated at ~35% efficiency, with roughly ~65% of heat lost to the environment. Therefore, the reduction in carbon dioxide emissions, either by more efficient use of fossil fuels or greater use of renewable energy, is very important. In this regard, thermoelectric devices are expected to play a vital role in meeting our future energy needs, by enabling a significant reduction in greenhouse gas emissions and our dependence on fossil fuels.

The physics and materials science of thermoelectrics largely developed during two periods of great discovery. In the three decades between 1821 and 1851, the basic thermoelectric effects were explored and understood macroscopically, and more importantly their applicability to thermometry, power generation, and refrigeration was recognized. With the exception of Altenkirch's derivation of thermoelectric efficiency in 1911, progress in the field was negligible in the 80 years that followed. Only after the 1930s, the microscopic understanding of electronic interactions in conductors led to the development of thermoelectric materials currently employed for solid state refrigeration and power generation.¹

The thermoelectric devices have several obvious advantages when compared with conventional refrigeration systems: (1) Thermoelectric devices can function in environments that are too severe, too sensitive, or too small for conventional refrigeration. (2) Thermoelectric devices have no moving parts, and no fluids or other materials that require periodic replenishment; theoretically, they can run indefinitely without the need of any kind of maintenance. (3) Highly precise temperature control within ± 0.1 °C can be ensured using thermoelectric devices and appropriate support circuitry. (4) Thermoelectric devices contain no chlorofluorocarbons or other materials which may pollute the environment. (5) Accelerated life-testing indicated the capability of thermoelectric devices to exceed more than 100 000 hours of steady-state operation. (6) The direction of heat transfer in a thermoelectric system is fully reversible. Changing the polarity of the DC power supply causes heat to be transferred in the opposite direction—a cooler can then become a heater.

According to all the above mentioned advantages, thermoelectric devices have in the last decade found very broad applications in many areas, such as military, aerospace, instrumentation and sensors, industrial and commercial products².

Thermoelectric devices are solid-state devices that can convert electrical energy into a temperature gradient or convert thermal energy from a temperature gradient into electrical energy. Traditionally, the term thermoelectricity includes three separately identified effects—the Seebeck effect, the Peltier effect, and the Thomson effect.³⁻⁵ The practical applications of these thermoelectric phenomena remained limited until the development of semiconductor materials.

Among the most important applications of thermoelectric phenomena is thermoelectric refrigeration, which is achieved when a direct current is passed through one or more pairs of n- and p-type semiconductor materials.⁶ Figure 1.1 is a diagram of a single pair consisting of n- and p-type semiconductor materials. In the cooling mode, direct current passes from the n-

to the p-type semiconductor material. The temperature T_C of the interconnecting conductor decreases and heat is absorbed from the environment. This heat absorption from the environment (cooling effect) occurs when electrons pass from a low energy level in the p-type material through the interconnecting conductor to a higher energy level in the n-type material. The absorbed heat is transferred through the semiconductor materials by electron transport to the other end of the junction of T_H temperature and liberated as the electrons return to a lower energy level in the p-type material. This phenomenon is known as the Peltier effect bears the name of Jean-Charles Peltier, the French physicist who discovered it in 1834.

A second phenomenon is also important in thermoelectric refrigeration. When a temperature difference is established between the hot and cold ends of the semiconductor material, a voltage is generated. This voltage is called the Seebeck voltage, and it is directly proportional to the temperature difference. The constant of proportionality, shown in Fig. 1.2, is referred to as the Seebeck coefficient. It is defined as the open circuit voltage produced between two points on a conductor, when a uniform temperature difference of 1 K exists between those points.

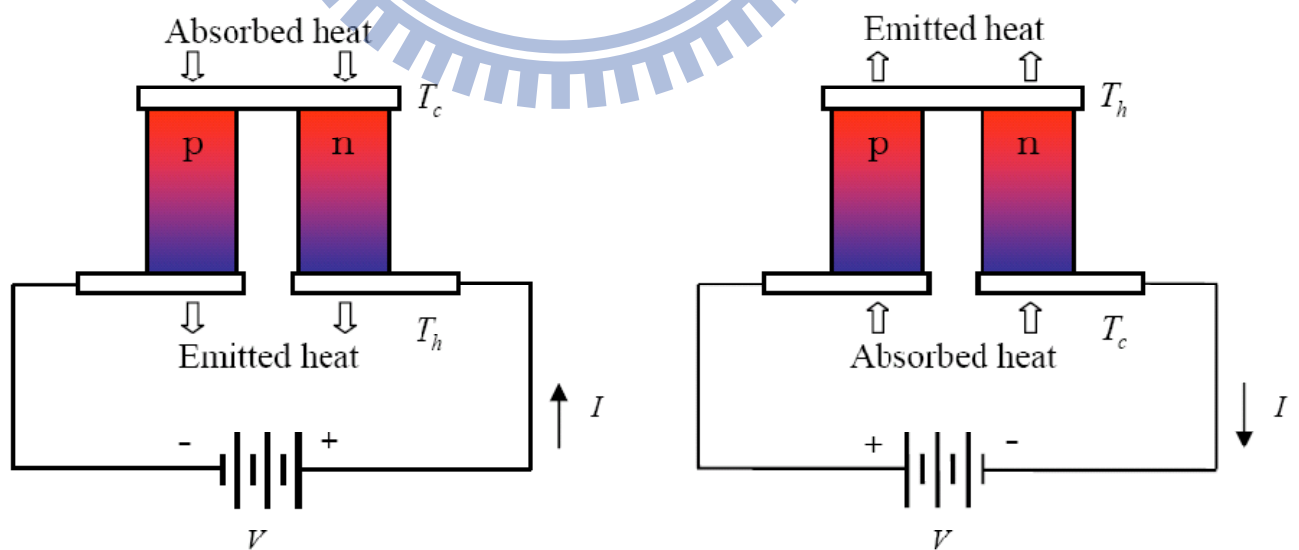


Figure 1.1 Schematic of thermoelectric module operation (left) cooling mode; (right) heating mode

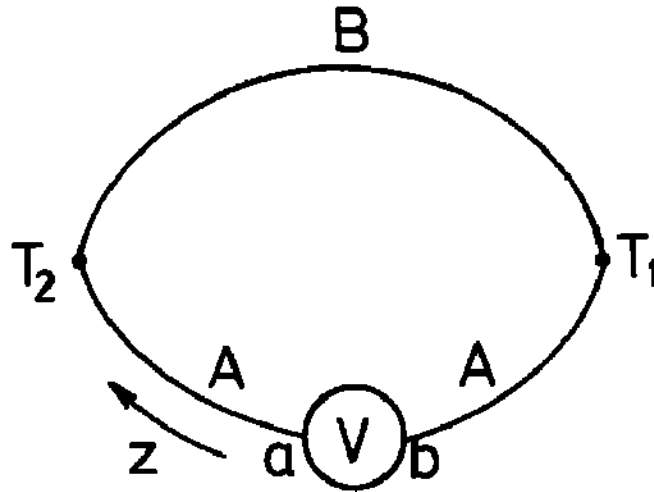


Figure 1.2 Thermoelectric circuit made of conductors A and B with junction temperatures T_1 and T_2 . Z is the coordinate along the conductors joining the two exits a and b of the voltmeter.

Lastly, William Thomson (Lord Kelvin) predicted and subsequently experimentally observed a third thermoelectric phenomenon, the reversible cooling and heating of a homogeneous conductor when an electrical current flows along it in the presence of a temperature gradient. This is widely known as the Thomson effect and is defined by the rate of heat generated or absorbed in a single current carrying conductor subjected to a temperature gradient. The Thomson coefficient is unique among the three main thermoelectric coefficients because it is the only thermoelectric coefficient directly measurable for individual materials. The Peltier and Seebeck coefficients can only be determined for pairs of materials.

Good thermoelectric materials should possess large Seebeck coefficients and high electrical conductivity, but low thermal conductivity.^{7, 8} More specifically, a high electrical conductivity is necessary to minimize Joule heating effects, whilst a low thermal conductivity not only helps to retain heat at the junctions, but also to maintain a large temperature gradient. These three properties were later embodied in the so-called figure-of-merit,

$$ZT = S^2\sigma/\kappa,$$

where S is the Seebeck coefficient, σ the electrical conductivity and κ the thermal conductivity. This non-dimensional power generating performance index is used to assess the power generating efficiency of semiconducting materials. The combination of these three properties allows to select the most suitable semiconducting materials for thermoelectric applications on the basis of their capability to attain a maximum value of the product ZT , where T is the absolute temperature (see Fig. 1.3).⁹ The power obtained depends on efficiency, which is, in turn, determined by the heat flux from the high temperature heat source and the temperature differential during thermoelectric power generation, and the thermoelectric properties of the materials.

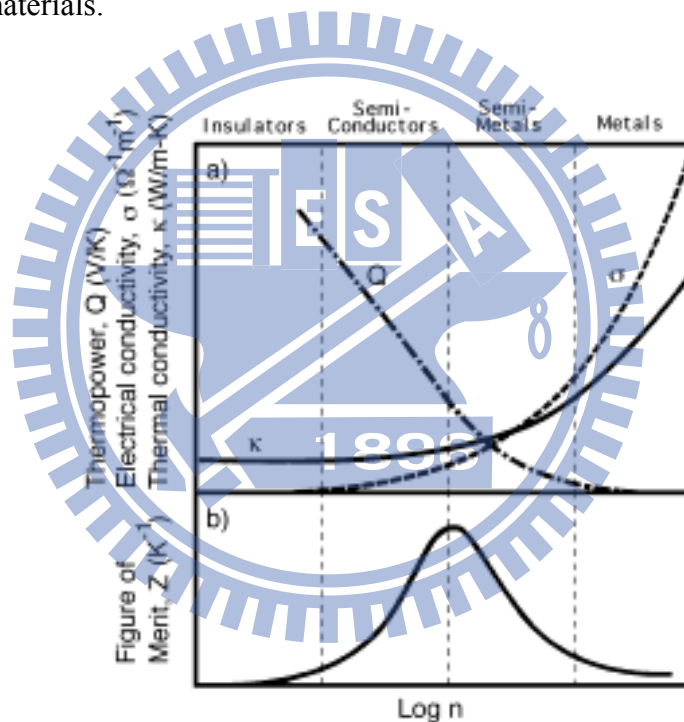


Figure 1.3 The Seebeck coefficients, electrical conductivity and thermal conductivity trend of metals, semiconductors, and insulators⁹.

The maximum efficiency of thermoelectric generating systems is given by the Carnot efficiency; this is an index for an ideal heat engine, and the physical properties of the materials, which is termed material efficiency. The relationship between the performance index of a thermoelectric power generating module and the theoretical generating efficiency

in the case where the Carnot efficiency is 50% is shown in Fig. 1.4.¹⁰ According to this figure, the theoretical generating efficiency approaches the Carnot efficiency as the non-dimensional power generating performance index, ZT , becomes larger. In the current thermoelectric conversion materials in which ZT is approximately equal to 1, theoretical generating efficiency is approximately 9%.

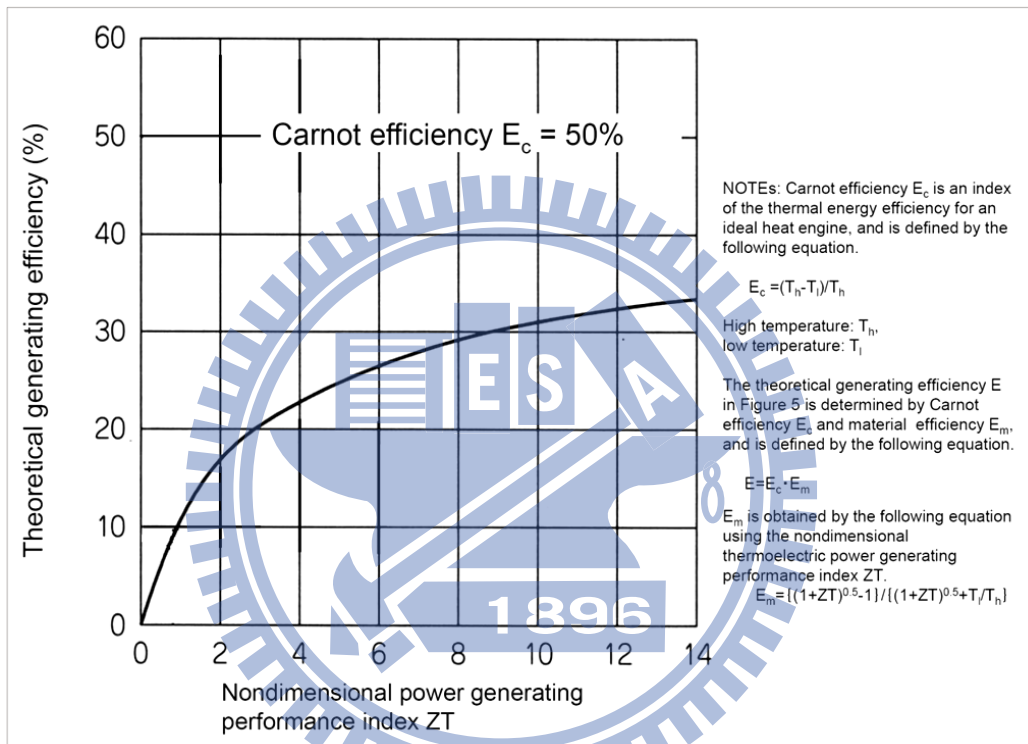


Figure 1.4 Relationship between power generating performance index of thermoelectric power generating module and theoretical generating efficiency¹⁰.

The thermoelectric conversion materials should have a non-dimensional power generating performance index, ZT , of 2 or higher. The dependence of this power generating performance index of thermoelectric energy conversion materials on temperature is illustrated in Fig. 1.5. To date, the most widely used thermoelectric materials have been intermetallic compounds such as bismuth telluride (Bi_2Te_3), zinc antimonide (ZnSb) and SiGe . In particular, Bi_2Te_3 -based compounds have an unusually high ZT value at room temperature, and are therefore the most commonly used thermoelectric material. The ZT value of these materials

tends to initially increase with increasing temperature and to decrease once a certain temperature has been exceeded. The power generating performance index of Bi_2Te_3 and Zn_4Sb_3 ranges between 1.0 and 1.25 in the low medium temperature region of 300-700 K, while a compound of $\text{AgSbTe}_2/\text{GeTe}$ (composition ratio 1:1) shows ZT approximately equal to 1.2 at 700K and $\text{Si}_{0.2}\text{Ge}_{0.8}$ shows $ZT \approx 0.7$ at approximately 1100K. In the temperature region under 500 K, BiTe-based compounds display high ZT values. In the medium temperature region of 700-900 K, $\text{AgSbTe}_2/\text{GeTe}$ and $\text{CeFe}_4\text{CoSb}_{12}$ are high efficiency materials, and in the high temperature region up to 900 K, the high efficiency materials are $\text{Si}_{0.2}\text{Ge}_{0.8}$, $\text{Bi}_2\text{Sr}_2\text{Co}_2\text{O}_y$, and $\text{Ca}_3\text{Co}_4\text{O}_9$. Despite the multitude of materials which are suitable for practical applications of thermoelectricity, during the past 50 years, it has been extremely difficult to increase the power conversion performance to $ZT > 1$, because electric resistance and thermal conductivity are mutually dependent.

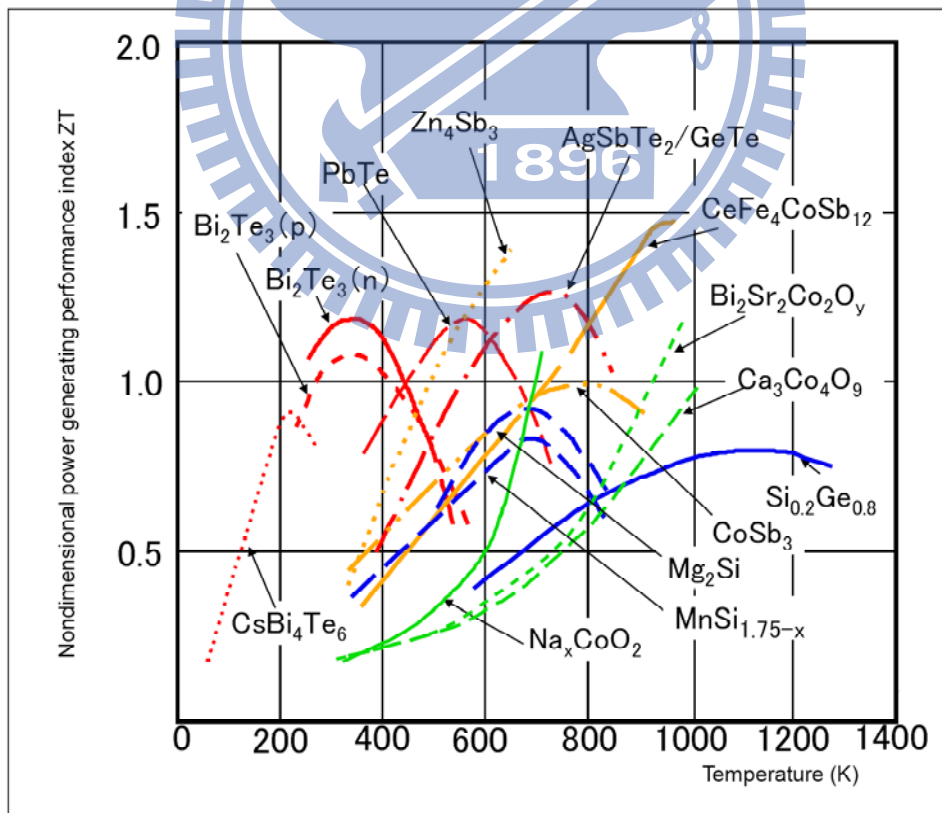


Figure 1.5 Temperature dependencies on non-dimensional power generating performance index of main thermoelectric conversion materials¹¹

During the 1990s, two approaches developed independently and mostly in different directions. Firstly, nanoscale constituents, prepared by different chemical approaches were introduced to the most prominent of bulk thermoelectric materials.¹²⁻¹⁵ Secondly, low-dimensional materials systems were now being assembled as three-dimensional nanocomposites containing a coupled assembly of nanoclusters showing short-range low dimensionality embedded in a host material,^{1,16} thereby producing a bulk material with nanostructures and many interfaces that scatter phonons more effectively than electrons.

Among chalcogenides, $\text{Bi}_{2-x}\text{Sb}_x\text{Te}_{3-y}\text{Se}_y$ is the best known thermoelectric material that has long served the needs of cooling applications at ambient temperature ($ZT \sim 1$).⁹ Recently, two new materials were identified, CsBi_4Te_6 and $\text{AgPb}_m\text{SbTe}_{2+m}$ which show good thermoelectric properties ($ZT = 0.82$ and 2.2) at both low and high temperature.^{17,18} In addition, new techniques have been developed for the deposition of nanometer-sized thermoelectric materials on thin films. Some rational approaches to the development of future solid-state systems include materials with a large ZT value, such as clathrate¹⁹⁻²¹ and skutterudite^{22,23} phases. Lastly, chalcogenides that contain heavy main-group elements and exist in minerals and synthetic compounds have attracted intensive research for their prospective applications in thermoelectric devices.

1.2. Homologous series

A series of structures built on the same structural principle with certain building blocks expanding by regular increments is called a homologous series. This could be built through the addition of a layer or a row of atoms on a given block. A homologous series is expressed by means of a mathematical formula that has ability to reproduce each member. It is a useful tool for designing compounds, because it allows a modular classification of its members, while concentrating on large scale structural features. The classification of the building blocks (or called modules) requires a certain level of abstraction with respect to the atomic occupancy and bonding details. The efficacy of a given homology depends on its ability to generate an infinite number of structure types.

Complex structures can be assembled from one, or more kinds of building blocks. Generally, the building blocks of a homologous series of compounds are simple, common units that adopt archetypal structures or are excised from such structures (e.g., NaCl-type blocks). To form each member, these building blocks need to combine in various ways according to the principles of coordination chemistry or by the action of structure building operators, unit cell intergrowth, glide reflection twinning, cyclic twinning, etc.²⁴ Within a homologous series, the type of fundamental building units and the principles that define how they combine remain preserved. Only the size of the building blocks can vary incrementally by changing the number of coordination polyhedra.

The term homologous series was used to describe chemical series that can be expressed by a general mathematical formula and built on the same structural principles,²⁵ first in complex metal oxide systems^{26, 27} and later in intermetallics, chalcogenides,^{28, 29} etc. Several homologous series are known for sulfides; these include the kobellite series,³⁰ the pavonite series,³¹ the gustavite-lillianite series.³² In addition, it was found that the BaQ/Fe₂Q₃ system (Q = S, Se) defined the 2D homologous series (BaQ)_n(Fe₂Q₃)_m.³³ In recent paper, Kanatzidis

et al. studied a new homologous series of $A_m[M_{1+l}Se_{2+l}]_{2m}[M_{2l+n}Se_{2+3l+n}]$, where A denotes an alkali or alkaline earth element; M is a main-group metal; and the three integer variables, l , m , and n , are used to control the shape or size in this series.^{34, 35}

The lillianite homologous series has also been investigated by Kanatzidis *et al.*³⁶ On the other hand, the first sample of lillianite ($Pb_3Bi_2S_6$), a rare Pb-Bi sulfosalt, were found³⁷ and defined^{38, 39} by Makovicky *et al.* Its members are generated by trochochemical cell twinning on to the (311) plane of slabs of galena (NaCl-type) lattices with a mirror as twin operation and reflecting the lattices across the mirror planes at $z=\pm 1/4$. In different lillianite homologous series in the thickness of the NaCl-type building blocks varies. Trochochemical cell twinning is a twinning on the cell scale which has been reported for minerals. This phenomenon takes place during those structural changes that are accompanied by a change in chemical composition. It can also be considered as a stress-relieving mechanism that accommodates impurities in the crystal. Figure 1.6 depicts the $Pb_3Bi_2S_6$ structure with trochochemical cell twinning. The various members of the lillianite homologous series can be identified by the number of metal octahedral along the (111) direction of the galena slabs.

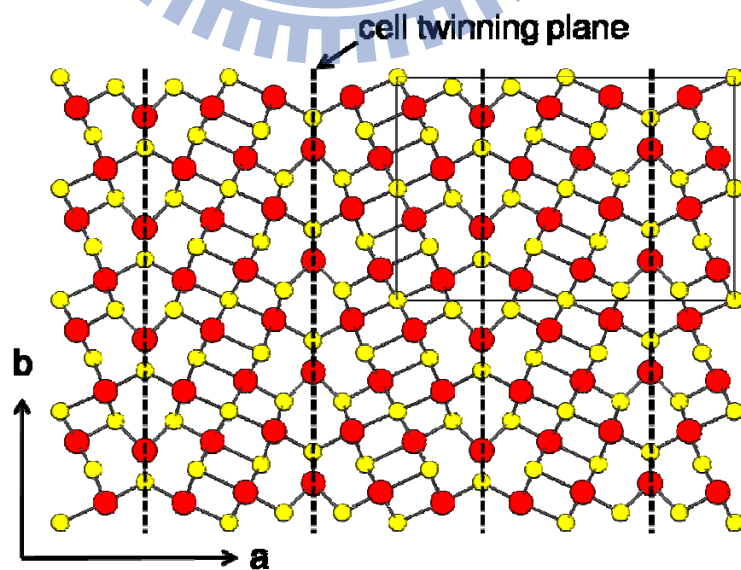


Figure 1.6 Lillianite $Pb_3Bi_2S_6$ structure projected on (001) direction³⁷.

The structures of the lillianite homologous series are described by the symbols L, n, n', where L indicates a member of the lillianite series, and n and n' correspond to the number of octahedra between two sides of the trochochemical cell-twinning plane. The symbol L(n, n') reflects the cation/anion ratio (M/X). The limit of the M/X ratio is located between 1 (PbS for L(∞, ∞)) and 0.714 (PbBi₄S₇ for L(2,1)). In the polysynthetic twinning in NaCl-(311) type, the M/X ratio decreases with increasing number of octahedral, n. For example, the mineral lillianite, Pb₃Bi₂S₆, is denominated as L(4, 4) and K_xSn_{6-2x}Bi_{2+x}Se₉ as L(7, 7), where the symbols mean that two identical, 4 and 7, octahedral blocks undergo cell-twinning. The sulfosalts of the lillianite family with a known structure are summarized in Table 1.1. In lillianite, three Pb²⁺ ions in galena have been placed by two Bi³⁺ ions, and one cation site has been eliminated,



There is a 16.67% (1/6) “cation deficiency” as compared with perfect galena (PbS).

Table 1.1 The sulfosalts with known structures of lillianite family^{40, 41}

Species	Ideal composition		symbol L(N,N')
	X/M	M/X	
Galena, PbS	1.000	1.000	(∞, ∞)
Ourayaite, Ag _{12.5} Pb ₁₅ Bi _{20.5} S ₅₂	1.083	0.923	(11,11)
Heyrovskite, Pb _{5.4} Bi _{2.42} Ag _{0.18} S ₉	1.125	0.889	(7,7)
Eskimoite, Ag ₇ Pb ₁₀ Bi ₁₅ S ₃₆	1.125	0.889	(9,5)
Treasurite, Ag ₇ Pb ₆ Bi ₁₅ S ₃₂	1.143	0.875	(8,4)
Vikingite, Ag ₅ Pb ₈ Bi ₁₃ S ₃₀	1.154	0.867	(7,4)
Lillianite, Pb ₃ Bi ₂ S ₆	1.200	0.833	(4,4)
Benjaminite, Ag ₃ Bi ₇ S ₁₂	1.200	0.833	(4,4)
Gustavite, AgPbBi ₃ S ₆	1.200	0.833	(7,1)
Pavonite, AgBi ₃ S ₅	1.250	0.800	(5,1)
Cu _{3.21} Bi _{4.79} S ₉	1.286	0.778	(4,1)
CuBi ₅ S ₈	1.333	0.750	(3,1)
Pb ₂ Bi ₆ S ₁₁	1.375	0.727	(2,2,1)
Pb ₃ Bi ₁₀ S ₁₈	1.385	0.722	(2,2,1,2,1)
PbBi ₄ S ₇	1.400	0.714	(2,1)

1.3. Motivation and goal of this thesis

Post-transition-metal ions such as Bi^{3+} and Pb^{2+} often generate distorted coordination environments associated with the inert lone electron pair⁴²⁻⁴⁴. The chalcogenide compounds formed by combinations of such ions usually exhibit complex crystal structures and semiconducting properties with a narrow band gap, and are promising materials for nonlinear optics⁴⁵, ferroelectrics⁴⁶, and thermoelectrics⁴⁷⁻⁴⁹. In a synthesis of new materials with useful thermoelectric properties, heavy main-group elements, such as tin, lead, antimony and bismuth, might enhance the electrical conductivity and diminish the thermal conductivity. Materials in this class contain various coordination environments constructed from M^{2+} ($\text{M} = \text{Sn}, \text{Pb}$) and M^{3+} ($\text{M} = \text{In}, \text{Sb}, \text{Bi}$) centers and Se^{2-} ions assembled into a structure similar to lillianite. These structures are homologous, with ordered intergrowths of “galena-like” structures cut parallel to the (311) plane to form a number of diverse frameworks with chemically twinned arrangements, a current theme in crystal chemistry that has recently been reviewed^{38, 50-52}. Many naturally occurring minerals and synthetic lillianite-type chalcogenides have been studied, including PbBi_4S_7 [L (2,1)]⁵³; CuBi_3S_8 [L (3,1)]⁵⁴; $\text{Cu}_{3.21}\text{Bi}_{4.79}\text{S}_9$ [L (4,1)]⁵⁵; AgBi_3S_5 [L (5,1)]⁵⁶; $\text{Pb}_3\text{Bi}_2\text{S}_6$ ^{37, 57}, $\text{AgPbBi}_3\text{S}_6$ ⁵⁸, and $\text{AgPbSb}_3\text{S}_6$ [L (4,4)]⁵⁹; $\text{Ag}_5\text{Pb}_8\text{Bi}_{13}\text{S}_{30}$ [L (4,7)]³⁹; $\text{Pb}_6\text{Bi}_2\text{S}_9$ ⁶⁰ and $\text{K}_{0.54}\text{Sn}_{4.92}\text{Bi}_{2.54}\text{Se}_9$ [L(7,7)]³⁶; $\text{Ag}_3\text{Bi}_7\text{S}_{12}$ [L (7,1)]⁶¹; $\text{KSn}_5\text{Bi}_5\text{Se}_{13}$ [L(4,5)]³⁶; $\text{Ag}_7\text{Pb}_6\text{Bi}_{15}\text{S}_{32}$ [L (4,8)]⁶²; $\text{Ag}_7\text{Pb}_{10}\text{Bi}_{15}\text{S}_{36}$ [L (5,9)]³⁸; and $\text{Ag}_{12.5}\text{Pb}_{15}\text{Bi}_{20.5}\text{S}_{52}$ [L (11,11)]⁵⁰. Most of the above lillianite-type chalcogenides are sulfosalts; only a few selenides have been reported. Recently, we have demonstrated that multinary selenides, such as $\text{InSn}_2\text{Bi}_3\text{Se}_8$ ⁶³, $\text{InSn}_6\text{BiSe}_9$ and $\text{Pb}_4\text{In}_x\text{M}_{6-x}\text{Se}_{13}$ ($\text{M} = \text{Bi}, x = 2.1-2.8$; $\text{Sb}, x = 2$)⁶⁴, can be prepared through solid-state synthetic routes that comprise various building units. Theoretical calculations have shown that the mixed occupancy metal sites arise from optimized M-Se bonding.

In this work, we investigated the quaternary chalcogenides that contain groups 3-5 heavy

main-group elements. On introducing heavy main-group elements such as Pb and Bi, an intriguing feature is the stereochemical localization of their ns^2 electrons that might influence the structural type and electronic structure, and consequently the electronic properties of the resulting compounds. Here we report the synthesis, structural characterization, measurements of physical properties, and calculations of electronic structures of five new quaternary selenides $\text{Sn}_{3-\delta}\text{Pb}_\delta\text{Bi}_2\text{Se}_6$ ($\delta = 0 - 0.7$), $\text{Pb}_x\text{Sn}_{6-x}\text{Bi}_2\text{Se}_9$ ($x = 0 - 4.36$), $\text{Sn}_2\text{Pb}_5\text{Bi}_4\text{Se}_{13}$, $\text{Sn}_{8.65}\text{Pb}_{0.35}\text{Bi}_4\text{Se}_{15}$ and $\text{Pb}_{13}\text{Sb}_{2.08}\text{Bi}_{1.92}\text{Se}_{19}$. First two compounds contained a measurable phase width and the other compounds have no phase width. The compounds of $\text{Sn}_{3-\delta}\text{Pb}_\delta\text{Bi}_2\text{Se}_6$ ($\delta = 0.0 - 0.7$) were synthesized and their structures are related to that of $\text{Pb}_3\text{Bi}_2\text{S}_6$ with an atomic position near the cell-twinning plane. Band structure calculations indicated that the structure is stabilized when the position of the M5 site is farther from the cell-twinning plane. The substitution of lead for tin cations in $\text{Pb}_x\text{Sn}_{6-x}\text{Bi}_2\text{Se}_9$ because of the similar bonding strength in Pb/Sn atoms and varying the Pb/Sn ratio produces significant variation of the physical and electronic properties. Quaternary selenides $\text{Sn}_2\text{Pb}_5\text{Bi}_4\text{Se}_{13}$ and $\text{Sn}_{8.65}\text{Pb}_{0.35}\text{Bi}_4\text{Se}_{15}$ exhibit topochemical cell-twinning of NaCl-type structures with lillianite homologous series $L(4, 5)$ and $L(4, 7)$, respectively. $\text{Pb}_{13}\text{Sb}_{2.08}\text{Bi}_{1.92}\text{Se}_{19}$ reveals novel structure type with alternated 7 and 8 octahedra wide slabs. Calculations of band structures, measurements of Seebeck coefficient and electrical conductivity confirm that these compounds are semiconductors with a narrow band gap.

Chapter 2

Experimental and Theoretical Studies of $\text{Sn}_{3-\delta}\text{Pb}_\delta\text{Bi}_2\text{Se}_6$ ($\delta = 0.0\text{--}0.7$)

Abstract

New ternary and quaternary chalcogenides $\text{Sn}_{3-\delta}\text{Pb}_\delta\text{Bi}_2\text{Se}_6$ ($\delta = 0.0\text{--}0.7$), were synthesized from pure elements using the solid-state method. Their crystal structures, determined using single crystal X-ray diffraction, belong to the orthorhombic space group *Pnma* (No. 62). The structure is related to $\text{Pb}_3\text{Bi}_2\text{S}_6$ that contains NaCl [311] layer units and zigzag arrays of metal atoms along the *c*-axis. A correlation between the Pb composition and the shifted position of a metal site was observed. Band structure calculations confirmed that the structure is stabilized when the position of the M5 site is farther from the mirror plane. Thermopower and conductivity measurements indicated that all of the compounds are *n*-type semiconductors with small band gaps.

2.1 Experiments

2.1.1 Synthesis

All reactions were carried out in a glovebox under a dry nitrogen atmosphere. The elements were used as received: Sn powder, Alfa 99.5%; Bi powder, Alfa 99.95%; Pb powder, Alfa 99%; and Se powder, Alfa 99.9%. In a typical reaction, all compounds were obtained by heating a stoichiometric mixture of the elements in evacuated quartz tubes to 1073 K over 12 hr, holding at 1073 K for 18 hr, slow cooling to 773 K at a rate of 0.42 K min⁻¹, and then cooling to room temperature naturally. Compound (**1**), Sn₃Bi₂Se₆, was initially obtained from a reaction intended to synthesize “Sn₅Bi₆Se₁₄” through the solid-state method. Based on powder X-ray diffraction results, the product of the “Sn₅Bi₆Se₁₄” reaction yielded an unknown phase after a search of the JCPDF database. A cuboid-shaped crystal was selected for single-crystal X-ray diffraction measurements. The refined formula Sn₃Bi₂Se₆ was determined, which was then used to synthesize the pure phase under the same heating conditions specified above. Attempts to obtain the charge-balanced product Sn₃Bi₂Se₆ failed; the reaction product contained a mixture of Sn₃Bi₂Se₆ and SnSe₂ phases. Reactions of Sn_{3-γ}Bi_{2+γ}Se₆ (0 ≤ γ ≤ 1) with Sn_{2.67}Bi_{2.26}Se₆ (refined formula with vacancies) were conducted to probe the possible phase. Two temperature profiles with slow cooling as described above and a quench reaction at 1073 K were performed. For reactions using the slow cooling process, a pure phase was obtained with γ = 0.38 and Sn_{2.67}Bi_{2.26}Se₆ (refined formula). Products of the other reactions contained the primary phase and impurities of SnSe₂ and Sn₃Bi₂Se₆. For reactions using the quenching process, products of reactions with 0 ≤ γ ≤ 0.62 yielded similar powder X-ray patterns to Sn_{2.67}Bi_{2.26}Se₆ with a broad peak width, indicative of poor crystallinity, with which it was impossible to perform a single-crystal study. For the quaternary system, a series of reactions with Sn_{3-δ}Pb_δBi₂Se₆ (0 ≤ δ ≤ 2) were performed to investigate the phase width under the same heating conditions specified above. Based on powder XRD measurements, pure phases were

obtained when $0.1 < \delta < 0.7$ (Figure 2.1a). The calculated lattice parameters a and b exhibited weak correlations with the percent Pb composition, while the lattice parameter c expanded as the concentration of Pb increased in the framework (Figure 2.2). The effect of percent Pb composition on the cell volume is shown in Figure 2.1b, indicating that the cell volume varies from $1204(2) \text{ \AA}^3$ for $\text{Sn}_3\text{Bi}_2\text{Se}_6$ ($x = 0$) to $1230(2)$ for $\text{Sn}_{2.3}\text{Pb}_{0.7}\text{Bi}_2\text{Se}_6$ ($x = 0.7$). The PbSe impurity phase began to form when $\delta > 0.7$. Crystals from the $\delta = 0.1, 0.3, 0.5,$ and 0.7 reactions were selected for single-crystal X-ray analysis.

2.1.2 Single-crystal X-ray Diffraction (XRD)

Cuboid-shaped crystals obtained for $\text{Sn}_{3-\delta}\text{Pb}_\delta\text{Bi}_2\text{Se}_6$ [$\delta = 0.0$ (1), 0.1 (2), 0.3 (3), 0.5 (4), and $x = 0.7$ (5)] were mounted on a glass fiber with epoxy glue for single-crystal X-ray diffraction analysis. Intensity data were collected using a diffractometer (Bruker APEX CCD equipped with graphite-monochromated Mo-K α radiation, $\lambda = 0.71073 \text{ \AA}$) at 300 K. The crystal-to-detector distance was 5.038 cm and the exposure time was 30 s. Data were collected with a scan width of 0.3° in ω with four groups of 600 frames at ψ settings of $0^\circ, 90^\circ, 180^\circ,$ and 270° . The 2θ values ranged between 1.76° and 56.54° . Diffraction peaks obtained from all frames of the reciprocal space images were integrated and used to determine the unit cell parameters using the Siemens SAINT program. The data were corrected for Lorentz and polarization effects using SADABS⁶⁵. Absorption corrections were based on a function fitted to the empirical transmission surface sampled by multiple equivalent measurements of numerous reflections. The structural model was obtained using the direct method and refined by full-matrix least-squares refinement based on F^2 using the SHELXTL package⁶⁶.

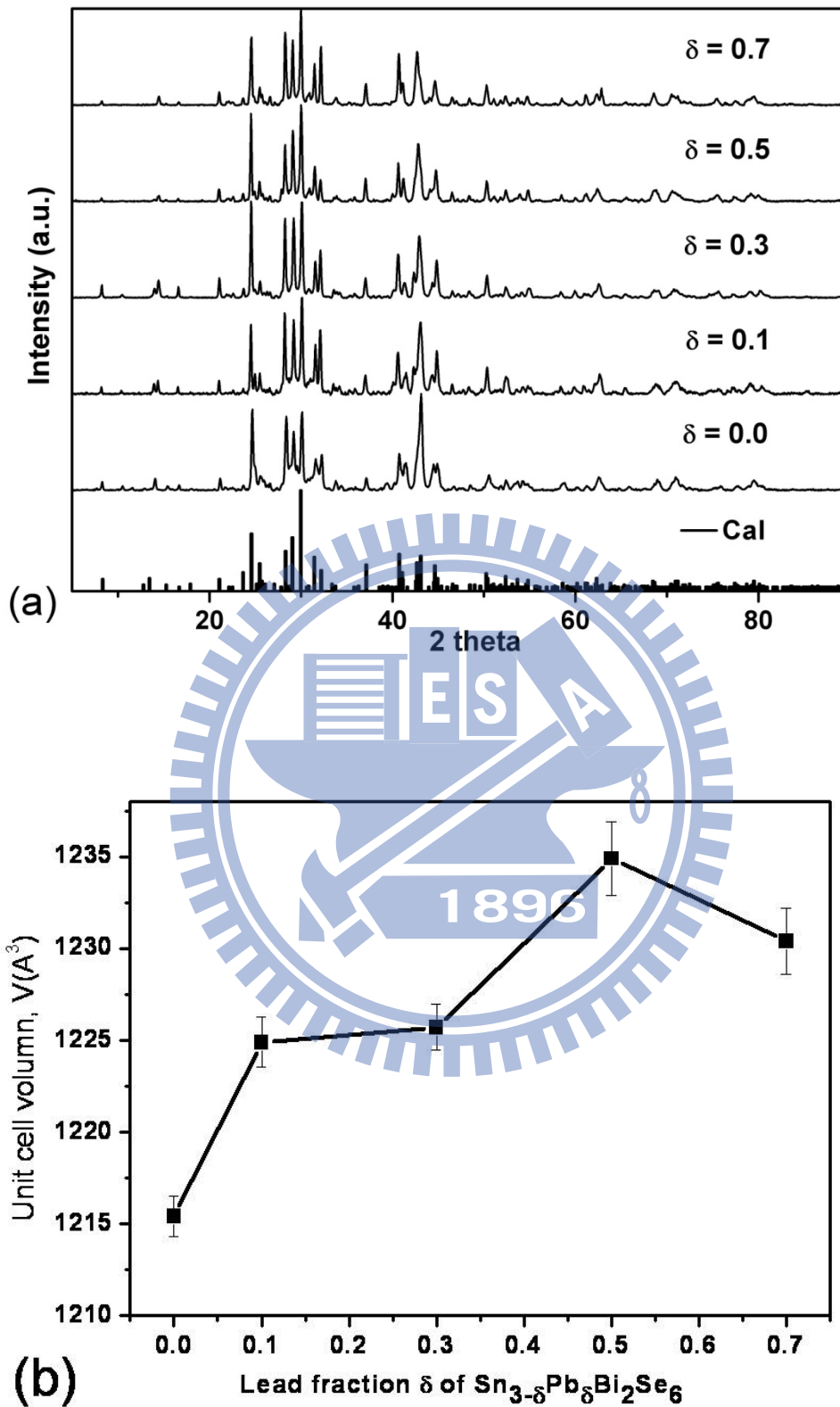


Figure 2.1 (a) Experimental and simulated powder X-ray patterns $\text{Sn}_{3-\delta}\text{Pb}_\delta\text{Bi}_2\text{Se}_6$ ($\delta = 0 - 0.7$).

(b) The refined unit cell volume as a function of Pb composition.

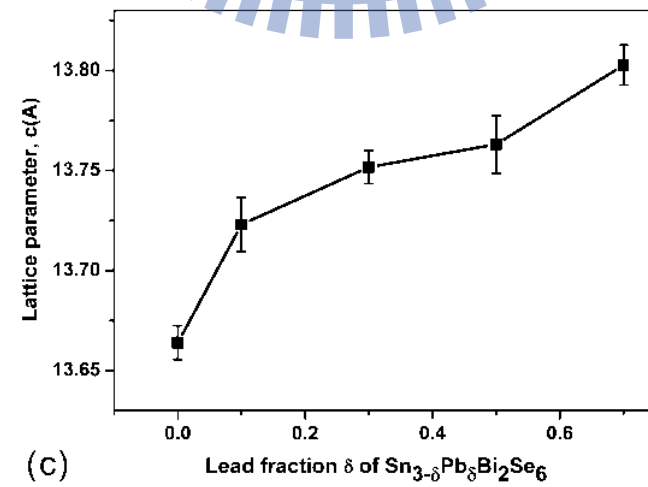
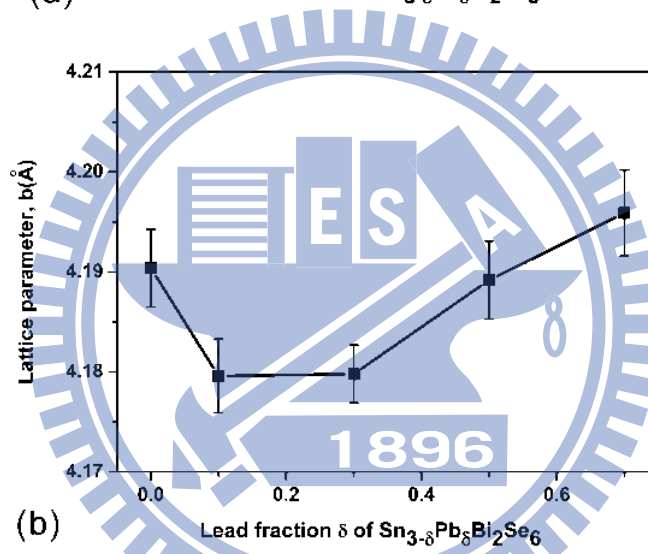
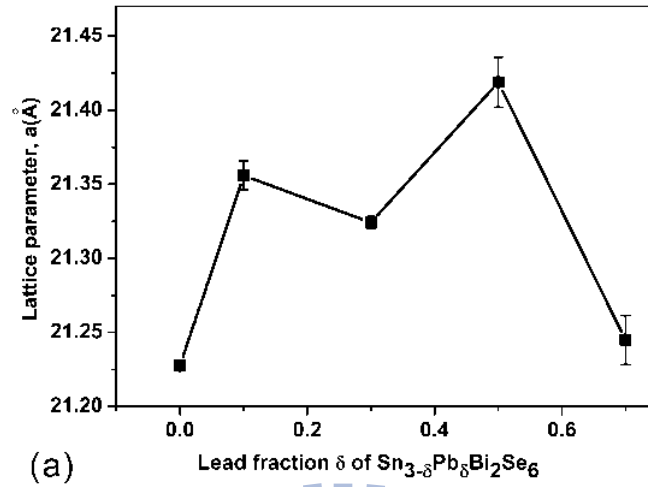


Figure 2.2 Lattice parameters for $\text{Sn}_{3-\delta}\text{Pb}_\delta\text{Bi}_2\text{Se}_6$ ($0 \leq \delta \leq 0.7$) as a function of the Pb composition.

All compounds had an orthorhombic lattice. Analysis of the systematic absence of reflections for compounds **1**, **2**, and **3** suggested space group *Pnma* (No. 62). In the structural refinement process, a structural model was determined having five unique sites containing metal atoms (Sn, Bi, and Pb) and six unique sites containing Se atoms. The occupancy parameters were refined along with the displacement parameters. The results indicated that all Se sites were fully occupied and the M1-M5 sites had mixed occupancies. The calculated electron densities of the M1-M5 sites were within 50–81 electrons/site, which were refined to fully occupied Sn (M3 site in compound **1**) or mixed occupancy Sn/Bi or Sn/Pb sites. The final cycle of refinement included anisotropic displacement parameters and a secondary extinction correction performed on F^2 . For compound **1**, the refinement of metal sites suffers from strong correlation between site occupancy and displacement parameter due to the poor X-ray diffraction data. The refinements indicate different electron densities in M1-M5 sites, and subsequently the site composition were estimated from the refined electron densities and fixed in the final stage of refinement. Fourier maps from **1**, **2** and **3** reveal residual peaks $\sim 3.8\text{--}4.3\text{ e}^-/\text{\AA}^3$ close to M5 ($\sim 0.9\text{ \AA}$). The refined compositions for **1**, **2**, and **3** were $(\text{Sn}^{+2})_3(\text{Bi}^{+3})_2(\text{Se}^{-2})_6$, $(\text{Sn}^{+2})_{2.93}(\text{Pb}^{+2})_{0.19}(\text{Bi}^{+3})_{1.89}(\text{Se}^{-2})_6$, and $(\text{Sn}^{+2})_{2.67}(\text{Pb}^{+2})_{0.32}(\text{Bi}^{+3})_2(\text{Se}^{-2})_6$, respectively, consistent with reaction stoichiometry.

Compounds **4** and **5** were initially refined with the C-centered space group *Cmcm* (No. 63), and structural refinements yielded reasonable values for $RI/wR2$ (**4**: 4.76%/11.85%, **5**: 3.07%/7.08%). However, the anisotropic displacement factors for the position on the mirror plane (M5 site) had unreasonable values (~ 0.181 and $\sim 0.126\text{ \AA}^2$ along the a-axis for **4** and **5**, respectively). These values could reflect partially occupied Sn or Bi sites, but the refined formulae were not charge-balanced and did not justify this refinement. Ultimately, the *Pnma* space group was chosen and the assignments for the metal and Se sites were similar to those

of **1–3**. The final refinements yielded charge-balanced formulae for **4** and **5** of $(\text{Sn}^{+2})_{2.49}(\text{Pb}^{+2})_{0.42}(\text{Bi}^{+3})_{2.09}(\text{Se}^{-2})_6$ and $(\text{Sn}^{+2})_{2.1}(\text{Pb}^{+2})_{0.67}(\text{Bi}^{+3})_{2.23}(\text{Se}^{-2})_6$, respectively.

Crystallographic data and selected bond distances for compounds **1–5** are given in Tables 2.1, 2.2 and 2.3.



Table 2.1 Crystallographic Data for $\text{Sn}_{3-\delta}\text{Pb}_\delta\text{Bi}_2\text{Se}_6$. ($\delta = 0, 0.1, 0.3, 0.5, 0.7$)

Empirical formula	$\text{Sn}_3\text{Bi}_2\text{Se}_6$ (1)	$\text{Sn}_{2.9}\text{Pb}_{0.1}\text{Bi}_2\text{Se}_6$ (2)	$\text{Sn}_{2.7}\text{Pb}_{0.3}\text{Bi}_2\text{Se}_6$ (3)	$\text{Sn}_{2.5}\text{Pb}_{0.5}\text{Bi}_2\text{Se}_6$ (4)	$\text{Sn}_{2.3}\text{Pb}_{0.7}\text{Bi}_2\text{Se}_6$ (5)
Refined formula	$\text{Sn}_3\text{Bi}_2\text{Se}_6$	$\text{Sn}_{2.93(6)}\text{Pb}_{0.19(3)}\text{Bi}_{1.89(5)}\text{Se}_6$	$\text{Sn}_{2.67(6)}\text{Pb}_{0.32(4)}\text{Bi}_{2.00(6)}\text{Se}_6$	$\text{Sn}_{2.49(4)}\text{Pb}_{0.42(2)}\text{Bi}_{2.09(4)}\text{Se}_6$	$\text{Sn}_{2.1(3)}\text{Pb}_{0.67(1)}\text{Bi}_{2.23(3)}\text{Se}_6$
Formula weight	1247.79	1256.64	1274.34	1292.04	1309.74
Temperature, K	300(2)	300(2)	300(2)	300(2)	300(2)
Wavelength, Å	0.71073	0.71073	0.71073	0.71073	0.71073
Crystal system	Orthorhombic	Orthorhombic	Orthorhombic	Orthorhombic	Orthorhombic
Space group	<i>Pnma</i> (No. 62)	<i>Pnma</i> (No. 62)	<i>Pnma</i> (No. 62)	<i>Pnma</i> (No. 62)	<i>Pnma</i> (No. 62)
Unit cell dimensions, <i>a</i>	<i>a</i> = 21.213(6) Å	<i>a</i> = 21.373(4) Å	<i>a</i> = 21.365(6) Å	<i>a</i> = 21.399(8) Å	<i>a</i> = 21.235(8) Å
<i>b</i>	<i>b</i> = 4.162(1) Å	<i>b</i> = 4.1898(8) Å	<i>b</i> = 4.190(1) Å	<i>b</i> = 4.190(2) Å	<i>b</i> = 4.198(2) Å
<i>c</i>	<i>c</i> = 13.640(4) Å	<i>c</i> = 13.690(2) Å	<i>c</i> = 13.741(4) Å	<i>c</i> = 13.797(5) Å	<i>c</i> = 13.846(6) Å
Volume, Å ³	1204.2(6)	1226.0(4)	1230.2(6)	1239.7(8)	1234.3(9)
4		4	4	4	4
Density (calculated), Mg/m ³	6.883	6.808	6.881	6.923	7.048
Absorption coefficient, mm ⁻¹	53.343	53.56	55.71	57.589	60.161
F(000)	2080	2092.8	2118.4	2144	2170
Crystal size, mm ³	0.1 × 0.03 × 0.03	0.08 × 0.03 × 0.03	0.1 × 0.05 × 0.04	0.08 × 0.03 × 0.03	0.08 × 0.04 × 0.03
Reflections collected	10884	8871	8866	8732	14065
Independent reflections	1701 [R(int) = 0.0455]	1721 [R(int) = 0.0388]	1734 [R(int) = 0.0333]	1744 [R(int) = 0.0571]	1746 [R(int) = 0.0492]
Completeness to theta = 28.24	99.90%	99.90%	99.50%	99.90%	99.80%
Data / restraints / parameters	1701 / 0 / 67	1721 / 0 / 73	1734 / 0 / 73	1744 / 0 / 72	1746 / 0 / 72
Goodness-of-fit on F2	1.913	1.078	1.082	1.059	1.114
Final R indices [I > 2σ(I)]	R1 = 0.0556, wR2 = 0.1310	R1 = 0.0319, wR2 = 0.0774	R1 = 0.0349, wR2 = 0.0792	R1 = 0.0467, wR2 = 0.1193	R1 = 0.0493, wR2 = 0.0975
Largest diff. peak and hole	4.765 and -3.348 e/Å ³	3.836 and -2.35 e/Å ³	3.91 and -2.873 e/Å ³	5.846 and -4.778 e/Å ³	2.942 and -3.985 e/Å ³

$$R1 = \frac{\sum ||F_o| - |F_c||}{\sum |F_o|} \quad wR2 = \left\{ \frac{\sum [w(F_o^2 - F_c^2)^2]}{\sum [w(F_o^2)^2]} \right\}^{1/2}$$

Table 2.2 Selected Interatomic Distances in Å for $\text{Sn}_{3-\delta}\text{Pb}_\delta\text{Bi}_2\text{Se}_6$ ($\delta=0-0.7$)

δ	0	0.1	0.3	0.5	0.7
M1—Se6	2.785(2)	2.792(2)	2.794(2)	2.798(2)	2.780(1)
M1—Se8 × 2	2.866(1)	2.877(3)	2.884(1)	2.889(1)	2.888(2)
M1—Se9 × 2	3.033(1)	3.024(1)	3.036(3)	3.043(2)	3.047(1)
M1—Se10	3.081(2)	3.067(1)	3.082(2)	3.086(2)	3.069(1)
M2—Se7 × 2	2.841(1)	2.860(2)	2.865(3)	2.875(3)	2.892(1)
M2—Se7	3.122(2)	3.179(1)	3.189(1)	3.227(3)	3.307(2)
M2—Se8	2.844(2)	2.834(1)	2.831(2)	2.828(1)	2.784(1)
M2—Se10 × 2	3.086(1)	3.098(1)	3.083(1)	3.076(2)	3.044(1)
M3—Se6	2.798(2)	2.825(1)	2.816(1)	2.815(1)	2.778(2)
M3—Se7 × 2	3.039(2)	3.060(2)	3.055(1)	3.054(2)	3.049(2)
M3—Se10	2.975(2)	3.024(2)	3.027(1)	3.043(1)	2.053(1)
M3—Se11 × 2	2.834(2)	2.848(1)	2.854(2)	2.738(2)	2.879(1)
M4—Se9 × 2	2.977(2)	2.984(1)	2.970(2)	2.963(1)	2.919(1)
M4—Se10 × 2	2.947(2)	2.982(2)	2.989(2)	3.001(2)	3.019(2)
M4—Se11	2.709(2)	2.728(1)	2.728(4)	2.738(2)	2.759(2)
M4—Se9	3.490(2)	3.513(2)	3.499(1)	3.487(3)	3.381(2)
M5—Se6 × 2	2.861(2)	2.868(2)	2.876(1)	2.884(2)	2.881(2)
M5—Se9	2.829(2)	2.893(1)	2.970(2)	3.071(2)	3.377(3)
M5—Se11 × 2	3.194(2)	3.239(1)	3.241(1)	3.258(2)	3.303(2)
M5—Se8 × 2	3.459(1)	3.451(2)	3.438(1)	3.429(3)	3.344(1)

Table 2.3a Fractional Atomic Coordinates and Equivalent Isotropic Atomic DisplacementParameters (U_{eq}) in 10^{-3} (Å²) and Site Occupancies for $\text{Sn}_3\text{Bi}_2\text{Se}_6$

	site	x	y	z	sof	$U(\text{eq})$
M1	4c	0.1409(1)	0.25	0.8288(1)	Bi/Sn [0.8/0.2]	7(1)
M2	4c	0.0490(1)	0.75	0.6102(1)	Bi/Sn [0.8/0.2]	7(1)
M3	4c	0.1251(1)	-0.25	0.3300(1)	Sn [100%]	10(1)
M4	4c	-0.0471(1)	0.75	0.8929(1)	Bi/Sn [0.3/0.7]	14(1)
M5	4c	0.2300(1)	0.75	0.0607(1)	Bi/Sn [0.1/0.9]	21(1)
Se6	4c	0.2574(1)	0.25	0.9232(1)		11(1)
Se7	4c	0.0860(1)	-0.25	0.4806(1)		7(1)
Se8	4c	0.1722(1)	-0.25	0.6927(1)		6(1)
Se9	4c	0.1067(1)	-0.25	0.9815(1)		7(1)
Se10	4c	0.0025(1)	0.25	0.7607(1)		6(1)
Se11	4c	0.1600(1)	0.25	0.1999(1)		6(1)

Table 2.3b Fractional Atomic Coordinates and Equivalent Isotropic Atomic DisplacementParameters (U_{eq}) in 10^{-3} (\AA^2) and Site Occupancies for $\text{Sn}_{3-\delta}\text{Pb}_\delta\text{Bi}_2\text{Se}_6$ ($\delta = 0.1$)

	site	x	y	z	Sof	U_{eq}
M1	4c	0.3597(1)	0.25	0.1697(1)	Bi/Sn [0.812(7)/0.188]	18(1)
M2	4c	0.0496(1)	-0.75	-0.1119(1)	Bi/Sn [0.840(7)/0.160]	17(1)
M3	4c	0.1250(1)	0.25	0.1698(1)	Sn/Bi [0.936(6)/0.064]	16(1)
M4	4c	0.4528(1)	-0.75	-0.1045(1)	Sn/Bi [0.831(6)/0.169]	21(1)
M5	4c	0.2669(1)	-0.25	-0.0610(1)	Sn/Pb [0.814(7)/0.186]	34(1)
Se6	4c	0.2432(1)	0.25	0.0774(1)		20(1)
Se7	4c	0.0865(1)	-0.25	0.0182(1)		18(1)
Se8	4c	0.3288(1)	-0.25	0.3054(1)		18(1)
Se9	4c	0.3923(1)	-0.25	0.0187(1)		18(1)
Se10	4c	0.4965(1)	0.25	0.2378(1)		17(1)
Se11	4c	0.1593(1)	-0.25	0.3002(1)		16(1)

Table 2.3c Fractional Atomic Coordinates and Equivalent Isotropic Atomic DisplacementParameters (U_{eq}) in 10^{-3} (\AA^2) and Site Occupancies for $\text{Sn}_{3-\delta}\text{Pb}_\delta\text{Bi}_2\text{Se}_6$ ($\delta = 0.3$)

	site	x	y	z	sof	U_{eq}
M1	4c	0.3606(1)	0.25	-0.1685(1)	Bi/Sn [0.797(8)/0.203]	20(1)
M2	4c	0.0495(1)	-0.75	-0.1117(1)	Bi/Sn [0.820(8)/0.18]	19(1)
M3	4c	0.1261(1)	0.25	0.1680(1)	Sn/Bi [0.884(7)/0.116]	17(1)
M4	4c	0.4521(1)	-0.75	-0.1070(1)	Sn/Bi [0.721(7)/0.279]	23(1)
M5	4c	0.2655(1)	-0.25	-0.0631(1)	Sn/Pb [0.677(8)/0.323]	38(1)
Se6	4c	0.2440(1)	0.25	0.0763(1)		23(1)
Se7	4c	0.0870(1)	-0.25	0.0180(1)		22(1)
Se8	4c	0.3294(1)	-0.25	0.3044(1)		19(1)
Se9	4c	0.3946(1)	-0.25	0.0175(1)		22(1)
Se10	4c	0.4972(1)	0.25	0.2406(1)		18(1)
Se11	4c	0.1603(1)	-0.25	0.2987(1)		19(1)

Table 2.3d Fractional Atomic Coordinates and Equivalent Isotropic Atomic DisplacementParameters (U_{eq}) in 10^{-3} (\AA^2) and Site Occupancies for $\text{Sn}_{3-\delta}\text{Pb}_\delta\text{Bi}_2\text{Se}_6$ ($\delta = 0.5$)

	site	x	y	z	sof	U_{eq}
M1	4c	0.2619(1)	0.25	0.1671(1)	Bi/Sn [0.718(5)/0.282]	17(1)
M2	4c	0.0497(1)	-0.75	-0.1118(1)	Bi/Sn [0.789(2)/0.211]	15(1)
M3	4c	0.1273(1)	0.25	0.1664(1)	Sn/Bi [0.804/0.196(3)]	17(1)
M4	4c	0.4515(1)	-0.75	-0.1087(1)	Sn/Bi [0.616(8)/0.384]	18(1)
M5	4c	0.2632(1)	-0.25	0.0649(1)	Sn/Pb [0.584(4)/0.416]	38(1)
Se6	4c	0.2451(1)	0.25	0.757(1)		17(1)
Se7	4c	0.0883(1)	-0.25	0.0175(1)		18(1)
Se8	4c	0.3303(1)	-0.25	0.3024(1)		14(1)
Se9	4c	0.3967(1)	-0.25	0.0168(1)		18(1)
Se10	4c	0.4977(1)	0.25	0.2427(1)		13(1)
Se11	4c	0.1614(1)	-0.25	0.2976(1)		14(1)

Table 2.3e. Fractional Atomic Coordinates and Equivalent Isotropic Atomic DisplacementParameters (U_{eq}) in 10^{-3} (\AA^2) and Site Occupancies for $\text{Sn}_{3-\delta}\text{Pb}_\delta\text{Bi}_2\text{Se}_6$ ($\delta = 0.7$)

	site	x	y	z	sof	U_{eq}
M1	4c	0.3655(1)	0.25	0.1646(1)	Bi/Sn [0.492(1)/0.508]	21(1)
M2	4c	0.0498(1)	-0.75	-0.1117(1)	Bi/Sn [0.674(3)/0.326]	19(1)
M3	4c	0.1314(1)	0.25	0.1644(1)	Sn/Bi [0.579/0.421(7)]	25(1)
M4	4c	0.4505(1)	-0.75	-0.1114(2)	Sn/Bi [0.354(4)/0.646]	23(1)
M5	4c	0.2535(1)	-0.25	-0.0676(1)	Sn/Pb [0.334(1)/0.666]	63(1)
Se6	4c	0.2484(1)	0.25	0.0747(1)		24(1)
Se7	4c	0.0929(1)	-0.25	0.0160(1)		24(1)
Se8	4c	0.3328(1)	-0.25	0.2988(1)		18(1)
Se9	4c	0.4030(1)	-0.25	0.0157(1)		25(1)
Se10	4c	0.4994(1)	0.25	0.2481(1)		17(1)
Se11	4c	0.1649(1)	-0.25	0.2971(1)		18(1)

2.1.3 Characterization

X-ray powder diffraction analysis of the products was performed using a Bragg–Brentano-type powder diffractometer (Bruker D8 Advance, operated at 40 kV and 40 mA, Cu K α , $\lambda = 1.5418 \text{ \AA}$). For phase identification, XRD data were collected over a 2θ range from 5° to 90° with a step interval of 0.05° . The bond valence calculations were performed using valence bond theory with R_0 values of 2.59, 2.67, and 2.72 \AA for Sn $^{2+}$, Pb $^{2+}$, and Bi $^{3+}$, respectively⁶⁷.

Energy dispersive spectra (SEM/EDX, Hitachi S-4700I High-Resolution Scanning Electron Microscope) were recorded for the cuboid crystalline samples. Semiquantitative EDS analysis of individual crystals of each reaction product confirmed the presence of Sn, Pb, Bi, and Se. Differential thermal analyzer (DTA) and thermogravimetry (TG) measurements were performed using a thermal analyzer (NETZSCH STA 409PC). A powder sample (approximately 30 mg) was placed in an alumina crucible; Al $_2$ O $_3$ powder served as a reference sample. The sample was heated to 1273 K at 20 K/min under a constant flow of N $_2$.

2.1.4 Physical Property Measurements

Seebeck coefficients were measured on a cold-pressed bar ($1 \times 1 \times 5 \text{ mm}^3$) with a commercial thermopower measurement apparatus (MMR Technologies) over the temperature range 300–500 K under a dynamic vacuum ($\sim 10^{-2}$ Torr). Constantan served as an internal standard and silver conductive paint was used to create electrical contacts. DC conductivity measurements were performed using a standard four-probe method with a homemade device under vacuum ($\sim 10^{-2}$ Torr) over the temperature range 100–300 K. Electrical contacts consisted of four copper wires attached to the bulk with silver glue. Samples were placed under a vacuum for air at least 1 hour to allow the silver glue to dry completely, which improved contact performance. To minimize the effects of grain boundaries in the crystalline

powder on the conductivity measurements, each cold-pressed sample was annealed at 773 K for 72 h before measurement.

2.1.5 Theoretical Calculations

Self-consistent tight-binding linear muffin tin orbital (LMTO) calculations using the atomic spheres approximation (ASA) were undertaken to investigate the electronic structures of these compounds. The density-function theory was applied with the local density approximation (LDA)⁶⁸⁻⁷². The atomic radii used were 1.72, 1.63, and 1.22 Å for Sn, Bi, and Se, respectively. All k -space integrations were performed with the tetrahedron method on $16 \times 16 \times 8$ grids of unique k points in the first Brillouin zone. Within the Brillouin zone based on the primitive cell of $\text{Sn}_3\text{Bi}_2\text{Se}_6$, 288 irreducible k points were used. We analyzed the electronic structure by extracting information from the densities of states (DOS) and the curves for crystal-orbital Hamiltonian populations (COHP)⁷³. To understand the effects of the M5 position and Pb concentration on the electronic structure, stability, and bonding of the as-synthesized compounds, two models were constructed of the electronic structure: (a) $\text{Sn}_3\text{Bi}_2\text{Se}_6$ with the cation sites assigned to Bi(M1, M2) and Sn(M3-M5) in space group $Pnma$, and with the fractional coordinate x of the M5 site ranging from $x = 0.225$ to $x = 0.25$ (on the mirror plane); (b) $\text{Sn}_{3-\delta}\text{Pb}_\delta\text{Bi}_2\text{Se}_6$ ($\delta = 0, 1, \text{ and } 3$) with varied assignments of metal sites. Details of the models are described in Table 2.4.

Table 2.4. Three models with varied assignments of metal sites for LMTO calculations.

	$\text{Sn}_3\text{Bi}_2\text{Se}_6$	$\text{Sn}_2\text{Pb}_1\text{Bi}_2\text{Se}_6$	$\text{Pb}_3\text{Bi}_2\text{Se}_6$
M1	Bi	Bi	Bi
M2	Bi	Bi	Bi
M3	Sn	Sn	Pb
M4	Sn	Sn	Pb
M5	Sn	Pb	Pb
Se6–Se11	Se	Se	Se

2.2 Results and Discussion

2.2.1 Crystal Structure

The crystal structures of compounds **1–5** are closely related to that of lillianite $\text{Pb}_3\text{Bi}_2\text{S}_6$. These as-synthesized phases contain four formulas per unit cell, with eleven crystallographically inequivalent sites: four with mixed-occupancy cations $\text{Sn}^{2+}/\text{Bi}^{3+}$, one with $\text{Sn}^{2+}/\text{Pb}^{2+}$ or fully occupancy Sn^{2+} , and six with Se^{2-} . The structure is illustrated in Figure 2.3 as a projection along the crystallographic b -axis (010). The structure contains two slabs of the same thickness that exhibit NaCl (311) tilt planes expanding along the a, b direction, which are connected by a Se6 atom to form a three-dimensional structure. The same structural feature exists in $\text{KSn}_5\text{Bi}_5\text{Se}_{13}$ ³⁶ and $\text{InSn}_6\text{BiSe}_9$ ⁶³, which contain similar NaCl(311)-type layer units. The lillianite phase $\text{Pb}_3\text{Bi}_2\text{S}_6$ also contains a metal site on the cell-twinning plane showing mirror symmetry. However, the M5 metal sites in the present selenides exhibit a zigzag array along the c -axis with glide symmetry. The coordination environments of the metal sites fall into two groups. (i) The M1-M4 sites are six-coordinate, with two types of distorted octahedral environments. The first type is a square pyramid having one short (~ 2.73 Å), four intermediate ($2.92\text{--}3.02$ Å), and one longer (~ 3.5 Å) bond trans to the shorter M-Se distances. The second type is a trigonal pyramid with three short M-Se bonds ($2.7\text{--}2.9$ Å) opposite to three longer ones ($2.9\text{--}3.1$ Å). (ii) The M5 site is close to the pseudo mirror plane with zigzag arrays along the (001) direction, as shown in Figure 2.3. Its coordination geometry can be described as a monocapped trigonal prism with M5-Se distances varying between $2.861(2)$ and $3.459(1)$ Å. The M-Se distances in both structures are comparable to a binary system and some multinary selenides in the literature that contain mixed occupancies of Bi/Sn or Pb/Sn, such as $\text{Pb}_4\text{Sb}_4\text{Se}_{10}$ ⁷⁴, $\text{Pb}_{0.875}\text{Sn}_{0.125}\text{Se}$ ⁷⁵, PbBi_2Se_4 ⁷⁶, $\text{InSn}_2\text{Bi}_3\text{Se}_8$ ⁶³, and $\text{Sn}_2\text{Pb}_5\text{Bi}_4\text{Se}_{13}$ ⁷⁷.

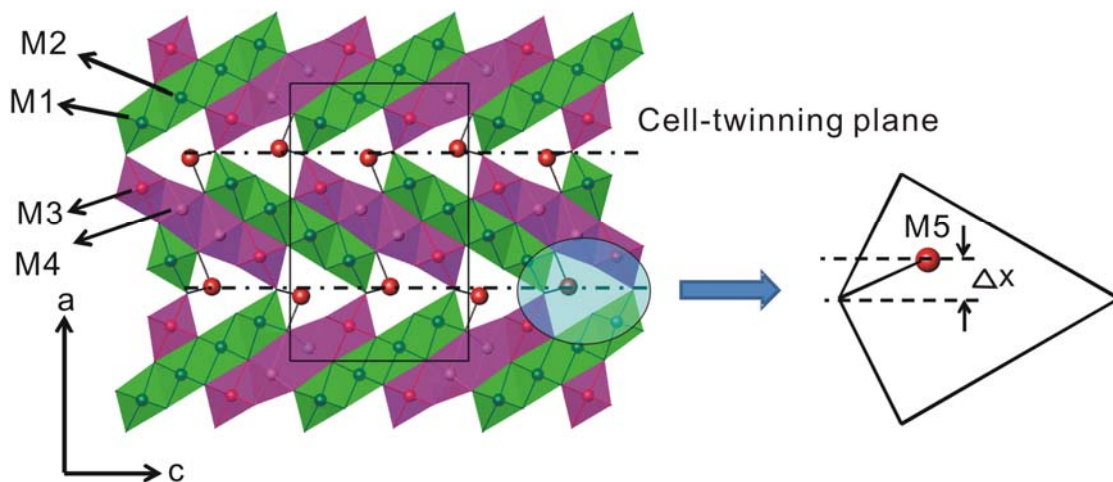
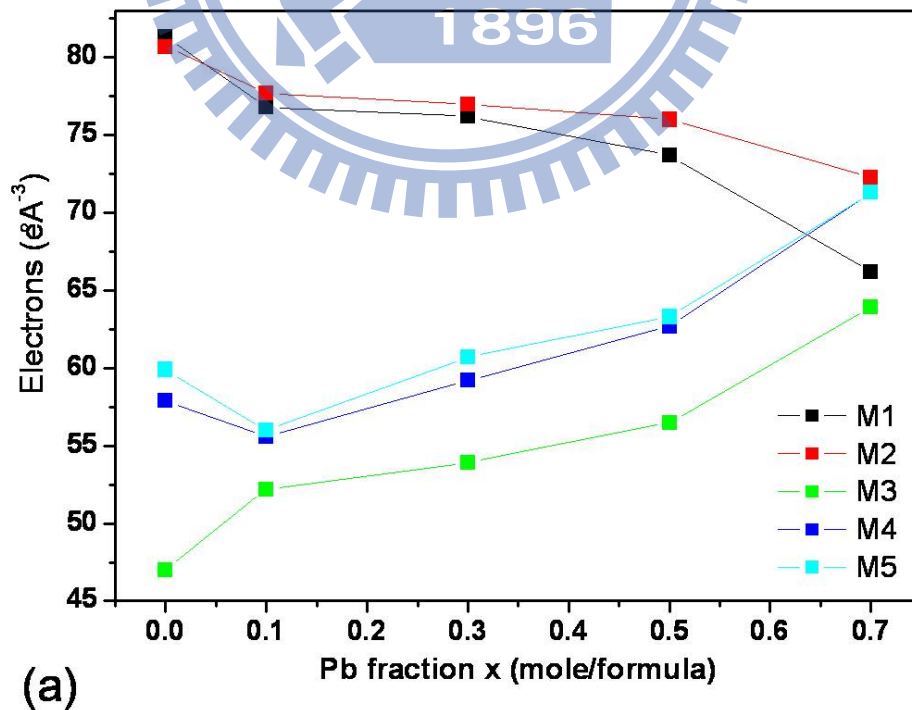


Figure 2.3 The crystal structure of $\text{Sn}_{3-x}\text{Pb}_x\text{Bi}_2\text{Se}_6$ as a projection along the crystallographic b -axis [010]. The slabs exhibit NaCl (311) tilt planes and the atoms along the cell-twinning plane exhibit glide arrayal. Δx indicates the shift in position of the M5 atom from the cell-twinning plane.



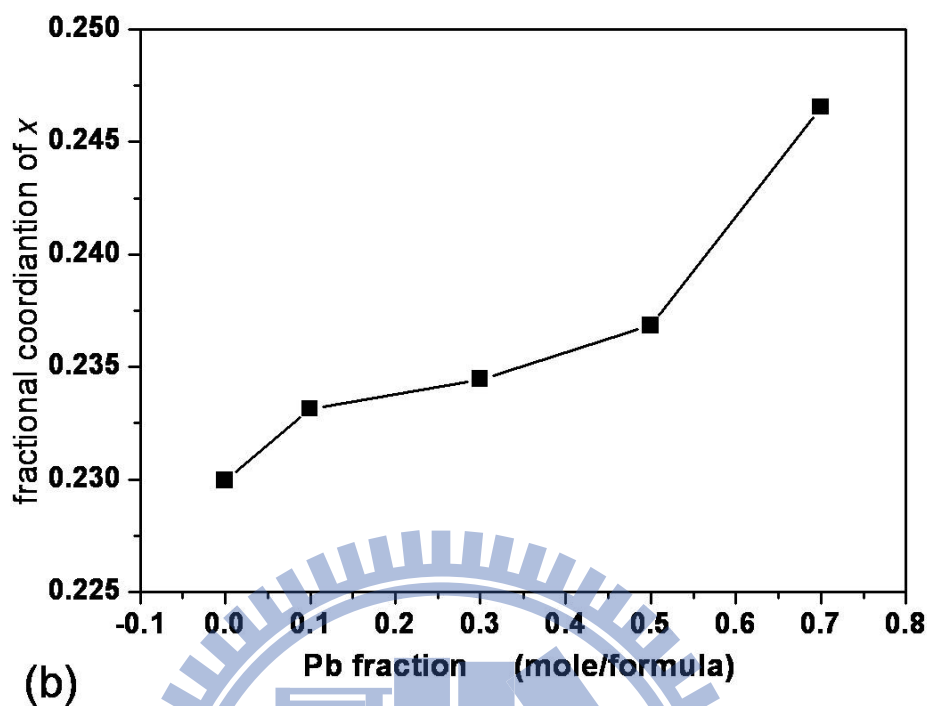


Figure 2.4 The electronic distributions at the five cation sites (a) and variations with the fractional coordinate x of the M5 site (b) in the $\text{Sn}_{3-\delta}\text{Pb}_\delta\text{Bi}_2\text{Se}_6$ ($\delta = 0-0.7$) systems. The standard deviations are smaller than the symbols shown.

The effect of Pb on the electron density of the metal sites and the position of the M5 site was studied and the results are shown in Figure 2.4a. For ternary phase **1** and quaternary phases with a low Pb content, the refined electron count for metal sites fell into two groups with electrons ~ 78 (M1, M2) and ~ 55 e⁻/site (M3, M4, M5), located in different NaCl(311) slab units (Figure 2.3). As the Pb concentration was increased, the electron densities of the M1 and M2 sites decreased, while those of the M3-M5 sites increased (Figure 2.4a). The refined electron count of the metal sites regrouped to (M1, M3) and (M2, M4, M5) with ~ 55 and ~ 65 e⁻/site, respectively, at the highest Pb concentration (**5**, $\delta = 0.7$). Figure 2.4b shows the fractional coordinate x of the M5 sites in the structure of **1-5**. The results indicate that the M5 site gradually shifts to the cell-twinning plane at $x = 0.25$ as the composition of Pb on M5 increases. The interatomic distance of M5-Se9 increased from 2.841(1) Å to 3.377(3) Å and

the fractional coordinate x varied from 0.2300(1) for $\text{Sn}_3\text{Bi}_2\text{Se}_6$ to 0.2465(1) for $\text{Sn}_{2.3}\text{Pb}_{0.7}\text{Bi}_2\text{Se}_6$. Bond valence sum calculations (BVM) clearly indicated that the M5 site of the ternary and Pb-rich quaternary phases approximated the formal oxidation states of Sn^{2+} and Pb^{2+} . Because the single-crystal analysis suggested that the M5 sites are mixed occupied by Bi/Sn(major) and Pb(major)/Sn for ternary and Pb-rich compounds, respectively, the results of the BVM were consistent with the model for the mixed-occupancy M5 site. The other metal sites of compounds **1–5** had calculated valences between 2.89 and 3.40 (M1-M2, Bi-rich) and 2.17 and 2.50 (M3-M4, Sn-rich). Figure 2.3 shows that the paired (M1, M3) and (M2, M4) sites are associated with the pseudo mirror plane at $x = 0.25$. For the Pb-rich phase, the position of the M5 site is close to $x = 0.25$ and the electron densities of (M1, M3) and (M2, M4) were close. The structure may lead to a space group with a mirror plane, such as $Cmcm$, from single-crystal structural analysis.

Table 2.5 Bond valence for $\text{Sn}_{3-\delta}\text{Pb}_\delta\text{Bi}_2\text{Se}_6$ ($\delta = 0 - 0.7$)

δ	element	M1	M2	M3	M4	M5
0	Pb	2.91	2.75	3.10	2.74	2.53
	Bi	3.33	3.15	3.55	3.13	2.89
	Sn	2.34	2.22	2.50	2.21	2.04
0.1	Pb	2.97	2.72	2.97	2.67	2.41
	Bi	3.40	3.11	3.13	2.82	2.76
	Sn	2.39	2.19	2.39	2.15	1.94
0.3	Pb	2.91	2.73	2.97	2.69	2.30
	Bi	3.07	2.88	3.14	2.84	2.43
	Sn	2.34	2.20	2.40	2.17	1.85
0.5	Pb	2.86	2.69	2.92	2.66	2.16
	Bi	3.02	2.84	3.09	2.81	2.28
	Sn	2.31	2.17	2.36	2.14	1.74
0.7	Pb	2.91	2.74	2.95	2.73	2.04
	Bi	3.08	2.89	3.12	2.88	2.16
	Sn	2.35	2.20	2.38	2.20	1.64

2.2.2 Electronic Structure

The effect of the M5 position along the a -axis was studied by varying the fractional coordinate x from 0.225 to 0.25. The relative total energy and ICOHP values for M5-Se as a function of x are shown in Figure 2.5. For relative total energies, the results suggest that the model stabilizes when the x value is shifted away from $x = 0.25$. The most stable model is for $x = 0.2425$, which is close to the observed value of 0.2465 for $\text{Sn}_{2.3}\text{Pb}_{0.7}\text{Bi}_2\text{Se}_6$. When $x < 0.2425$, the repulsive interaction between M5 and Se dominates and the total energy becomes unstable. The calculated ICOHP values can be treated as an index for the interatomic bonding strength; the results shown in Figure 2.5 indicate that the strong-bonding interatomic interactions of the M5-Se contacts gradually increased until $x = 0.23$. The results also suggest that the structure is more stable when the M5 site is shifted away from the mirror plane.

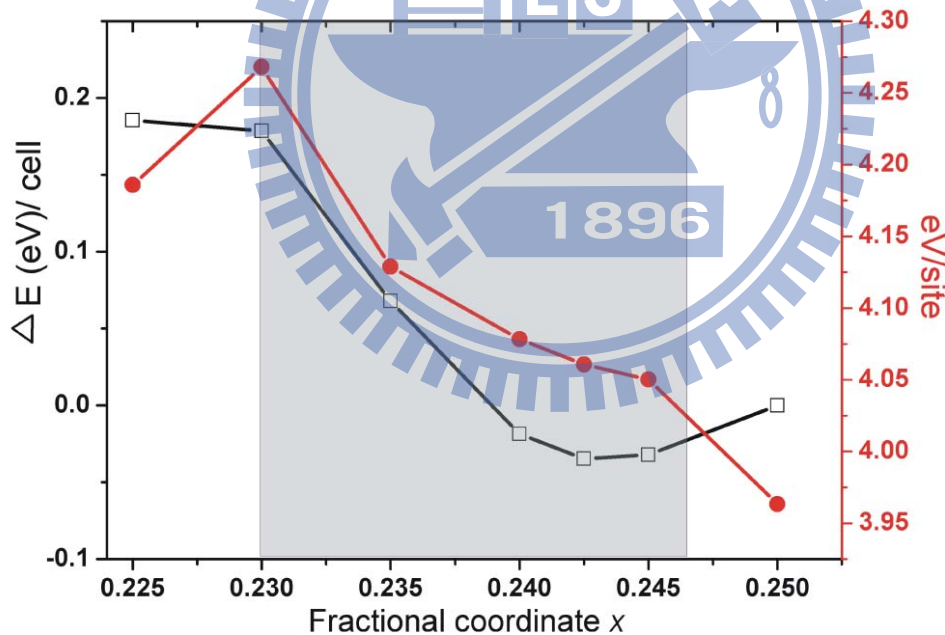


Figure 2.5 Theoretical calculations for the $\text{Sn}_3\text{Bi}_2\text{Se}_6$ model vs. the fractional coordinate x of the M5 sites. The black line is the difference in total energy; the energy at $x = 0.25$ was set to zero for this curve. The blue line shows the ICOHP for the M5 atom vs. fractional coordinate x . The gray area corresponds to single-crystal results for the $\text{Sn}_{3-\delta}\text{Pb}_\delta\text{Bi}_2\text{Se}_6$ ($\delta = 0 - 0.7$) system.

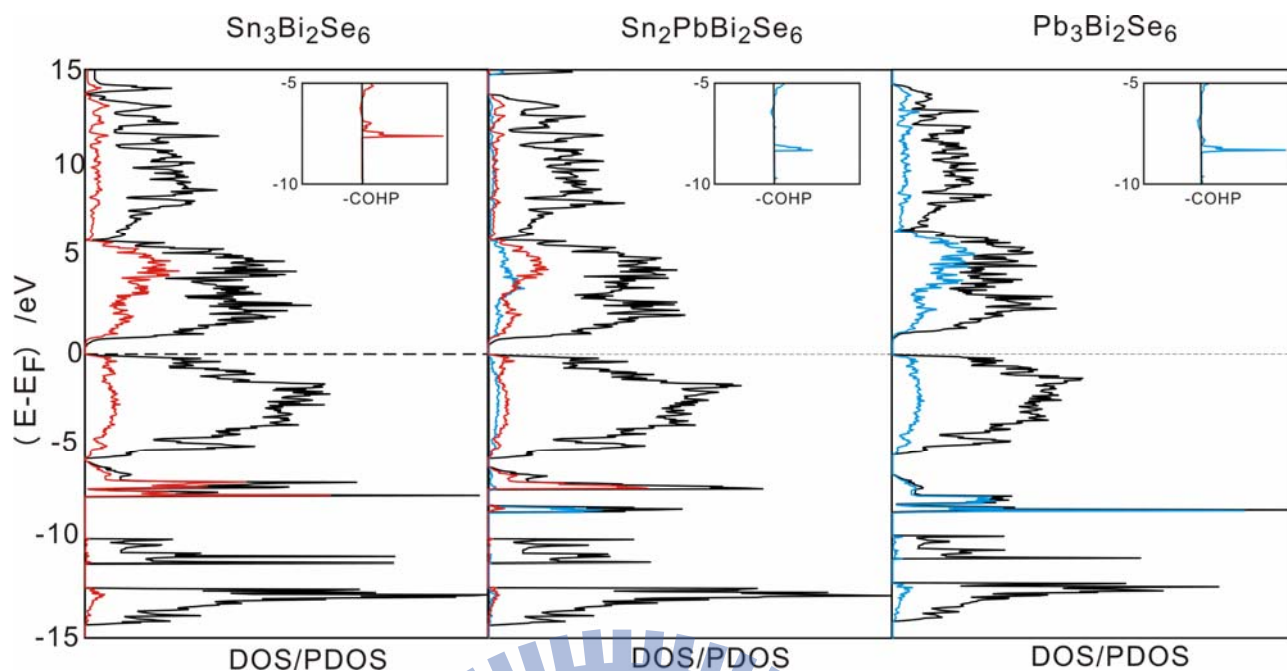


Figure 2.6. Densities of states and partial densities of states for selected M-Se bonds (Sn: red line, Pb: blue line, total DOS: black line) for the $\text{Sn}_3\text{Bi}_2\text{Se}_6$ (left), $\text{Sn}_2\text{PbBi}_2\text{Se}_6$ (middle), and $\text{Pb}_3\text{Bi}_2\text{Se}_6$ (right) models. The horizontal dashed line denotes the Fermi energy (E_F).

Because the model only considers M5-Se bonding, the observed trend for the M5-Se contacts is not the same as the results of the total energy analysis. The results for the total energy and bonding character of M5-Se clearly demonstrate that the favored position of M5 is above or below the cell-twinning plane of the lillianite structure, which indicates why the space group $Pnma$ was chosen rather than $Cmcm$.

The effect of substituting Sn for Pb atoms on the bonding character of the M5-Se contact was also studied (Figure 2.6). In general, as seen from the DOS curve, the valence band was filled for all models with small band gaps (~ 0.4 eV), indicative of semiconducting behavior. Crystal-orbital Hamiltonian population (COHP) calculations are shown in Figure 2.7; the results indicate that the bonding states of the (Sn, Pb, Bi)-Se contacts were occupied and well below the Fermi level, with small contributions of antibonding interactions near the Fermi

level. The large peak between -5 eV and the Fermi level was dominated by the Se p-orbital, whereas the bottom of the conduction band was mainly associated with empty p orbitals of the main-group metal. The *ns* states of the Sn, Pb, and Bi atoms were essentially localized and appeared as sharp peaks centered between -5 and -10 eV, likely resulting from the inert-pair effect commonly observed for heavy main-group elements. Further examination of the projected densities of states (PDOS) curves indicated that the Sn states decreased as the cation sites became gradually replaced with Pb. The PDOS for the M5 site (Figure 2.6) exhibited sharp contributions of Sn(5s) states between -7.5 and -8.5 eV for the M5 site in Sn₃Bi₂Se₆, reduced by ~1 eV in the Sn₂Pb₁Bi₂Se₆ and Pb₃Bi₂Se₆ models in which the M5 site was occupied by Pb. The COHP curves for the M5-Se contacts (insets in Figure 2.6) show differences in the bonding characters of Pb-Se and Sn-Se. The results indicate that the M5-Se bonding states were shifted to a lower energy region due to the strong interaction of the Pb-Se

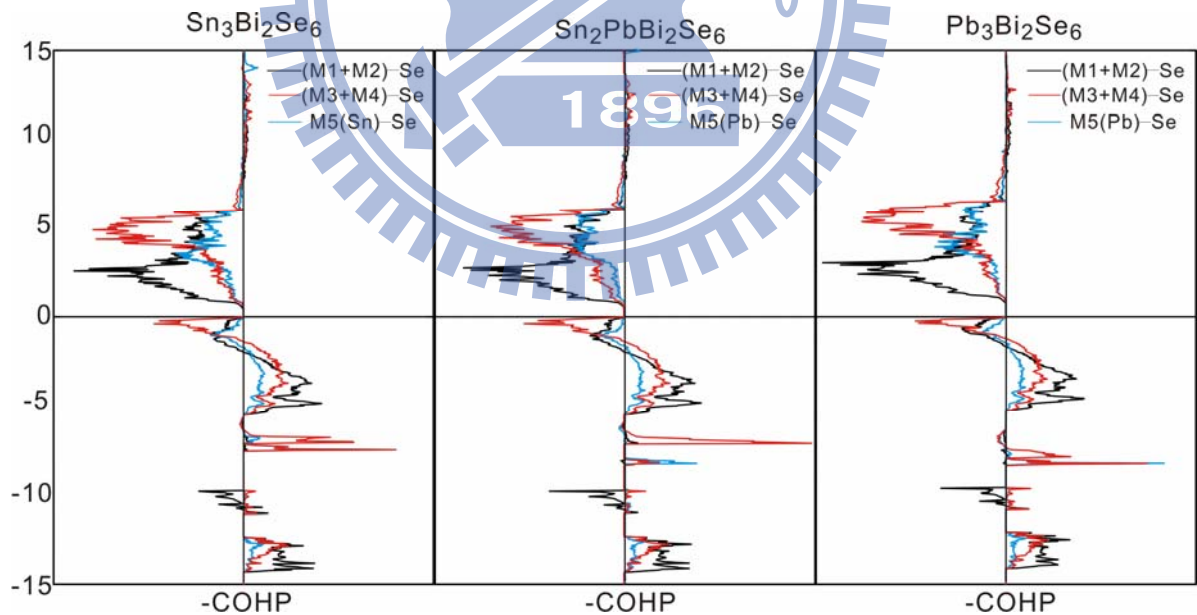
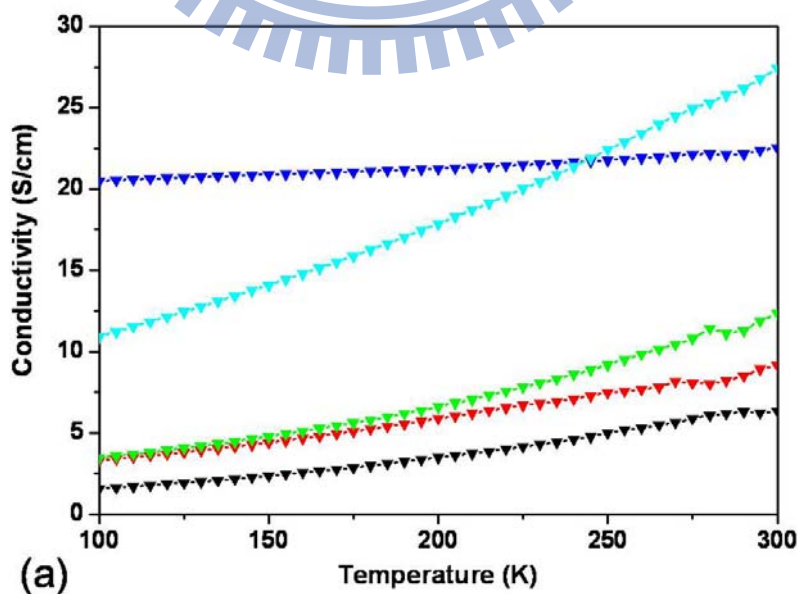


Figure 2.7. Crystal-orbital Hamiltonian populations (COHP) for selected M-Se interaction curves (M1-Se and M2-Se: black line, M3-Se and M4-Se: red line, and M5-Se: blue line) for Sn₃Bi₂Se₆ (left), Sn₂Pb₁Bi₂Se₆ (middle), and Pb₃Bi₂Se₆ (right).

contact. Because the coordination environment of the M5 site remains the same and the ionic radius of Pb^{2+} (1.29 Å) is larger than that of Sn^{2+} (1.22 Å)⁷⁸, the interaction for Pb-Se is expected to be stronger than for Sn-Se contacts. The results are consistent with experimental findings that the quaternary phase $\text{Sn}_{3-\delta}\text{Pb}_\delta\text{Bi}_2\text{Se}_6$ can be synthesized, while the pure ternary phase $\text{Sn}_3\text{Bi}_2\text{Se}_6$ is difficult to synthesize.

2.2.3 Physical Properties

A standard four-probe technique was used to measure the temperature-dependent resistivity from 100 to 300 K. Compounds **1–5** exhibited decreasing resistivity with increasing temperature, consistent with the typical trend for semiconducting property (Figure 2.8a). Compounds **1–5** had negative and nearly temperature-independent thermopower and the maximum observed at $\delta = 0.5$, indicative of n-type semiconducting behavior in which the majority of the charge carriers are electrons (Figure 2.8b). Room-temperature thermopower values are **1**: -53.2, **2**: -116.8, **3**: -77.9, **4**: -148.2, and **5**: -128.4 $\mu\text{V}/\text{K}$, which are too small for thermoelectric applications



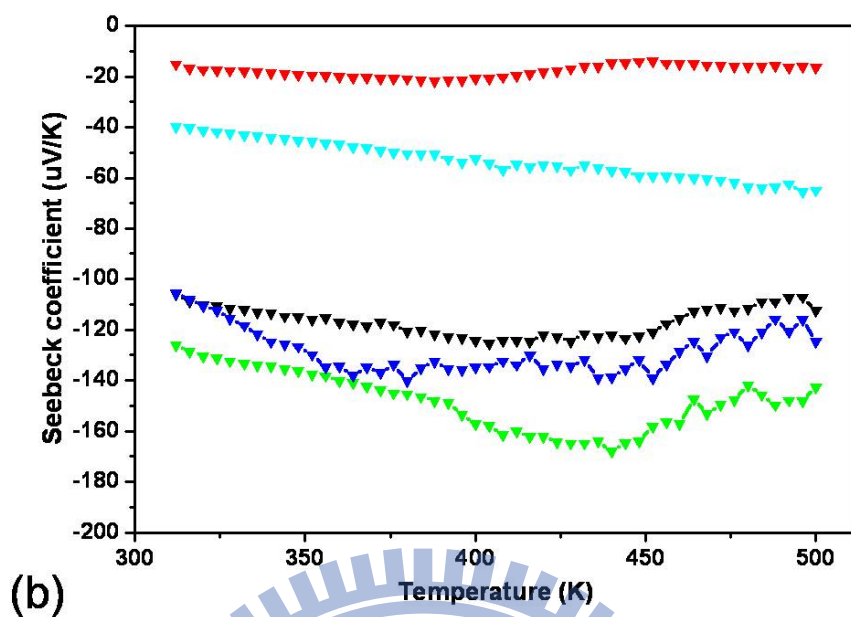


Figure 2.8 Temperature dependence of electrical conductivity (a) and thermoelectric power (b) of $\text{Sn}_{3-\delta}\text{Pb}_\delta\text{Bi}_2\text{Se}_6$ for $\delta = 0$ (light blue), $\delta = 0.1$ (black), $\delta = 0.3$ (red), $\delta = 0.5$ (green) and $\delta = 0.7$ (dark blue).

2.2.4 Thermoanalyses

The TG-DTA vs. temperature spectrum for compound **1** exhibited maximum exothermic peaks at 972 K, corresponding to decomposition of the compound near 1082 K. The quaternary compounds **2–5** had similar results with increased exothermic and decomposition peaks at ~ 1007 K and ~ 1093 K, respectively (Figure 2.9). These results were reproduced by heating the as-synthesized powder in a quartz ampoule under vacuum and subsequently heating to 1173 K. The PXRD pattern of the residual product was indexed as a mixture of SnSe_2 , Bi_2Se_3 , PbSe , and Se phases.

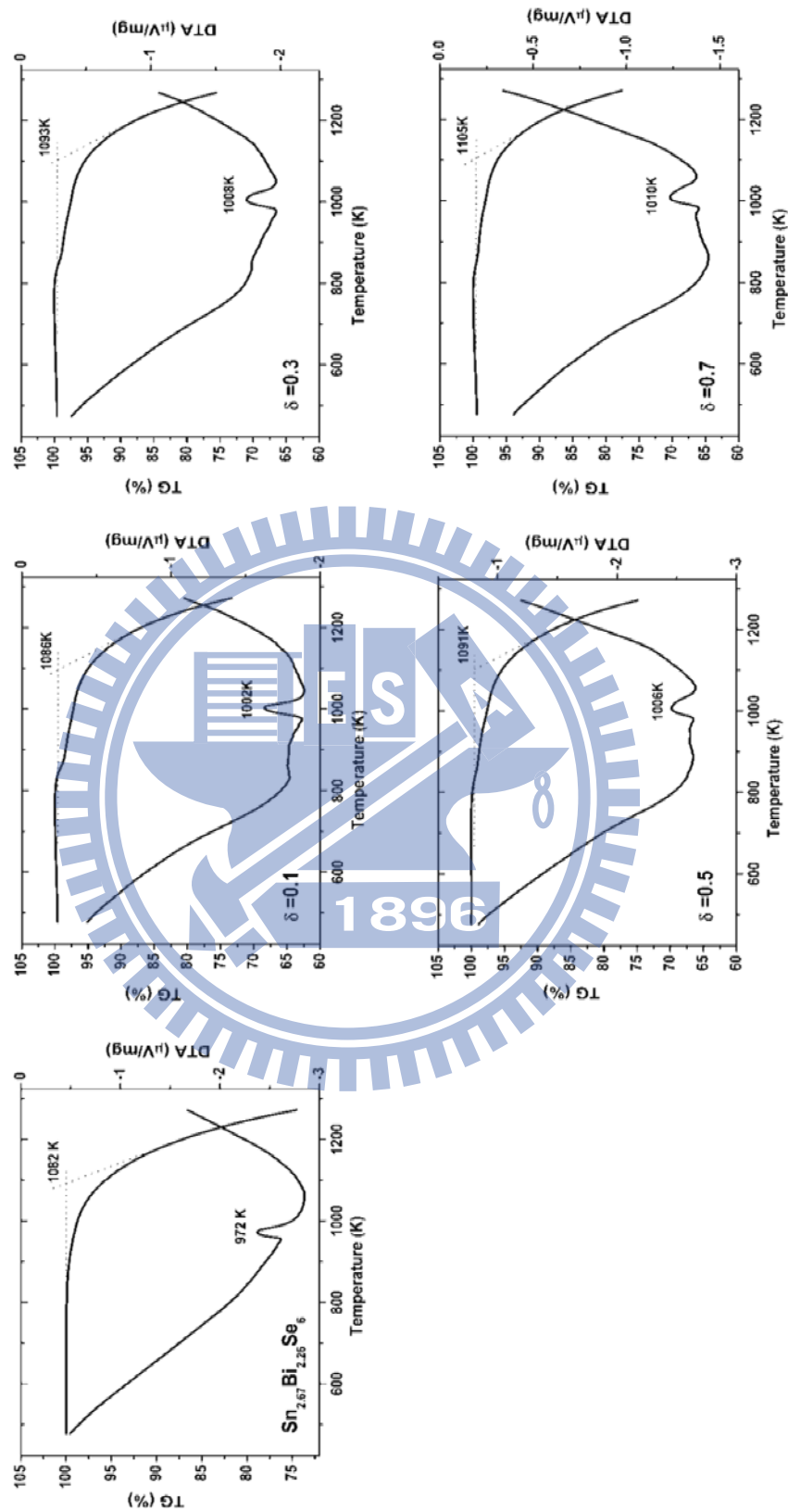


Figure 2.9 Thermal analysis (TG/DTA scans) of $\text{Sn}_{3-\delta}\text{Pb}_\delta\text{Bi}_2\text{Se}_6$ ($\delta = 0, 0.1, 0.3, 0.5, 0.7$)

2.3 Conclusions

This study presents combined experiments and calculations to investigate site preference in the crystal structures of $\text{Sn}_{3-\delta}\text{Pb}_\delta\text{Bi}_2\text{Se}_6$ ($\delta = 0.0\text{--}0.7$). The quaternary selenides $\text{Sn}_{3-\delta}\text{Pb}_\delta\text{Bi}_2\text{Se}_6$ ($\delta = 0.1\text{--}0.7$) contained various amounts of Pb, which affected not only the electron density but also the position of the metal sites. All compounds were *n*-type semiconductors with small band gaps as confirmed by measurements of physical properties and calculation of electronic structures.



Chapter 3

Synthesis and Phase Width of New Quaternary Selenides $\text{Pb}_x\text{Sn}_{6-x}\text{Bi}_2\text{Se}_9$ ($x=0 - 4.36$)

Abstract

Quaternary chalcogenides $\text{Pb}_x\text{Sn}_{6-x}\text{Bi}_2\text{Se}_9$ ($x=0 - 4.36$) were synthesized by solid-state methods, and their structures were determined from X-ray diffraction of single crystals. $\text{Pb}_x\text{Sn}_{6-x}\text{Bi}_2\text{Se}_9$ crystallizes in orthorhombic space group *Cmcm* (No. 62), and the structure features a three-dimensional framework containing slabs of NaCl-(311) type that exhibits identical layers containing seven octahedra unit, which are expanding along direction [010]. Each slab contains fused rectangular units that are connected to each other with M-Se contacts in a distorted octahedral environment. Calculations of the band structure, measurements of Seebeck coefficient and electrical conductivity confirm that these compounds are n-type semiconductors with small band gaps and high electrical conductivities.

3.1 Experiments

3.1.1 Synthesis

All operations were performed in a glove box with a dry nitrogen atmosphere. Chemicals were used as obtained (from Alfa Aesar) – Bi, 99.5 %, powder; Pb, 99.99 %, powder; Sn, 99.9 % powder; Se, 99.95 %, powder. The total masses of samples (all elements combined) were about 0.5 g. All reactants in evacuated fused-silica tubes were placed in resistance furnaces with a controlled temperature. The reaction mixture was heated from 300 K to 1023 K over 8 h; the latter temperature was maintained for 16 h before natural cooling to about 300 K. The product contained a molten part and small particles with a metallic luster. The cuboid shape crystals were chosen for measurements on a single crystal X-ray diffraction.

3.1.2. Single-crystal X-ray diffraction (XRD)

Single crystals of compounds $\text{Pb}_x\text{Sn}_{6-x}\text{Bi}_2\text{Se}_9$ ($x = 0$ (**1**), 0.178 (**2**), 0.436 (**3**)) were mounted on glass fibers with epoxy glue; intensity data were collected on a diffractometer (Bruker APEX CCD) with graphite-monochromated Mo-K α radiation ($\lambda = 0.71073 \text{ \AA}$) at 298(2) K. The distance from the crystal to the detector was 5.038 cm. Data were collected with a scan 0.3° in groups of 600, 435, 600, 435 frames for each at settings 0° , 90° , 180° and 270° , respectively. The duration of exposure was 30 s for both samples; values of 2θ varied between 0.59° and 28.31° . Diffraction signals obtained from all frames of reciprocal space images were used to determine the parameters of the unit cell. The data were integrated (Siemens SAINT Program) and corrected for Lorentz and polarization effects⁶⁵. Absorption corrections were based on a function fitted to the empirical transmission surface as sampled by multiple equivalent measurements of numerous reflections. The structural model was obtained with direct methods and refined with full-matrix

least-square refinement based on F^2 (SHELXTL package)⁶⁶. The atomic occupancy for each metal site was determined from the coordination environment compared with literature.

Crystallographic data and selected bond distances for $\text{Sn}_6\text{Bi}_2\text{Se}_9$, $\text{Pb}_{1.78}\text{Sn}_{4.22}\text{Bi}_2\text{Se}_9$ and $\text{Pb}_{4.36}\text{Sn}_{1.64}\text{Bi}_2\text{Se}_9$ are given in Tables 3.1 – 3.3.

Table 3.1. Crystallographic Data for $\text{Pb}_x\text{Sn}_{6-x}\text{Bi}_2\text{Se}_9$ ($x=0, 1.78, 4.36$)

Empirical formula	$\text{Sn}_6\text{Bi}_2\text{Se}_9$	$\text{Pb}_{1.78}\text{Sn}_{4.22}\text{Bi}_2\text{Se}_9$	$\text{Pb}_{4.36}\text{Sn}_{1.64}\text{Bi}_2\text{Se}_9$
Formula weight	1840.74	1998.27	2226.6
Temperature		300(2) K	
Wavelength		0.71073 Å	
Crystal system		Orthorhombic	
Space group		<i>Cmcm</i> (No.63)	
Unit cell dimensions	$a = 4.206(2)$ Å $b = 13.903(6)$ Å $c = 32.12(1)$ Å	$a = 4.2105(8)$ Å $b = 13.945(3)$ Å $c = 32.174(5)$ Å	$a = 4.2469(7)$ Å $b = 14.073(2)$ Å $c = 32.383(5)$ Å
Volume	1878(1)	1889.1(6)	1935.4(5)
Z		4	
Density (calculated)	6.510 Mg/m ³	7.026 Mg/m ³	7.641 Mg/m ³
Absorption coefficient	43.925 mm ⁻¹	57.161 mm ⁻¹	74.876 mm ⁻¹
F(000)	3088	3316	3646
Crystal size	0.03 x 0.04 x 0.2 mm ³	0.03 x 0.05 x 0.3 mm ³	0.03 x 0.04 x 0.2 mm ³
Reflections collected	4772	9994	11178
Independent reflections	1272 [R(int) = 0.0901]	1357 [R(int) = 0.0466]	1388 [R(int) = 0.0431]
Data / restraints / parameters	1272 / 0 / 56	1357 / 0 / 60	1388 / 0 / 59
Goodness-of-fit on F^2	1.318	1.051	1.097
Final R indices [$I > 2\sigma(I)$]	R1 = 0.0938, wR2 = 0.2685	R1 = 0.0353, wR2 = 0.0930	R1 = 0.0318, wR2 = 0.0773
Largest diff. peak and hole	6.901 and -3.611 e/Å ⁻³	2.817 and -4.928 e/Å ⁻³	3.256 and -3.568 e/Å ⁻³

Table 3.2a. Fractional Atomic Coordinates and Equivalent Isotropic Atomic Displacement Parameters ($U_{eq} / 10^{-3} \text{ \AA}^2$) and Site Occupancies for $\text{Sn}_6\text{Bi}_2\text{Se}_9$

	site	x	y	z	sof	U(eq)
M1	4a	0	0	0.5	Bi/Sn(0.40/0.60)	25(1)
M2	8f	-0.5	-0.2296(2)	0.4426(1)	100%Sn	24(1)
M3	8f	-0.5	-0.0447(2)	0.6180(1)	Bi/Sn(0.60/0.40)	22(1)
M4	8f	0	0.1769(2)	0.6732(1)	Bi/Sn(0.15/0.85)	20(1)
M5	4c	-0.5	0.4109(6)	0.75	Bi/Sn(0.10/0.90)	97(1)
Se6	8f	-0.5	-0.1377(3)	0.5270(1)		23(1)
Se7	8f	0	0.0909(3)	0.5841(1)		22(1)
Se8	4c	0	0.2716(5)	0.75		25(1)
Se9	8f	-0.5	-0.3231(4)	0.3547(2)		31(1)
Se10	8f	-0.5	0.0443(3)	0.6957(1)		24(1)

Table 3.2b. Fractional Atomic Coordinates and Equivalent Isotropic Atomic Displacement Parameters ($U_{eq} / 10^{-3} \text{ \AA}^2$) and Site Occupancies for $\text{Pb}_{1.78}\text{Sn}_{4.22}\text{Bi}_2\text{Se}_9$

	site	x	y	z	sof	U(eq) ^a
M1	4a	0	0	0.5	Pb/Bi/Sn(0.184/0.361/0.455(9))	22(1)
M2	8f	-0.5	-0.2294(1)	0.4423(1)	Pb/Bi/Sn(0.047/0.091/0.862(7))	18(1)
M3	8f	-0.5	-0.0449(1)	0.6182(1)	Pb/Bi/Sn(0.254/0.499/0.247(9))	21(1)
M4	8f	0	0.1783(1)	0.6732(1)	Pb/Bi/Sn(0.116/0.227/0.657(7))	22(1)
M5	4c	-0.5	0.4134(1)	0.75	Pb/Sn(0.76(1)/0.24)	59(1)
Se6	8f	-0.5	-0.1374(1)	0.5269(1)		16(1)
Se7	8f	0	0.0899(1)	0.5842(1)		15(1)
Se8	4c	0	0.2697(1)	0.75		20(1)
Se9	8f	-0.5	-0.3244(1)	0.3544(1)		24(1)
Se10	8f	-0.5	0.0452(1)	0.6953(1)		19(1)

Table 3.2c. Fractional Atomic Coordinates and Equivalent Isotropic Atomic Displacement Parameters ($U_{eq} / 10^{-3} \text{ \AA}^2$) and Site Occupancies for $\text{Pb}_{4.36}\text{Sn}_{1.64}\text{Bi}_2\text{Se}_9$

	site	x	y	z	sof	U(eq)
M1	4a	0	0	0.5	Pb/Bi/Sn(0.529/0.315/0.156(8))	20(1)
M2	8f	-0.5	-0.2294(1)	0.4418(1)	Pb/Bi/Sn(0.389/0.231/0.380(7))	18(1)
M3	8f	-0.5	-0.0450(1)	0.6185(1)	Pb/Bi/Sn(0.577/0.343/0.081(7))	20(1)
M4	8f	0	0.1785(1)	0.6737(1)	Pb/Bi/Sn(0.448/0.267/0.285(7))	21(1)
M5	4c	-0.5	0.4148(1)	0.75	100%Pb	58(1)
Se6	8f	-0.5	-0.1372(1)	0.5273(1)		16(1)
Se7	8f	0	0.0876(1)	0.5849(1)		15(1)
Se8	4c	0	0.2724(1)	0.75		23(1)
Se9	8f	-0.5	-0.3248(1)	0.3542(1)		24(1)
Se10	8f	-0.5	0.0444(1)	0.6957(1)		20(1)

Table 3.3 Interatomic Distances for $\text{Pb}_x\text{Sn}_{6-x}\text{Bi}_2\text{Se}_9$ ($x=0, 1.78, 4.36$)

	$\text{Sn}_6\text{Bi}_2\text{Se}_9$	$\text{Pb}_{1.78}\text{Sn}_{4.22}\text{Bi}_2\text{Se}_9$	$\text{Pb}_{4.36}\text{Sn}_{1.64}\text{Bi}_2\text{Se}_9$	
M1	—Se6×4	2.972(3)	2.9751(8)	3.0032(8)
	—Se7×2	2.979(4)	2.984(1)	3.015(1)
M2	—Se6×2	2.964(4)	2.9771(9)	3.0051(8)
	—Se6	2.996(5)	3.007(1)	3.058(1)
	—Se7×2	2.979(4)	2.9907(9)	3.0405(9)
	—Se9	3.108(2)	3.125(2)	3.139(2)
M3	—Se6	3.200(5)	3.211(1)	3.225(1)
	—Se7×2	3.028(4)	3.0275(9)	3.0288(9)
	—Se9×2	2.926(4)	2.9204(9)	2.9404(9)
	—Se10	2.783(5)	2.780(1)	2.799(1)
M4	—Se7	3.104(5)	3.118(1)	3.146(1)
	—Se8	2.798(4)	2.782(1)	2.802(1)
	—Se9×2	3.059(4)	3.061(1)	3.0922(9)
	—Se10×2	2.889(4)	2.896(1)	2.9292(9)
M5	—Se8×2	2.862(7)	2.906(1)	2.920(1)
	—Se9×2	3.578(2)	3.581(1)	3.604(1)
	—Se10×4	3.299(6)	3.302(1)	3.306(1)

3.1.3 Characterization

X-ray powder diffraction analysis of the products was performed using a Bragg–Brentano-type powder diffractometer (Bruker D8 Advance, operated at 40 kV and 40 mA, Cu $K\alpha$, $\lambda = 1.5418 \text{ \AA}$). For phase identification, XRD data were collected over a 2θ range from 5° to 90° with a step interval of 0.05° . The bond valence calculations were performed using valence bond theory⁶⁷ with R_0 values of 2.59, 2.67, 2.57, and 2.72 \AA for Sn^{2+} , Pb^{2+} , Sb^{3+} and Bi^{3+} , respectively.

Energy dispersive spectra (SEM/EDX, Hitachi S-4700I High-Resolution Scanning Electron Microscope) were recorded for the cuboid crystalline samples. Semiquantitative EDS analysis of

individual crystals of each reaction product confirmed the presence of Sn, Sb, Pb, Bi, and Se. Differential thermal analyzer (DTA) and thermogravimetry (TG) measurements were performed using a thermal analyzer (NETZSCH STA 409PC). A powder sample (approximately 30 mg) was placed in an alumina crucible; Al₂O₃ powder served as a reference sample. The sample was heated to 1273 K at 20 K/min under a constant flow of N₂.

3.1.4 Physical Property Measurements

Seebeck coefficients were measured on a cold-pressed bar (1×1×5 mm³) with a commercial thermopower measurement apparatus (MMR Technologies) over the temperature range 300–500 K under a dynamic vacuum (~10⁻² Torr). Constantan served as an internal standard and silver conductive paint was used to create electrical contacts. DC conductivity measurements were performed using a standard four-probe method with a homemade device under vacuum (~10⁻² Torr) over the temperature range 100–300 K. Electrical contacts consisted of four copper wires attached to the bulk with silver glue. Samples were placed under a vacuum for room temperature at least 1 hour to allow the silver glue to dry completely, which improved contact performance. To minimize the effects of grain boundaries in the crystalline powder on the conductivity measurements, each cold-pressed sample was annealed at 773 K for 72 h before measurement.

3.1.5. Calculation of the Electronic Structure

Band calculations with tight-binding linear muffin-tin orbitals (LMTO) were undertaken to understand the electronic structures⁶⁸⁻⁷². The space group *Cmcm* for Pb_xSn_{6-x}Bi₂Se₉ was used to simulate the observed crystal structures containing mixed-occupancy sites (vide infra). Integration in *k* space was performed with an improved tetrahedron method on grids 16×16×8

unique k points in the first Brillouin zone. We analyzed the electronic structure on extracting information from the band structure, densities of states (DOS), and crystal orbital-hamiltonian population curves (COHP)⁷³.

3.2. Results and discussion

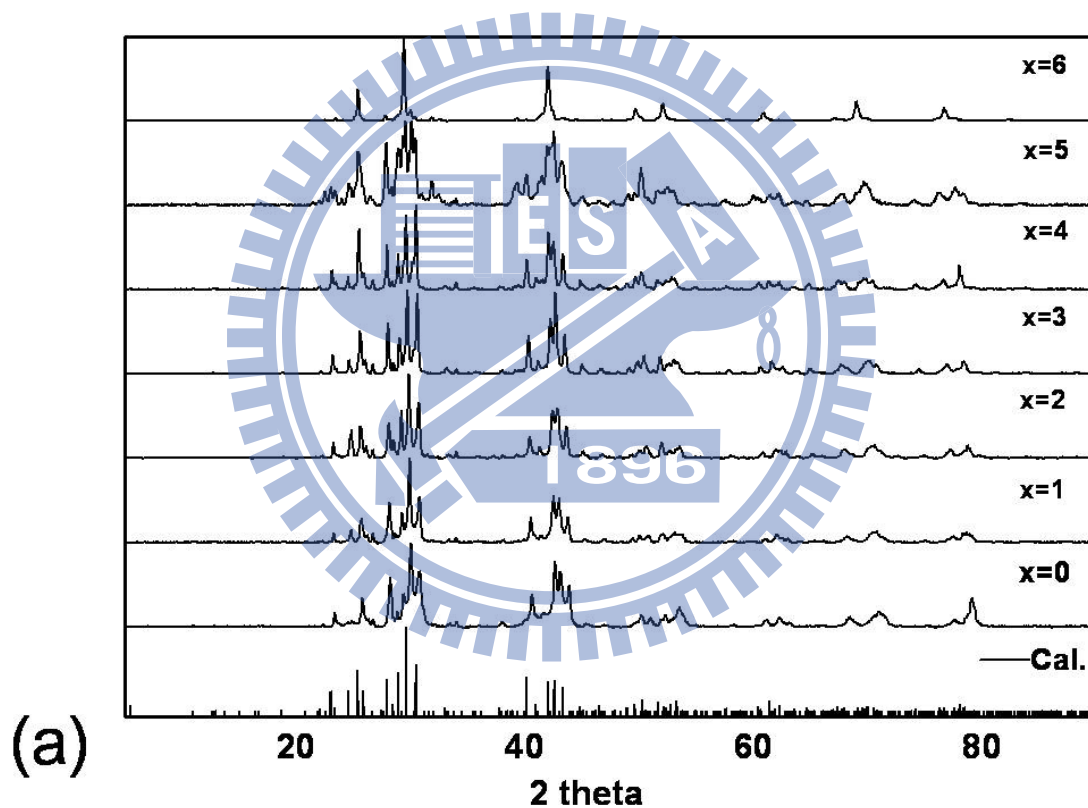
3.2.1 Synthesis and Structure Analysis

Ternary phase $\text{Sn}_6\text{Bi}_2\text{Se}_9$ (**1**) was obtained from experiment with stoichiometric ratio of “ $\text{Sn}_6\text{Bi}_2\text{Se}_9$ ”; and quaternary phases $\text{Pb}_{1.78}\text{Sn}_{4.22}\text{Bi}_2\text{Se}_9$ (**2**) and $\text{Pb}_{4.36}\text{Sn}_{1.64}\text{Bi}_2\text{Se}_9$ (**3**) were initially observed as a product from a reaction with a molar ratio $\text{Pb}:\text{Sn}:\text{Bi}:\text{Se} = 3:1:2:7$ and $3:8:4:17$. The powder X-ray diffraction experiments from the products revealed an unknown phase after searching the JCPDF database. The cuboid shape crystals were chosen for measurements on a single crystal X-ray diffraction. The refined formula “ $\text{Sn}_6\text{Bi}_2\text{Se}_9$ ”, “ $\text{Pb}_{1.78}\text{Sn}_{4.22}\text{Bi}_2\text{Se}_9$ ” and “ $\text{Pb}_{4.36}\text{Sn}_{1.64}\text{Bi}_2\text{Se}_9$ ” were determined, which was used to synthesize the pure phase with same heating conditions as specified above. The experimental X-ray powder-diffraction patterns agreed satisfactorily with patterns simulated based on single-crystal data, confirming the phase purity of the products as synthesized (Figure 3.1a). A series of reactions $\text{Pb}_x\text{Sn}_{7-x}\text{Bi}_2\text{Se}_9$ ($x=0-6$) were performed with the same heating conditions as specified above to investigate the phase width. Based on powder X-ray diffraction, a pure phase of $\text{Pb}_x\text{Sn}_{6-x}\text{Bi}_2\text{Se}_9$ was synthesized in the range $0 \leq x \leq 4$. Unknown and impurity phase of PbSe start to form when $x > 4$. Figure 3.1b shows the refined lattice parameters for $\text{Pb}_x\text{Sn}_{6-x}\text{Bi}_2\text{Se}_9$ ($x = 0-5.0$). In general, the refined lattice parameters were gradually increased as the composition of Pb increased. The lattice parameters for samples with $x > 5.0$ could not be indexed because of impurity PbSe and unknown phase overlapped on powder patterns with the major phase. Compared with single crystal data of $\text{Sn}_6\text{Bi}_2\text{Se}_9$ (**1**), $\text{Pb}_{1.78}\text{Sn}_{4.22}\text{Bi}_2\text{Se}_9$ (**2**) and $\text{Pb}_{4.36}\text{Sn}_{1.64}\text{Bi}_2\text{Se}_9$ (**3**), the cell volume and average bond lengths of M-Se increase with increasing Pb concentration of the compound. This trend is in

consistent to the larger ionic radius of Pb^{2+} (1.29 Å) comparing with Sn^{2+} (1.22 Å)⁷⁹. Other possible variations in the $\text{Pb}_x\text{Sn}_{6-x}\text{M}_2\text{X}_9$ (M = Sb, Bi; X = S and Se) were tested; the products from the reaction contained mixtures of binary PbSe or SnSe or Bi_2Se_3 and an unknown phase. $\text{Sn}_6\text{Bi}_2\text{Se}_9$ (1), $\text{Pb}_{1.78}\text{Sn}_{4.22}\text{Bi}_2\text{Se}_9$ (2) and $\text{Pb}_{4.36}\text{Sn}_{1.64}\text{Bi}_2\text{Se}_9$ (3) revealed orthorhombic C-centered lattice; and the analysis of systematic absence of reflections suggested space group *Cmcm* (No. 63). In structure refinement process, a structural model with five unique sites for metal atoms (Sn, Bi and Pb) and five unique sites for Se atoms was observed. The occupancy parameters were refined along with the displacement parameters. The results show that all Se sites were fully occupied and M1-M5 sites are mixed occupied. It is difficult to quantitative analysis from Pb/Bi due to their similar atomic numbers. Therefore, the $\text{Pb}^{2+}/\text{Bi}^{3+}$ ratio in M1-M4 sites were fixed dependent on charge balance model in quaternary systems. The refined electron densities could give direct evidence on the compositions of M1-M5 sites. The results presented as a function of Pb is shown in Figure 3.2. It is clearly seen that the electron density of M5 site is significantly increased as the Pb element was included in quaternary phase, indicative of site preference for Pb atom. On the other hand, the electron densities of M1-M4 site are gradually increased upon substitution of Pb atom. The results suggest that Pb atom prefer to occupy M5 site and shows no clear preference to occupy M1-M4 sites. Based on the trend from the refined electron densities, the M1-M4 sites were refined with $[(\text{Pb}/\text{Bi}) + \text{Sn}]$ with fixed ratio of Pb/Bi as $X/2$ ($X = 0, 1.78,$ and 3.36), while M5 sites was refined with $[\text{Sn} + \text{Pb}]$. Space groups of low symmetry space groups were used to test if the mixed occupied metal sites could result from an incorrect choice of space group with high symmetry. The results exhibit the same features of split metal sites and the CCD frames of the intensity data revealed no evidence of superstructure reflections.

The final cycle of refinement included anisotropic displacement parameters and a secondary extinction correction performed on F_0^2 . Fourier maps showed featureless residual peaks ~ 6.901 ,

3.256 and 2.82 e-/Å³ close to M5 for compound **1**, **2**, and **3**, respectively. The refined composition are (Sn⁺²)₆(Bi⁺³)₂(Se⁻²)₉ (**1**), (Pb⁺²)_{1.78}(Sn⁺²)_{4.22}(Bi⁺³)₂(Se⁻²)₉ (**2**) and (Pb⁺²)_{4.36}(Sn⁺²)_{1.64}(Bi⁺³)₂(Se⁻²)₉ (**3**), which were in agreement with the reaction compositions. Final structural refinements for all data produced *RI/ wR2/ GOF* = 0.0938/0.2685/1.318, 0.0353/0.0930/1.051 and 0.0318/0.0773/1.097 for **1**, **2** and **3**, respectively.



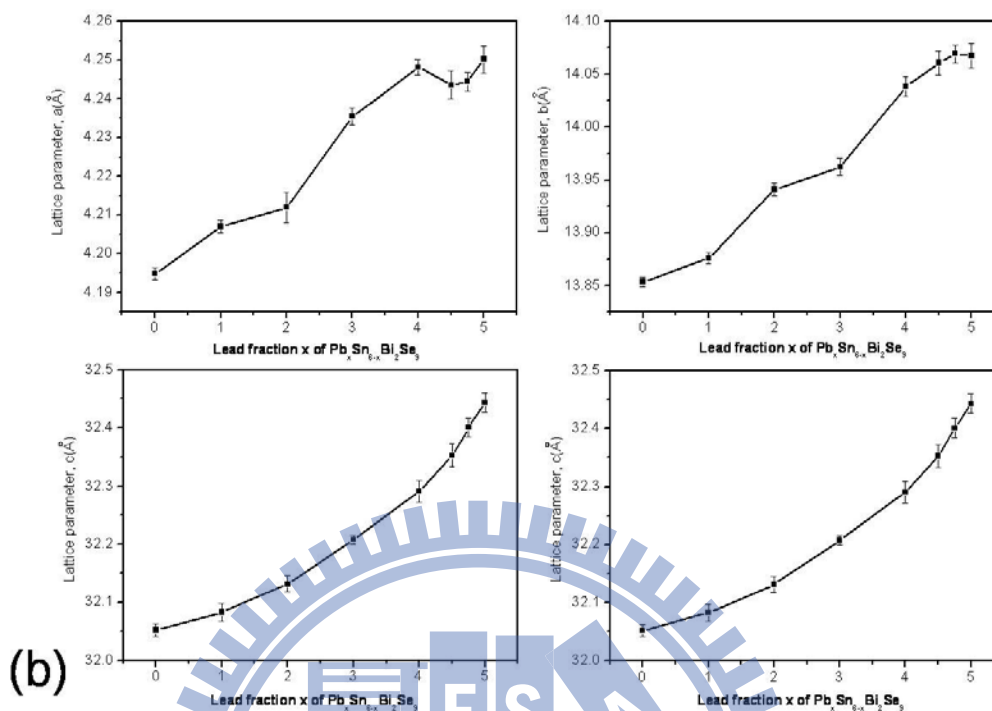


Figure 3.1 (a) Experimental and simulated X-ray powder patterns for $\text{Pb}_x\text{Sn}_{6-x}\text{Bi}_2\text{Se}_9$ ($x=0-6$).
 (b) The unit cell volume and lattice parameters as a function of Lead composition in $\text{Pb}_x\text{Sn}_{6-x}\text{Bi}_2\text{Se}_9$ ($x=0-5$).

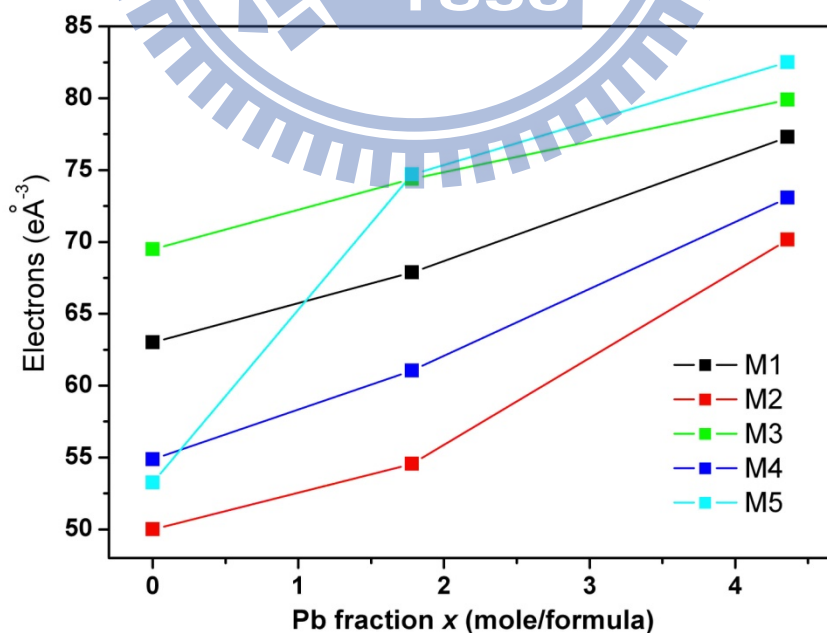


Figure 3.2 The electronic distributions at the five cation sites in the $\text{Pb}_x\text{Sn}_{6-x}\text{Bi}_2\text{Se}_9$ ($x=0-4.36$) systems. The standard deviations are smaller than the symbols shown.

3.2.2 Crystal Structure

$\text{Pb}_x\text{Sn}_{6-x}\text{Bi}_2\text{Se}_9$ is isostructural to the mineral heyrovskyite $\text{Pb}_6\text{Bi}_2\text{S}_9$ that crystallizes in orthorhombic space group *Cmcm* (No. 63) with four formula units per unit cell. The structure contains ten crystallographically inequivalent sites, five for cations (Pb^{2+} , Sn^{2+} , and Bi^{3+}) and five for anions (Se^{2-}). Figure 3.3 shows a [100] projection of the structure that consists of two slabs derived from NaCl (311) tilt planes expanded parallel to the b-axis, which are symmetry related by mirror planes perpendicular to the c-axis ($z = 0, 1/2$) and interconnected by Se atoms running along the c axis. Each slab is composed of fused rectangular rod units that are expanded along direction [100] and connected to each other with M-Se contacts in a distorted octahedral environment. The coordination environment of metal sites can be grouped into three types: (i) Site M1 is hexa-coordinate in a near ideal octahedron with average M-Se distance 3.025 Å, which were refined as mixed occupied with Pb/Bi/Sn. (ii) The coordination polyhedral around M2-M4 sites are distorted octahedral with a square pyramid having five short (2.78-3.06 Å) and one longer (3.12-3.23 Å). This site is mixed occupied Pb/Bi/Sn. (iii) The M5 site is mixed occupied by Pb/Sn atoms, which located on the edge plane of two slabs that exhibits bi-capped trigonal prism coordination environment. The M5-Se distances varying between 2.5 and 3.31 Å in a trigonal prism environment and two long M5-Se contacts between 3.58 and 3.6 Å without bonding interaction.

The M-Se distances in $\text{Pb}_x\text{Sn}_{6-x}\text{Bi}_2\text{Se}_9$ structures are comparable to other systems and some multinary selenide chalcogenides in the literature that contain mixed occupancy of Bi/Sn or Pb/Sn, such as $\text{Pb}_4\text{Sb}_4\text{Se}_{10}$ ⁷⁴, PbBi_2Se_4 ⁷⁶, $\text{InSn}_2\text{Bi}_3\text{Se}_8$ ⁶³, and $\text{Sn}_2\text{Pb}_5\text{Bi}_4\text{Se}_{13}$ ⁷⁷. The distorted octahedral environments are due to the lone pair effect, as observed in similar (Bi/Sb)-Se or (Pb/Sn)-Se contacts for known chalcogenides with Sn, Bi, Pb as the constituent element.

The structures of $\text{Pb}_x\text{Sn}_{6-x}\text{Bi}_2\text{Se}_9$ belong to the lillianite homologous series that are described by

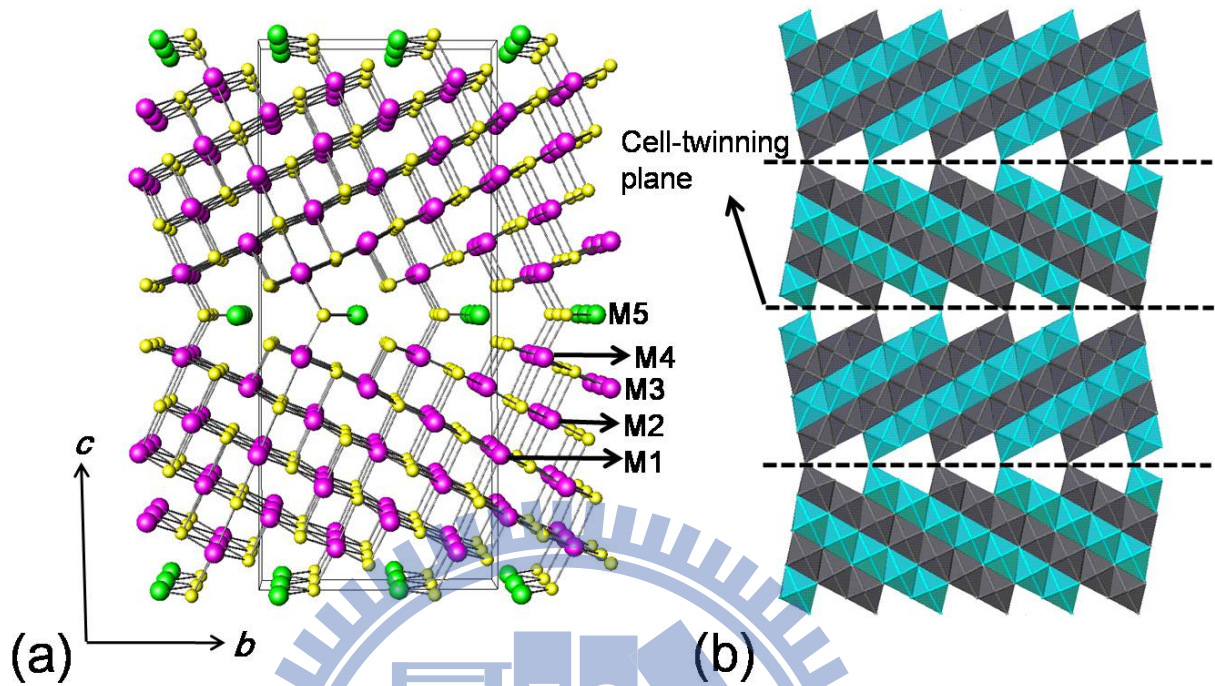


Figure 3.3. Crystal structures of $\text{Pb}_x\text{Sn}_{6-x}\text{Bi}_2\text{Se}_9$ (a) projection along $[100]$ direction with slightly perspective and (b) representation using octahedra chains with the same slab thickness.

the symbol $L n, n'$ where L indicates a member of the lillianite series and n and n' correspond to the number of octahedra between two sides of the topochemical cell-twinning plane. The symbol $L(n, n')$ reflects the cation/anion ratio (M/X). The limit of the ratio M/X is located within 1 (PbS for $L(\infty, \infty)$) and 0.714 (PbBi_4S_7 for $L(2, 1)$). The polysynthetic twinning in NaCl-(311) type exhibits a ratio M/X decreasing with increasing the number of octahedral n . In the same way that the symbol $L(7, 7)$ can be assigned for $\text{Pb}_x\text{Sn}_{6-x}\text{Bi}_2\text{Se}_9$ ($M/X = 0.889$). Therefore, the structure can be considered as a three-dimensional framework containing slabs of NaCl-(311) type that exhibits identical layers of 7 octahedra wide slabs expanding along direction $[010]$.

3.2.3. Electronic Structure

Since the $\text{Pb}_x\text{Sn}_{6-x}\text{Bi}_2\text{Se}_9$ phase exhibits phase width with varied composition of Pb/Sn, we constructed three models with varied assignments of Pb, Bi and Sn in M1-M5 sites to performed calculations of the electronic structure (Table 3.5). These models generate hypothetical formulae $\text{Sn}_6\text{Bi}_2\text{Se}_9$ (1), $\text{Pb}_3\text{Sn}_3\text{Bi}_2\text{Se}_9$ (2) and $\text{Pb}_6\text{Bi}_2\text{Se}_9$ (3), respectively. Curves for the total and partial densities of states (DOS, PDOS) for these models appear in Figure 3.4. The calculated band structures show direct band gaps for all models, indicative of filled valence bands with semiconducting property. The electronic states near the Fermi level (E_F) are composed of mostly Pb(6p), Bi(6p) and Sn(5p) states. The large feature between -5 eV and the Fermi level is dominated by Se (3p) and Sn/Pb (5p/6p) states. The sharp features at -10 and -6 eV are from the filled *ns* state of Pb and Sn atoms.

Table 3.5. Three models with varied assignment of metal sites for the LMTO calculations.

	$\text{Sn}_6\text{Bi}_2\text{Se}_9$	$\text{Sn}_3\text{Pb}_3\text{Bi}_2\text{Se}_9$	$\text{Pb}_6\text{Bi}_2\text{Se}_9$
M1	Sn	Sn	Pb
M2	Sn	Sn	Pb
M3	Bi	Bi	Bi
M4	Sn	Pb	Pb
M5	Sn	Pb	Pb
Se6 – Se10	Se	Se	Se

The interatomic interactions were analyzed with ICOHP values by integrating the area of the COHP curves (Table S2). All calculated models in M3 site were fixed with Bi because of largest Bi occupancy and bonding strength (Bi-Se = 5.49eV) compared with other sites (M1, M2, M4 and M5) and other bonding models (M3 = Pb or Sn), respectively.

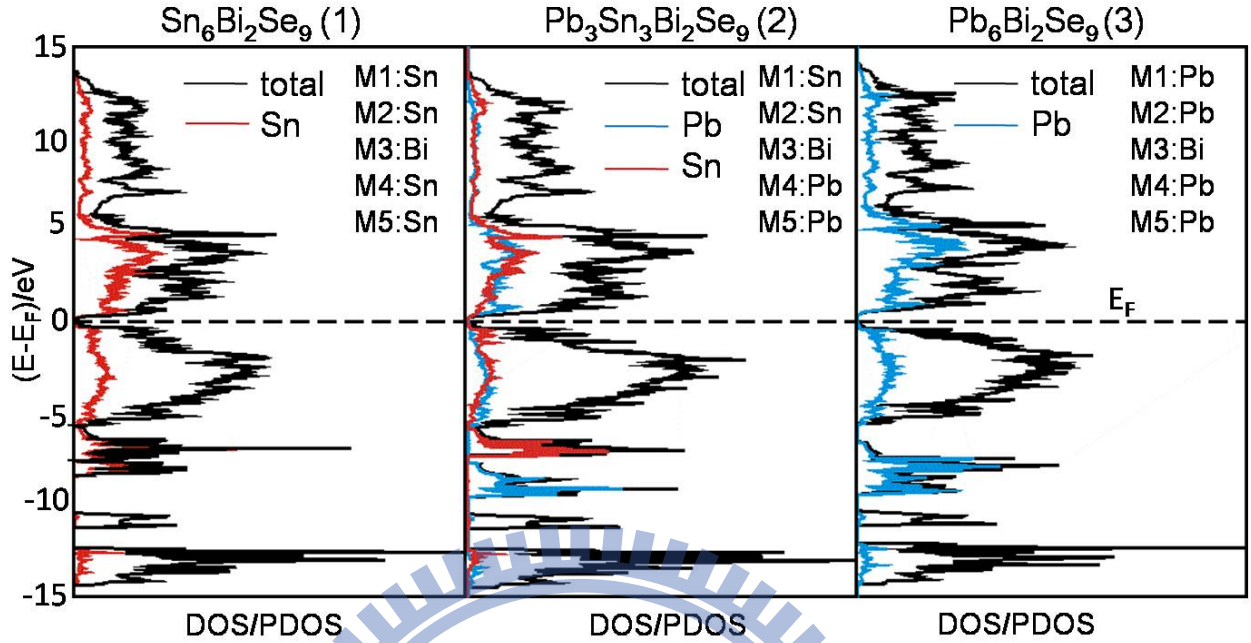


Figure 3.4 DOS/PDS for series of models: $\text{Pb}_{6-x}\text{Sn}_x\text{Bi}_2\text{Se}_9$ ($x = 0, 3, 6$). The black, red, and blue lines refer to total, Sn and Pb atoms, respectively. The horizontal dashed line denotes the Fermi energy (E_F).

For M-Se ($M = \text{M1}, \text{M2}, \text{M4}$ and M5) contact, the ICOHP indicative of a similar bonding strength for Pb and Sn models that might be exchanged Sn/Pb to keep the structure stable, especially in M5-Se ($\text{Sn-Se/Pb-Se} = 4.21/4.17$ eV per site) that has largest tolerance and is identical to experimental results.

The average ICOHP for M-Se ($M = \text{M1}, \text{M2}, \text{M4}$ and M5) contact for $\text{Sn}_6\text{Bi}_2\text{Se}_9$ (ICOHP = 4.25) is greater than for $\text{Pb}_6\text{Bi}_2\text{Se}_9$ (ICOHP = 4.00), indicative of strong bonding strength for Sn-Se compared with Pb-Se contact. The results are in consistent with the experiments that ternary phases $\text{Sn}_6\text{Bi}_2\text{Se}_9$ can be synthesized, while pure ternary phase $\text{Pb}_6\text{Bi}_2\text{Se}_9$ is difficult to be synthesized and suggest a possible phase width that could be controlled by molar ratio Pb/Sn.

Table 3.6 ICOHP values by integrating the area of the COHP curves.

	$\text{Sn}_6\text{Bi}_2\text{Se}_9$	$\text{Sn}_3\text{Pb}_3\text{Bi}_2\text{Se}_9$	$\text{Pb}_6\text{Bi}_2\text{Se}_9$
M1	4.17	4.17	3.82
M2	3.98	3.98	3.70
M3	5.49	5.49	5.49
M4	4.65	4.32	4.32
M5	4.21	4.17	4.17

3.2.4 Physical Properties

A standard four-probe technique was used to measure the temperature-dependent resistivity from 100 to 300 K. The variation of specific electrical conductivities of $\text{Pb}_x\text{Sn}_{6-x}\text{Bi}_2\text{Se}_9$ ($x=0, 2$ and 4 for i, ii, and iii, respectively) with temperature is shown in Figure 3.5a. The results exhibited decreasing resistivity with increasing temperature slightly, consistent with the typical trend for semiconducting property. For these compounds, the resistivity decreased with increasing Pb composition; while the quaternary phase $\text{Pb}_4\text{Sn}_2\text{Bi}_2\text{Se}_9$ (iii) exhibited the largest conductivity at room temperature. The energy gaps of $\text{Pb}_x\text{Sn}_{6-x}\text{Bi}_2\text{Se}_9$ are measurement using diffuse reflectance spectra in the region $4000\text{-}400\text{ cm}^{-1}$, but both compound's band gap were too small to out of the measurement range. This could be due to the mid-gap states which derived from great mixed sites by aliovalent elements such as Sn/Bi or Pb/Bi⁸⁰. Compounds i –iii had negative and nearly temperature-independent thermopower, indicative of n-type semiconducting behavior in which the majority of the charge carriers are electrons (Figure 3.5b). Room-temperature thermopower values were i: -49.4, ii: -42.4 and iii: -26.1 $\mu\text{V/K}$, which were too low to be useful for TE applications.

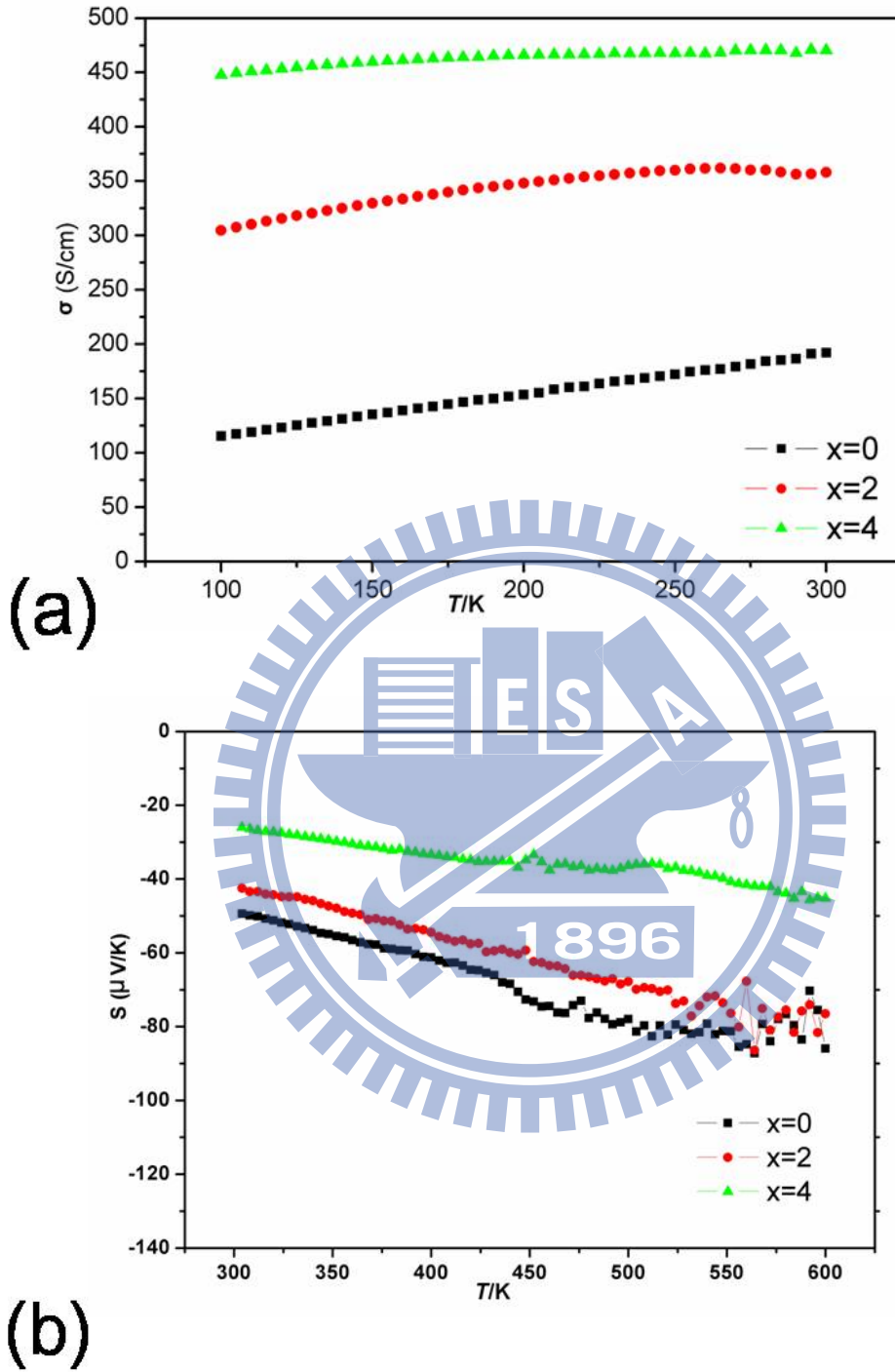


Figure 3.5 Temperature dependence of electrical conductivity (a) and thermoelectric power (b) of $\text{Pb}_x\text{Sn}_{6-x}\text{Bi}_2\text{Se}_9$ ($x=0, 2$ and 4).

3.2.5 Thermoanalyses

The TG-DTA vs. temperature curve for solid solution compounds $\text{Pb}_x\text{Sn}_{6-x}\text{Bi}_2\text{Se}_9$ ($x=0, 2$ and 4) had similar results with increased exothermic and decomposition peaks at ~ 1115 K and ~ 1010 K, respectively (Figure 3.6). These results were reproduced by heating the as-synthesized powder in a quartz ampoule under vacuum and subsequently heating to 1173 K. The PXRD pattern of the residual product was indexed as a mixture of SnSe_2 , PbSe , Bi_2Se_3 , and Se phases.

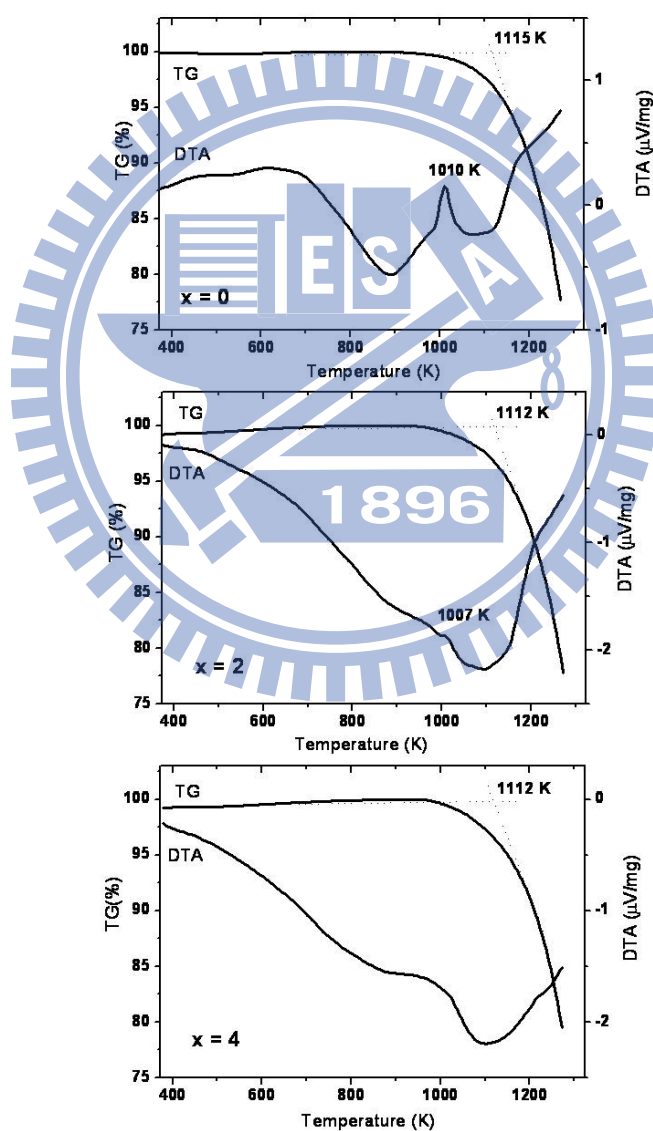


Figure 3.6 Thermal analysis (TG/DTA scans) of $\text{Pb}_{6-x}\text{Sn}_x\text{Bi}_2\text{Se}_9$ ($x=0, 2$ and 4)

3.3 Conclusions

In this study, solid-solution $\text{Pb}_x\text{Sn}_{1-x}\text{Bi}_2\text{Se}_9$ ($x=0 - 4.36$) were synthesized and characterized. The structure of $\text{Pb}_x\text{Sn}_{6-x}\text{Bi}_2\text{Se}_9$ belong to mineral, heyrovskyite that contains slab units cut from NaCl structure parallel to the (311) plane. As confirmed by measurements of physical properties and calculation of electronic structures, these phases are n-type semiconductors with small band gaps and high electrical conductivities.



Chapter 4

Synthesis and Characterization of Quaternary Selenides $\text{Sn}_2\text{Pb}_5\text{Bi}_4\text{Se}_{13}$ and $\text{Sn}_{8.65}\text{Pb}_{0.35}\text{Bi}_4\text{Se}_{15}$

Abstract

Quaternary selenides $\text{Sn}_2\text{Pb}_5\text{Bi}_4\text{Se}_{13}$ and $\text{Sn}_{8.65}\text{Pb}_{0.35}\text{Bi}_4\text{Se}_{15}$ were synthesized from the elements in sealed silica tubes; their crystal structures were determined by single-crystal X-ray diffraction. Both compounds crystallize in monoclinic space group $C2/m$ (No.12), with lattice parameters of $\text{Sn}_2\text{Pb}_5\text{Bi}_4\text{Se}_{13}$: $a = 14.001(6) \text{ \AA}$, $b = 4.234(2) \text{ \AA}$, $c = 23.471(8) \text{ \AA}$, $V = 1376.2(1) \text{ \AA}^3$, $R_1/wR_2 = 0.0584/0.1477$, and $GOF = 1.023$; $\text{Sn}_{8.65}\text{Pb}_{0.35}\text{Bi}_4\text{Se}_{15}$: $a = 13.872(3) \text{ \AA}$, $b = 4.2021(8) \text{ \AA}$, $c = 26.855(5) \text{ \AA}$, $V = 1557.1(5) \text{ \AA}^3$, $R_1/wR_2 = 0.0506/0.1227$, and $GOF = 1.425$. These compounds exhibit topochemical cell-twinning of NaCl-type structures with lillianite homologous series $L(4, 5)$ and $L(4, 7)$ for $\text{Sn}_2\text{Pb}_5\text{Bi}_4\text{Se}_{13}$ and $\text{Sn}_{8.65}\text{Pb}_{0.35}\text{Bi}_4\text{Se}_{15}$, respectively. Measurements of electrical conductivity indicate that these materials are semiconductors with narrow band gaps; $\text{Sn}_2\text{Pb}_5\text{Bi}_4\text{Se}_{13}$ is n -type, whereas $\text{Sn}_{8.65}\text{Pb}_{0.35}\text{Bi}_4\text{Se}_{15}$ is a p -type semiconductor with Seebeck coefficients $-80(5)$ and $178(7) \mu\text{V/K}$ at 300K, respectively.

4. Experiments

4.1.1. Synthesis

All compounds were performed in a glove box under a dry nitrogen atmosphere. Chemicals were used as obtained (from Alfa Aesar) – Bi, 99.95 %, powder; Sn, 99.5 %, powder; Pb, 99.9 %, powder; Se, 99.95 %, powder. The total masses of samples (all elements combined) were about 0.5 g. All reactants in evacuated fused-silica tubes were placed in a resistance furnace with controlled temperature.

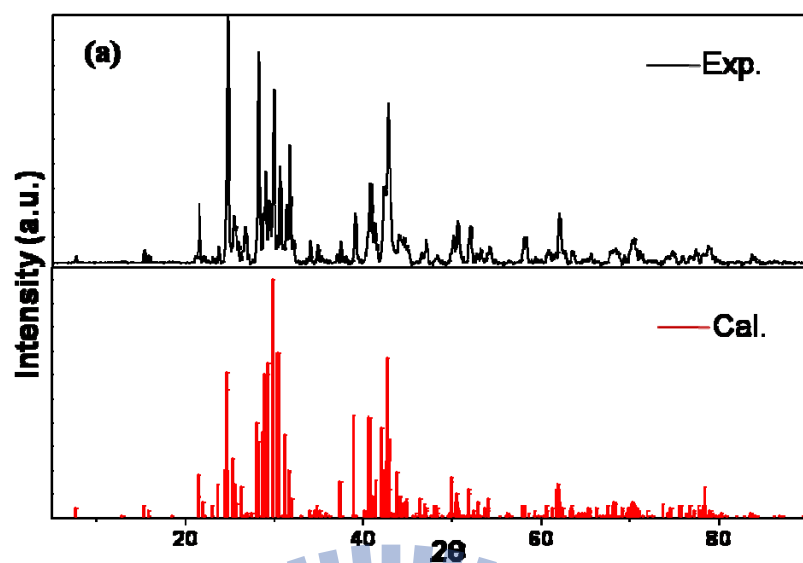
(a) $\text{Sn}_2\text{Pb}_5\text{Bi}_4\text{Se}_{13}$

$\text{Sn}_2\text{Pb}_5\text{Bi}_4\text{Se}_{13}$ was initially observed from a reaction intended to synthesize ‘ $\text{Sn}_{0.8}\text{Pb}_{2.2}\text{Bi}_2\text{Se}_6$ ’. The reaction mixture was heated slowly to 1073 K over 12 h. This temperature was maintained for 18 h, followed by slow cooling to 773 K over 12 h, and finally to about 300 K on simply terminating the power. The product, observed under an optical microscope, contained a molten part and cuboid-shaped crystals. Measurements of powder X-ray diffraction of the product of the ‘ $\text{Sn}_{0.8}\text{Pb}_{2.2}\text{Bi}_2\text{Se}_6$ ’ reaction revealed mixtures of $\text{Pb}_2\text{Bi}_2\text{Se}_5$ ⁸¹, $\text{Sn}_3\text{Bi}_9\text{Se}_{13}$ ⁸² and an unknown phase. Some cuboid-shaped crystals were chosen for measurements with single-crystal X-ray diffraction; the crystal structure was determined with a refined composition near $\text{Sn}_2\text{Pb}_5\text{Bi}_4\text{Se}_{13}$. Reactions with varied ratios Sn/Pb in $\text{Sn}_x\text{Pb}_{7-x}\text{Bi}_4\text{Se}_{13}$ ($x = 0, 2, 4, 6, 7$) were utilized to probe the possible phase width with the same heating conditions as specified above. The products of each reaction displayed silvery, brittle ingots that were sensitive to neither air nor moisture. Analyses by powder X-ray diffraction and energy-dispersive spectra (EDX) revealed a pure phase from reaction ‘ $\text{Sn}_2\text{Pb}_5\text{Bi}_4\text{Se}_{13}$ ’. The products from the other reactions comprised mixtures of SnSe_2 ⁸³, PbSe ⁸⁴, Bi_2Se_3 ⁸⁵ and $\text{Sn}_{0.57}\text{Bi}_{0.28}\text{Se}$ ⁸⁶. Attempts to synthesize a quaternary phase $\text{Sn}_2\text{Pb}_5\text{M}_4\text{X}_{13}$ (M = Sb, Bi; X = S, Se) failed; the product yielded only known phases of SnBi_2S_4 ⁸⁷, $\text{Pb}_2\text{Bi}_2\text{S}_5$ ⁸⁸, PbSe ⁸⁴, PbSb_2Se_4 ⁸⁹ and a minor unknown phase.

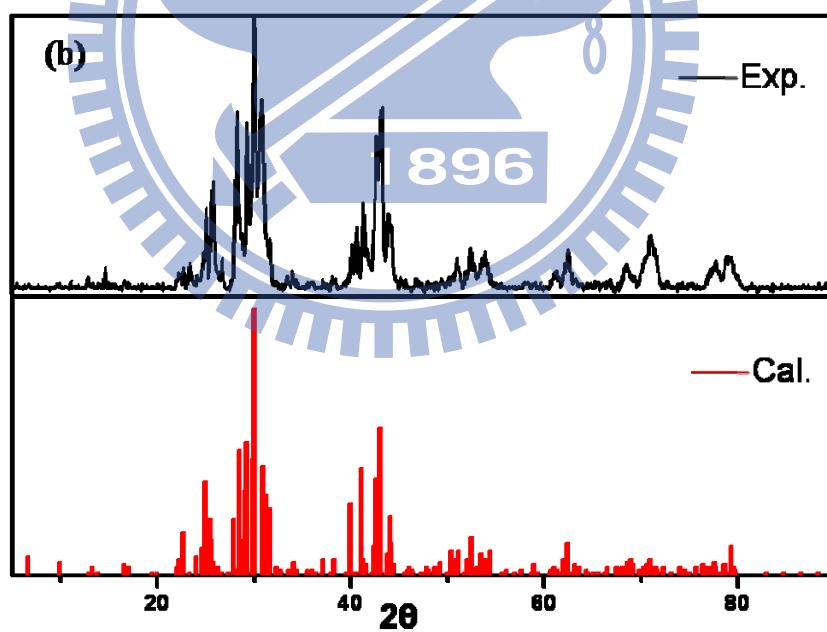
(b) $\text{Sn}_{8.65}\text{Pb}_{0.35}\text{Bi}_4\text{Se}_{15}$

$\text{Sn}_{8.65}\text{Pb}_{0.35}\text{Bi}_4\text{Se}_{15}$ was initially observed from a reaction intended to synthesize ‘ $\text{Sn}_{2.9}\text{Pb}_{0.1}\text{Bi}_2\text{Se}_6$ ’, with heating conditions the same as specified above. The product contained a molten ingot with cuboid-shaped crystals. Measurements with powder X-ray diffraction indicated that this product contained mixtures of $(\text{Sn}_x\text{Pb}_{1-x})_3\text{Bi}_2\text{Se}_6$ and an unknown phase. Measurements of single-crystal X-ray diffraction on a cuboid-shaped crystal revealed a quaternary phase with refined formula $\text{Sn}_{8.65}\text{Pb}_{0.35}\text{Bi}_4\text{Se}_{15}$. Reactions with varied ratios Sn/Pb in $\text{Sn}_{9-x}\text{Pb}_x\text{Bi}_4\text{Se}_{15}$ ($x = 0, 0.35, 0.5, 1, 9$) were utilized to probe the possible phase width using the same heating conditions as specified above. The products from each reaction revealed silvery, brittle ingots that were stable in air. According to measurements of powder X-ray diffraction and energy-dispersive spectra (EDX), the pure phase was observed from only the reaction ‘ $\text{Sn}_{8.65}\text{Pb}_{0.35}\text{Bi}_4\text{Se}_{15}$ ’. The products of other reactions contained mixtures of $\text{Sn}_{0.57}\text{Bi}_{0.28}\text{Se}^{86}$, PbSe^{84} , $\text{Bi}_2\text{Se}_3^{85}$ and $\text{PbBi}_2\text{Se}_4^{76}$. When other possible variations of $\text{Sn}_{8.65}\text{Pb}_{0.35}\text{M}_4\text{X}_{15}$ ($\text{M} = \text{Sb}, \text{Bi}; \text{X} = \text{S}, \text{Se}$) were tested, the products in each case contained mixtures of PbSe^{84} , $\text{Sn}_{17}\text{Bi}_6\text{S}_{29}^{90}$, $\text{Sn}_4\text{Sb}_4\text{Se}_{10}^{91}$ and $\text{Sn}_2\text{Sb}_2\text{S}_5^{92}$.

Because the compound $\text{Sn}_2\text{Pb}_5\text{Bi}_4\text{Se}_{13}$ as synthesized is near the reported phase of $\text{KSn}_5\text{Bi}_4\text{Se}_{13}^{36}$, additional reactions were performed with various containers (graphite, alumina and tantalum) to avoid a possible contamination of alkali-metal cations (e.g. K^+ , Na^+) from the silica tube; these containers were sealed inside silica tubes under vacuum and heated under the same conditions as specified above. Pure phases of the title compounds were observed; elemental analyses (EDX) show no signal from alkali metals (Na, K) in the products. Both compounds are stable in air under ambient conditions and the experimental X-ray powder-diffraction patterns agreed satisfactorily with patterns simulated based on single-crystal data, indicating the phase purity of the products as synthesized (Figure 4.1).



(a) $\text{Sn}_2\text{Pb}_5\text{Bi}_4\text{Se}_{13}$



(b) $\text{Sn}_{8.65}\text{Pb}_{0.35}\text{Bi}_4\text{Se}_{15}$

Figure 4.1 Experimental and simulated X-ray powder patterns for a) $\text{Sn}_2\text{Pb}_5\text{Bi}_4\text{Se}_{13}$ and b) $\text{Sn}_{8.65}\text{Pb}_{0.35}\text{Bi}_4\text{Se}_{15}$.

4.1.2. Single-crystal X-ray diffraction (XRD)

Single crystals of compounds $\text{Sn}_2\text{Pb}_5\text{Bi}_4\text{Se}_{13}$ ($0.08 \times 0.03 \times 0.03 \text{ mm}^3$) and $\text{Sn}_{8.65}\text{Pb}_{0.35}\text{Bi}_4\text{Se}_{15}$ ($0.08 \times 0.031 \times 0.03 \text{ mm}^3$) were mounted on glass fibers with epoxy glue; intensity data were collected on a diffractometer (Bruker APEX CCD) with graphite-monochromated Mo–K radiation ($\lambda = 0.71073 \text{ \AA}$) at 298(2) K. The distance from the crystal to the detector was 5.038 cm. Data were collected with a scan 0.3° in groups of 600 frames each at θ settings 0° , 90° , 180° and 270° . The duration of exposure was 30 s for both samples; values of 2θ varied between 2.25° and 28.35° . Diffraction signals obtained from all frames of reciprocal space images were used to determine the parameters of the unit cell. The data were integrated (Siemens SAINT program) and corrected for Lorentz and polarization effects⁶⁵. Absorption corrections were based on a function fitted to the empirical transmission surface as sampled by multiple equivalent measurements of numerous reflections. The structural model was obtained with direct methods and refined with full-matrix least-square refinement based on F^2 (SHELXTL package⁶⁶). The atomic occupancy for each metal site was determined from the coordination environment compared with literature and a formula valence balance.

(a) $\text{Sn}_2\text{Pb}_5\text{Bi}_4\text{Se}_{13}$

Several crystals from the crushed product were used for single-crystal X-ray diffraction, but the initial diffraction data to index these crystals indicated that many of them were twinned crystals with large standard deviations of the lattice parameters. The best crystal data for the structure determination were selected for a rod-shaped crystal that revealed a monoclinic unit cell ($a = 14.001(6) \text{ \AA}$, $b = 4.234(2) \text{ \AA}$ and $c = 23.471(8) \text{ \AA}$, $V = 1376.2(1) \text{ \AA}^3$); systematic absences indicated space group $C2/m$ (No. 12). Thirteen independent crystallographic sites (M1-6 and Se7-13) were located. The structural refinements displayed

unreasonable thermal displacement parameters for sites M1-6, indicative of positions with mixed occupancy of Bi/Sn or Pb/Sn. The basis of charge balance was used to determine the site preference for Pb or Bi; sites (M1-M3), (M4-M6) and Se7-Se13 were assigned as mixed occupancy of Bi/Sn, Pb/Sn, and 100 % Se, respectively. During the latter stages of refinement, four large residues ($\sim 4\text{-}6 \text{ e}/\text{\AA}^3$) appeared in the map of electron density at positions near M3 and M6 sites, which might be due to the contribution of twin components. These maxima were made to refine as partially occupied Sn, Pb or Bi atoms, but refined formula were not charge-balanced to justify the refinement. These maxima were therefore excluded as atoms in the final model because of their uncertainty. Attempts to collect data from the twin component and refined in a HKL5 format failed to improve the refinement with decreased residuals. Assuming Sn^{2+} , Pb^{2+} , Bi^{3+} and Se^{2-} , a charge-balanced formula $(\text{Sn}^{2+})_{2.07}(\text{Pb}^{2+})_{5.06}(\text{Bi}^{3+})_{3.87}(\text{Se}^{2-})_{13}$ was constructed. The final cycle of refinement included anisotropic displacement parameters and a secondary extinction correction performed on F_0^2 with 82 parameters and 1877 independent reflections. Final structural refinements produced $R1/wR2/GOF = 0.058/0.147/1.023$.

(b) $\text{Sn}_{8.65}\text{Pb}_{0.35}\text{Bi}_4\text{Se}_{15}$

X-ray measurements on a single crystal revealed a monoclinic unit cell with $a = 13.872(3) \text{ \AA}$, $b = 4.2021(8) \text{ \AA}$, $c = 26.855(5) \text{ \AA}$, $V = 1557.1(5) \text{ \AA}^3$; systematic absences indicated space group $C2/m$ (No. 12). Fifteen crystallographic sites (M1-2, Sn3, M4-M7, and Se8-Se15) were found. The cationic sites M1-2, M4-M7 have mixed occupancy by Bi/Sn and Pb/Sn atoms because of their atypical parameters for thermal displacement when refined with full occupancy by Sn, Pb or Bi. The refined electron density of site Sn3 is near 100 % Sn within a standard deviation, and was so assigned. During the latter stages of refinement, a large maximum ($\sim 8 \text{ e}/\text{\AA}^3$) appeared in the map of electron density at a position near M7 (~ 0.8

Å), which might be due to the contribution of twin components. This feature was made to refine as partially occupied Sn, Pb or Bi atoms, but the refined formulae were not charge-balanced, so this feature was excluded as an atom in the final model. Attempts to collect data from the twin component and refined in HKL5 format failed to improve the refinement with decreased residuals. Assuming $\text{Sn}^{2+}/\text{Pb}^{2+}$, $\text{Sn}^{2+}/\text{Bi}^{3+}$ and Se^{2-} , a charge-balanced formula $(\text{Sn}^{2+}_{8.41}\text{Pb}^{2+}_{0.37})(\text{Bi}^{3+})_{4.22}(\text{Se}^{2-})_{15}$ was constructed that served to constrain the occupancies of the disordered sites. The final cycle of refinement included anisotropic displacement parameters and a secondary extinction correction performed on F_0^2 with 95 parameters and 2200 independent reflections. Final structural refinements produced $\text{Sn}_{8.65}\text{Pb}_{0.35}\text{Bi}_4\text{Se}_{15}$ with $R1/wR2/GOF = 0.0506/0.1227/1.425$. Crystallographic data and selected bond distances for $\text{Sn}_2\text{Pb}_5\text{Bi}_4\text{Se}_{13}$ and $\text{Sn}_{8.65}\text{Pb}_{0.35}\text{Bi}_4\text{Se}_{15}$ are given in Tables 4.1-4.5.

Table 4.1 Crystallographic Data for $\text{Sn}_2\text{Pb}_5\text{Bi}_4\text{Se}_{13}$ and $\text{Sn}_{8.65}\text{Pb}_{0.35}\text{Bi}_4\text{Se}_{15}$

Empirical formula	$\text{Sn}_2\text{Pb}_5\text{Bi}_4\text{Se}_{13}$	$\text{Sn}_{8.65}\text{Pb}_{0.35}\text{Bi}_4\text{Se}_{15}$
Crystal size / mm ³	0.08×0.03×0.03	0.08×0.031×0.3
Formula mass / g mol ⁻¹	3129.3	3141.14
Temperature / K	298(2)	298(2)
Wavelength / Å	0.71073	0.71073
Crystal system	<i>monoclinic</i>	<i>monoclinic</i>
Space group	C2/m (No. 12)	C2/m (No. 12)
<i>a</i> / Å	14.001(6)	13.872(3)
<i>b</i> / Å	4.234(2)	4.2021(8)
<i>c</i> / Å	23.471(8)	26.855(5)
<i>V</i> , Å ³	98.46(1)	95.92(3)
<i>Z</i>	1376.2(1)	1557.1(5)
Density / g cm ⁻³	2	2
Absorption coeff. / mm ⁻¹	7.552	6.7
Independent reflections	74.5	49.88
<i>GOF</i> on F^2	1877 [R(int) = 0.0499]	2200[R(int)=0.0328]
<i>R1/wR2</i> [$I > 2\sigma(I)$]	1.022	1.425
	5.84/14.77 %	5.06/12.27 %

$$^a R1 = \frac{\sum ||F_0| - |F_c||}{\sum |F_0|} \quad wR2 = \left\{ \frac{\sum [w(F_0^2 - F_c^2)^2]}{\sum [w(F_0^2)^2]} \right\}^{1/2}$$

Table 4.2 Fractional Atomic Coordinates and Equivalent Isotropic Atomic DisplacementParameters ($U_{eq} / 10^{-3} \text{ \AA}^2$) and Site Occupancies for $\text{Sn}_2\text{Pb}_5\text{Bi}_4\text{Se}_{13}$

	Wyckoff site	x	y	z	sof	U_{eq}^a
M1	2d	0.5	0	0.5	Sn/Bi 0.64(1)/0.36	13(1)
M2	4i	0.7494(1)	0	0.4147(1)	Sn/Bi 0.09/0.91(2)	19(1)
M3	4i	0.1490(1)	0.5	0.0443(1)	Sn/Bi 0.16/0.84(2)	17(1)
M4	4i	0.4438(1)	0.5	0.1224(1)	Sn/Pb 0.23/0.77(1)	18(1)
M5	4i	0.5077(1)	0.5	0.3388(1)	Sn/Pb 0.22/0.78(2)	19(1)
M6	4i	0.2395(1)	0	0.2252(1)	Sn/Pb 0.05/0.95(2)	48(1)
Se7	4i	0.6284(2)	0.5	0.4600(1)	1	14(1)
Se8	4i	0.2875(2)	0	0.879(1)	1	20(1)
Se9	4i	0.3711(2)	0	0.3763(1)	1	29(1)
Se10	4i	0.3837(2)	0.5	0.2311(1)	1	19(1)
Se11	2a	0	0	0	1	14(1)
Se12	4i	0.0855(2)	0.5	0.1524(1)	1	16(1)
Se13	4i	0.6340(2)	0	0.3063(1)	1	18(1)

^a (U_{eq}) is defined as one third of the trace of the orthogonalized U_{ij} tensor**Table 4.3** Fractional Atomic Coordinates and Equivalent Isotropic Atomic DisplacementParameter ($U_{eq} / 10^{-3} \text{ \AA}^2$), and Site Occupancies for $\text{Sn}_{8.65}\text{Pb}_{0.35}\text{Bi}_4\text{Se}_{15}$

	Wyckoff site	x	y	z	sof	U_{eq}^a
M1	4i	0.5740(1)	0	0.1424(1)	Sn/Bi 0.29/0.71(1)	22(1)
M2	2a	0.5	0.5	0	Sn/Bi 0.63(1)/0.37	24(1)
Sn3	4i	0.7835(1)	0.5	0.690(1)	1	20(1)
M4	4i	0.6302(1)	0	0.4607(1)	Sn/Bi 0.52(1)/0.48	22(1)
M5	4i	0.3665(1)	0.5	0.2082(1)	Sn/Bi 0.72(1)/0.28	23(1)
M6	4i	0.3934(1)	0.5	0.3943(1)	Sn/Bi 0.55(1)/0.45	24(1)
M7	4i	0.1493(1)	0	0.3084(1)	Sn/Pb 0.82(1)/0.18	70(1)
Se8	2c	0.5	0.5	0.5	1	19(1)
Se9	4i	0.7127(1)	0.5	0.1739(1)	1	29(1)
Se10	4i	0.2867(1)	0.5	0.2999(1)	1	23(1)
Se11	4i	0.5036(1)	0	0.2360(1)	1	20(1)
Se12	4i	0.5223(1)	0	0.3684(1)	1	20(1)
Se13	4i	0.7491(1)	0.5	0.4220(1)	1	26(1)
Se14	4i	0.4296(1)	0.5	0.1012(1)	1	17(1)
Se15	4i	0.6437(1)	0	0.328(1)	1	18(1)

^a U_{eq} is defined as one third of the trace of the orthogonalized U_{ij} tensor.

Table 4.4 Interatomic Distances for Sn₂Pb₅Bi₄Se₁₃.

	Contacts	Distance/Å		Contacts	Distance/Å		Contacts	Distance/Å
M1	—Se7× 4	3.014(2)	M2	—Se13	2.806(3)	M3	—Se12	2.808(3)
	—Se9× 2	3.184(1)		—Se9× 2	2.941(2)		—Se8× 2	2.950(2)
				—Se7× 2	3.001(2)		—Se11× 2	3.0451(1)
				—Se7	3.176(3)		—Se8	3.351(2)
M4	—Se10	2.802(3)	M5	—Se10	2.848(3)	M6	—Se10× 2	2.913(2)
	—Se12× 2	2.916(2)		—Se13× 2	2.929(2)		—Se12× 2	3.311(1)
	—Se8× 2	3.066(2)	—Se9× 2	3.068(2)	—Se13× 2	3.335(1)		
	—Se11	3.088(2)	—Se7	3.087(3)	—Se8	3.386(2)		

Table 4.5 Selected Distances in Å for Sn_{8.65}Pb_{0.35}Bi₄Se₁₅

	Contacts	Distance/Å		Contacts	Distance/Å		Contacts	Distance/Å
M1	—Se11	2.789(2)	M2	—Se15× 4	2.967(1)	Sn3	—Se15× 2	2.954(1)
	—Se9× 2	2.915(1)		—Se14× 2	2.981(2)		—Se14× 2	2.984(1)
	—Se14× 2	3.031(1)			—Se15		3.011(2)	
	—Se15	3.190(1)			—Se9		3.075(1)	
M4	—Se12	2.761(2)	M5	—Se10	2.801(2)	M6	—Se10	2.800(2)
	—Se13× 2	2.926(1)		—Se11× 2	2.880(1)		—Se12× 2	2.890(1)
	—Se8× 2	3.0309(8)		—Se9× 2	3.068(1)		—Se13× 2	3.046(1)
	—Se13× 2	3.412(2)		—Se7	3.087(1)		—Se8	3.062(1)
M7	—Se10× 2	2.862(2)						
	—Se13	3.209(2)						
	—Se12× 2	3.266(1)						
	—Se11× 2	3.391(2)						

4.1.3 Characterization

X-ray powder-diffraction patterns were measured on a powder diffractometer of Bragg–Brentano-type (Bruker D8 Advance, operated at 40 kV and 40 mA, Cu K α , $\lambda = 1.5418$ Å). For phase identification, XRD data were collected in a 2θ range from 5° to 90° with a step interval 0.02° . Energy-dispersive spectra (SEM/EDX, Hitachi S-4700I High-Resolution Scanning Electron Microscope) were recorded on the cuboid-like crystalline samples. A semiquantitative EDS analysis on individual crystals of each reaction product confirmed the presence of Sn, Pb, Bi and Se. Measurements of differential scanning calorimetry (DSC) and

thermogravimetry (TG) were performed with a thermal analyzer (NETZSCH STA 409PC). A powder sample (approximately 40 mg) was placed in an alumina crucible; Al₂O₃ powder served as a reference sample. The sample was heated to 1273 K at 20 K/min under a constant flow of N₂.

4.1.4 Calculation of the Electronic Structure

Band calculations with tight-binding linear muffin-tin orbitals (LMTO) using the atomic spheres approximation (ASA) were undertaken to understand the electronic structures⁶⁸⁻⁷². Density-functional theory was employed with the local-density approximation (LDA) for the exchange-correlation energy. Space group *C2/m* was used to simulate the observed crystal structures containing mixed-occupancy sites, and the phase width. Integration in *k* space was performed with an improved tetrahedron method on grids 16×16×8 of unique *k* points in the first Brillouin zone. We analyzed the electronic structure by extracting information from the band structure, density of states (DOS), and curves of crystal-orbital Hamiltonian populations (COHP)⁷³.

4.1.5 Physical Property Measurements

We measured Seebeck coefficients on a cold-pressed bar (1×1×5 mm³) with a commercial thermopower measurement apparatus (MMR Technologies) in the temperature range 300 – 600 K under a dynamic vacuum (~10⁻² Torr). Constantan served as an internal standard, and silver conductive paint was used to create electric contacts. Measurements of DC conductivity were performed with a standard four-probe method with a homemade device under vacuum (~10⁻² Torr) in the temperature range 30 – 300 K.

Electrical contacts consisted of four copper wires attached to the bulk with silver glue.

Samples were placed under vacuum for at least 1 h to allow the silver glue to dry completely,

which improved contact performance.

4.2 Results and discussion

4.2.1 Structure description

(a) $\text{Sn}_2\text{Pb}_5\text{Bi}_4\text{Se}_{13}$

$\text{Sn}_2\text{Pb}_5\text{Bi}_4\text{Se}_{13}$ is isostructural with $\text{KSn}_5\text{Bi}_4\text{Se}_{13}$ ³⁶ that crystallizes in monoclinic space group $C2/m$ (No. 12) with four formula units per unit cell. The structure contains thirteen crystallographically inequivalent sites – three for mixed-occupancy cations $\text{Sn}^{2+}/\text{Bi}^{3+}$, three for mixed-occupancy cations $\text{Sn}^{2+}/\text{Pb}^{2+}$, and seven for anions (Se^{2-}). Figure 4.2a shows the structure of $\text{Sn}_2\text{Pb}_5\text{Bi}_4\text{Se}_{13}$ in a projection along the crystallographic b -axis [010]. The coordination environment of metal sites is grouped into four types: (i) Site M1 is hexacoordinate in a distorted octahedron with average M-Se distance 3.071 Å. (ii) Sites M2 five near Se (~ 2.938 Å) atoms and one remote Se (~ 3.176 Å) atoms. (iii) The coordination and M3 are surrounded by six selenium atoms forming a capped square pyramid containing

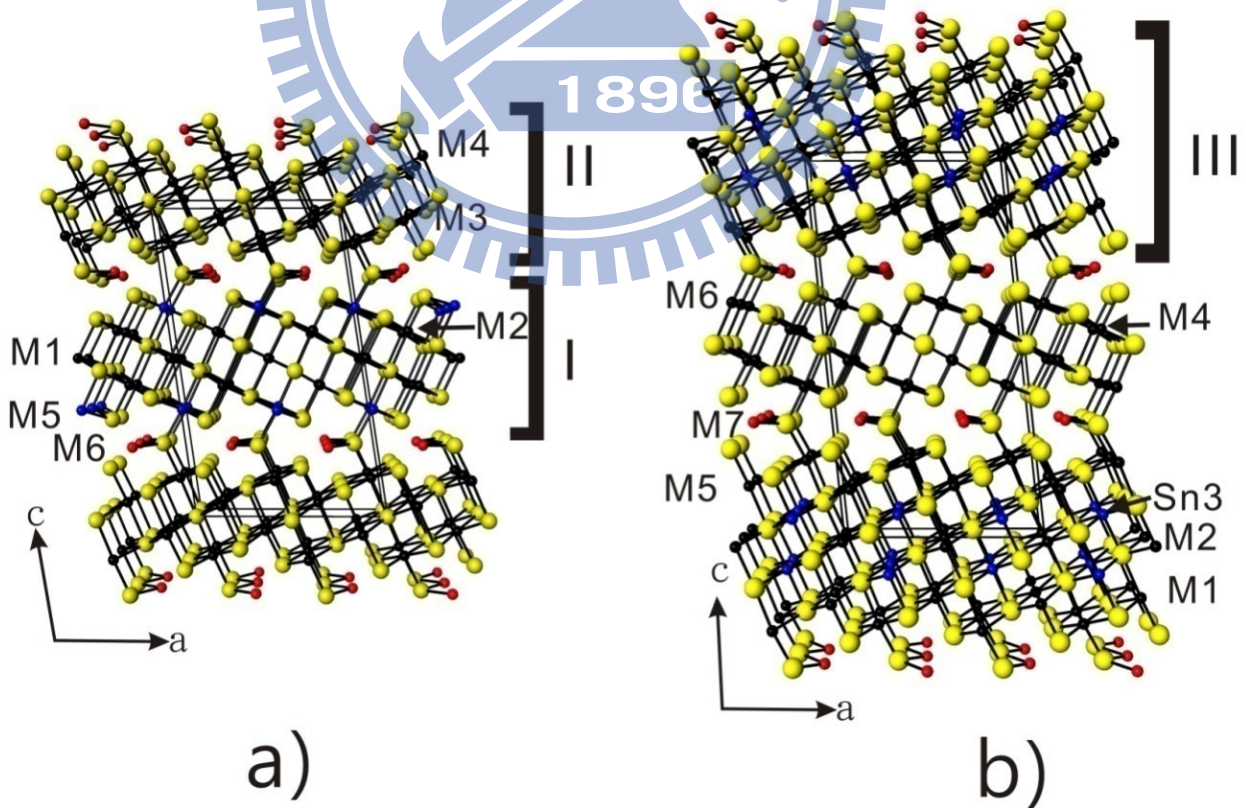


Figure 4.2 Crystal structures of $\text{Sn}_2\text{Pb}_5\text{Bi}_4\text{Se}_{13}$ (a) and $\text{Sn}_{8.65}\text{Pb}_{0.35}\text{Bi}_4\text{Se}_{15}$ (b) in a projection

along the crystallographic *b*-axis [010], showing slabs **I**, **II** and **III** of NaCl (113) tilt planes. environments around sites M4 and M5 are distorted octahedra with three short M-Se bonds (2.8 – 3.0 Å) opposite three long ones (3.0 - 3.1 Å) attributed to the ns^2 lone-pair effect, as observed in similar Pb-Se contacts for known chalcogenides with Pb as the constituent element, such as $Pb_4Sb_4Se_{10}$ ⁷⁴. (iv) Site M6 lies on the tropychemical cell-twinning plane that has a bicapped trigonal-prism coordination with a short M-Se contact to Se10 (2.913(7) Å); the other distances to Se12 (3.311(2) Å), Se13 (3.335(4) Å), Se8 (3.386(4) Å) and Se9 (3.749(5) Å) are longer.

The structure consists of two slabs with disparate thicknesses (**I** and **II**) parallel to plane (113) of the NaCl-type structure. Slab **I** comprises Pb- and Bi-rich sites of sites M3 and M4, whereas slab **II** comprises sites M1, M2 and M5 rich in Pb or Sn. The slabs as described array with *c* axial expanding to form a herringbone arrangement, which is stitched with M6 and Se10. Relative to $KSn_5Bi_5Se_{13}$, all M-Se coordination environments are similar, and interatomic distances are slightly increased because of large and heavy Pb atoms in the structure of $Sn_2Pb_5Bi_4Se_{13}$. The atomic composition of site M6 lies on the cell-twinning plane for $Sn_2Pb_5Bi_4Se_{13}$ (M6 = 95 % Pb + 5 % Sn), different from the corresponding site in $KSn_5Bi_5Se_{13}$ (M5 = 50 % K + 50 % Bi)

(b) $Sn_{8.65}Pb_{0.35}Bi_4Se_{15}$

$Sn_{8.65}Pb_{0.35}Bi_4Se_{15}$ is isostructural with the mineral vikingite, $Ag_4Pb_{10}Bi_{12}S_{30}$ ⁹³, that crystallizes in monoclinic space group $C2/m$ (No. 12) with four formula units per unit cell. The structure contains fifteen crystallographically inequivalent sites, six for mixed-occupancy cations (Sn^{2+}/Bi^{3+} or Sn^{2+}/Pb^{2+}), one for Sn^{2+} and eight for anions (Se^{2-}). The coordination environments of cations are similar to the structure of $Sn_2Pb_5Bi_4Se_{13}$ that contains hexacoordinate sites of three types (i= M2, M3; ii=M1, M4; iii= M5, M6) and one bi-capped

trigonal-prism site (iv = M7). The projection of $\text{Sn}_{8.65}\text{Pb}_{0.35}\text{Bi}_4\text{Se}_{15}$ along the crystallographic *b*-axis [010] is shown in Figure 4.2b that contains slabs **I** and **III** parallel to plane (113) of the NaCl-type structure. The building unit of the thin layer (slab **I**) is similar to the building unit in $\text{Sn}_2\text{Pb}_5\text{Bi}_4\text{Se}_{13}$ that contains metal sites of M4, M6 and three sites for Se atoms. M4 and Se atoms are connected to form a distorted 5+1-coordination octahedral geometry with five small (~ 2.935 Å) and one large (~ 2.935 Å) interatomic distances. Slab **III** contains metal sites of M1, M2, Sn3, M5, and five sites for Se atoms. Site M1 shows a distorted octahedral environment with 5+1 coordination by six selenium atoms with average interatomic distance 2.979 Å. The coordinations of sites M2 and Sn3 are near ideal octahedral coordination with average interatomic distances 2.972 and 2.994 Å for M2-Se and Sn3-Se contacts, respectively. Sites M5 and M6 are describable as distorted octahedral, containing three near Se (~ 2.855 Å) atoms and three far Se (~ 3.06 Å) atoms. The coordination environment of M7 is similar to site M6 of $\text{Sn}_2\text{Pb}_5\text{Bi}_4\text{Se}_{13}$ that forms a bicapped trigonal prism with eight Se atoms in the mirror plane of the trochochemical cell twinning to accommodate Sn and Pb in a ratio 0.82/0.18. The bond lengths exhibit a strong interaction to Se10 (2.862(2) Å), and the others have a more remote distance to Se12 (3.311(2) Å), Se13 (3.335(4) Å) and Se8 (3.386(4) Å).

The M-Se distances in both structures are comparable to a binary system and some multinary selenide compounds in the literature that contain mixed occupancy of Bi/Sn or Pb/Sn such as $\text{Pb}_4\text{Sb}_4\text{Se}_{10}$ ⁷⁴, $\text{Pb}_{0.875}\text{Sn}_{0.125}\text{Se}$ ⁷⁵, $\text{Pb}_{0.84}\text{Sn}_{1.16}\text{S}_{1.86}\text{Se}_{0.14}$ ⁹⁴, $\text{K}_{0.54}\text{Sn}_{4.92}\text{Bi}_{2.54}\text{Se}_9$ ³⁶, $\text{KSn}_5\text{Bi}_5\text{Se}_{13}$ ³⁶ and $\text{K}_{0.54}\text{Sn}_{3.54}\text{Bi}_{11.46}\text{Se}_{21}$ ⁹⁵. The structures of $\text{Sn}_2\text{Pb}_5\text{Bi}_4\text{Se}_{13}$ and $\text{Sn}_{8.65}\text{Pb}_{0.35}\text{Bi}_4\text{Se}_{15}$ belong to the lillianite homologous series that are described with a symbol $L(n, n')$ for their size of slab length; L signifies that the structure is the lillianite homologous series and (n, n') indicates the number of octahedra between two sides of the trochochemical cell-twinning plane.

$\text{Sn}_2\text{Pb}_5\text{Bi}_4\text{Se}_{13}$ can thus be defined as $L(4, 5)$ and $\text{Sn}_{8.65}\text{Pb}_{0.35}\text{Bi}_4\text{Se}_{15}$ as $L(4, 7)$ of the lillianite homologous series.

4.2.2 Electronic Structure

(a) $\text{Sn}_2\text{Pb}_5\text{Bi}_4\text{Se}_{13}$

To calculate the electronic structure using the TB-LMTO-ASA method, a charge-balanced model of $\text{SnPb}_6\text{Bi}_4\text{Se}_{13}$ was constructed with the cation sites assigned to Sn(M1), Bi(M2, M3) and Pb(M4, M5, M6). Projections of the corresponding total and partial density of states (DOS, PDOS) for atoms in slabs **I** and **II** are presented in Figure 4.3. The band structure of $\text{SnPb}_6\text{Bi}_4\text{Se}_{13}$ shows a direct band gap with a calculated gap ~ 0.2 eV, indicative of a semiconducting property. As the DOS curve shows, the contributions of metal atoms above the Fermi energy stem largely from atoms of slab **I**, whereas the large maximum below the Fermi level arises predominantly from atoms in slab **II**. The large feature between -6 eV and the Fermi level is dominated by selenium-based filled p orbitals, whereas the bottom of the conduction band is based mainly on empty p orbitals of the main-group metal.

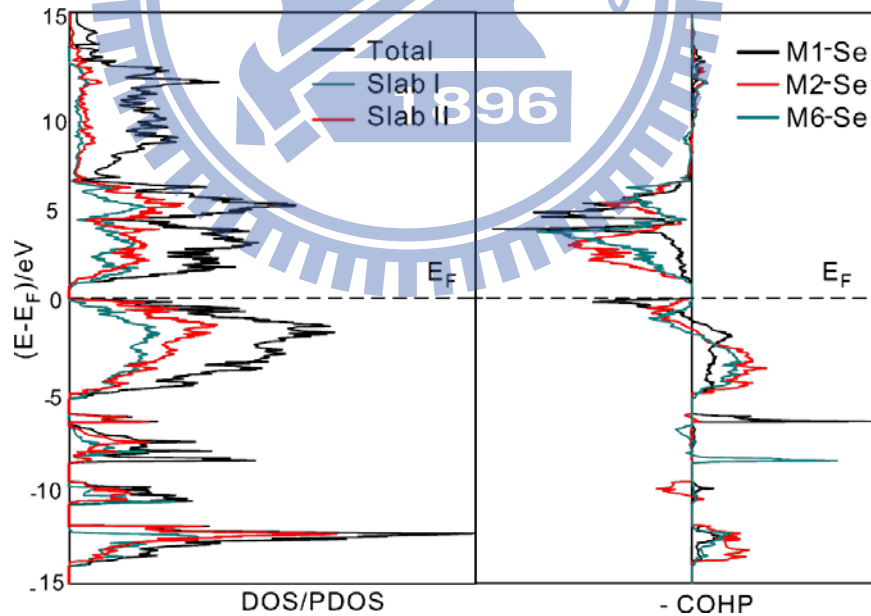


Figure 4.3 Density of states (left), partial density of states, and crystal-orbital hamiltonian populations (COHP) for selected M-Se (M1-Se : black line, M2-Se : red dashed line, and M6-Se : blue line) interactions (right) curves of $\text{Sn}_2\text{Pb}_5\text{Bi}_4\text{Se}_{13}$. The horizontal dashed line denotes the Fermi energy (E_F). The contributions from slab **I** (M3 (Bi) + M4 (Pb)) and slab **II** (M1 (Bi) + M2 (Bi) + M5 (Pb)) are denoted with red and blue lines.

The DOS and the crystal-orbital Hamiltonian populations (COHP) near the Fermi level are dominated by the p states of Se and metals (Sn/Pb/Bi). The ns states of Sn, Pb and Bi atoms are essentially localized and shown in sharp peaks centered at ca. -6, -10 and -8 eV, respectively, which might result from the inert-pair effect commonly observed in heavy main-group elements. Calculations of the crystal-orbital Hamiltonian population (COHP) are shown in Figure 2.3; the results indicate that bonding states of the (Sn, Pb, Bi)-Se contacts are occupied and well below the Fermi level, with small contributions of antibonding interactions near the Fermi level. Despite the antibonding interactions near the Fermi level, the bonding character remains, with average ICOHP values 0.62, 0.58 and 0.94 eV/bond for Sn-Se, Pb-Se and Bi-Se contacts, respectively.

(b) $Sn_{8.65}Pb_{0.35}Bi_4Se_{15}$

To understand the effect of Pb to the stability of the $Sn_{8.65}Pb_{0.35}Bi_4Se_{15}$ phase, four hypothetical models $Sn_{9-x}Pb_xBi_4Se_{15}$ ($x = 0, 2, 4, 9$) were constructed to perform calculations of the electronic structures. Details of the models are described in the Table 4.6. In general, the DOS curves for all models exhibit filled valence band with narrow band gaps ($\Delta E < 0.01$ eV), indicative of a semiconducting property.

Table 4.6 Four models with varied assignment of metal sites for the LMTO calculations.

	$Sn_9Bi_4Se_{15}$	$Sn_7Pb_2Bi_4Se_{15}$	$Sn_5Pb_4Bi_4Se_{15}$	$Pb_9Bi_4Se_{15}$
M1	Bi	Bi	Bi	Bi
M2	Sn	Sn	Sn	Pb
M3	Sn	Sn	Sn	Pb
M4	Bi	Bi	Bi	Bi
M5	Sn	Sn	Pb	Pb
M6	Sn	Sn	Sn	Pb
M7	Sn	Pb	Pb	Pb

Further examination of the PDOS curves show that the Sn contributions decrease as sites M1-M7 are gradually replaced by Pb (Figure 4.4). The results of DOS and COHP curves from $\text{Sn}_7\text{Pb}_2\text{Bi}_4\text{Se}_{15}$ (Sn = M2, M3, M5, M6; Bi = M1, M4; Pb = M7) are illustrated in Figure 4.5. Projections of the partial density of states (PDOS) for atoms in slab **I** and **III** show that the large feature between -6 eV and the Fermi level is dominated by the p orbital from atoms of slab **III**, whereas the contributions to the PDOS above the Fermi level are p orbitals from atoms of slab **I**. The COHP calculations for M-Se contacts show nearly optimal bonding with weak antibonding characters near the Fermi level.

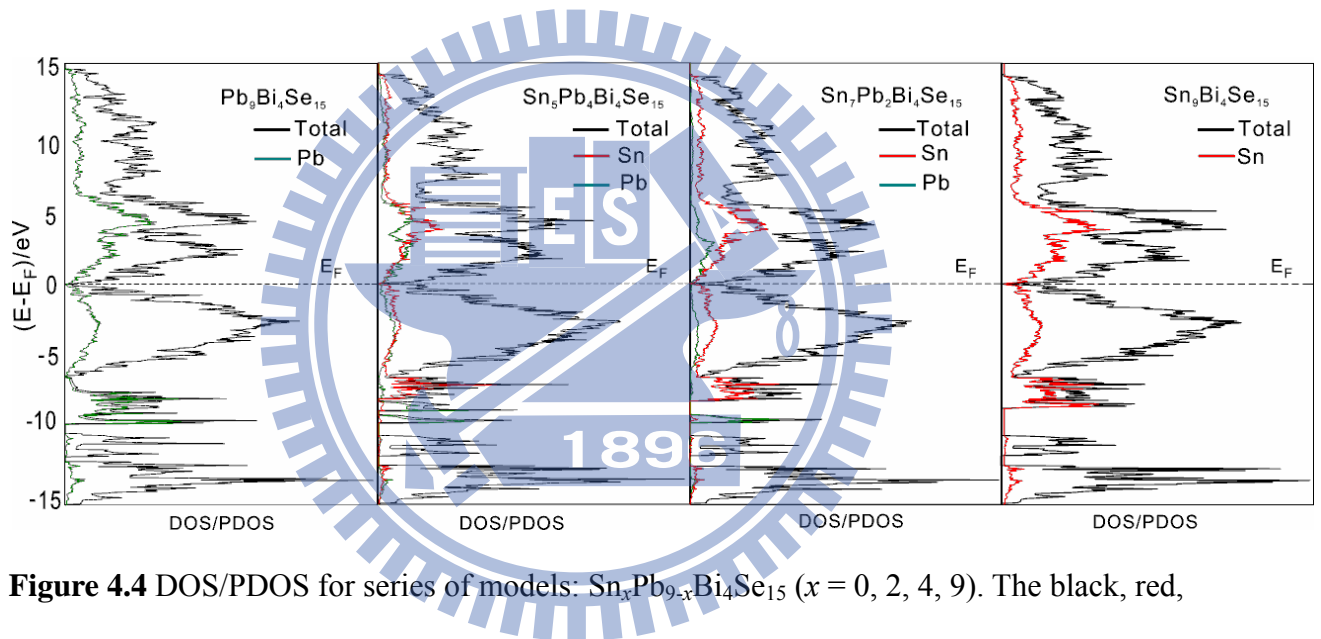


Figure 4.4 DOS/PDOS for series of models: $\text{Sn}_x\text{Pb}_{9-x}\text{Bi}_4\text{Se}_{15}$ ($x = 0, 2, 4, 9$). The black, red, and green lines refer to total, Sn and Pb atoms, respectively.

The effect of substituting Sn with Pb atoms to the bonding character of M7-Se contact was studied. Figure 2.6 shows the PDOS and COHP curves from $\text{Sn}_9\text{Bi}_4\text{Se}_{15}$ (M7 = Sn) and $\text{Sn}_7\text{Pb}_2\text{Bi}_4\text{Se}_{15}$ (M7 = Pb). PDOS curve of M7 site for $\text{Sn}_9\text{Bi}_4\text{Se}_{15}$ exhibits sharp contributions of Sn(5s) states between -7.5 and -8.5 eV, which are significantly reduced by ~1 eV for M7 site in $\text{Sn}_7\text{Pb}_2\text{Bi}_4\text{Se}_{15}$. The COHP curves show bonding interaction for these states. Since the space for Sn^{2+} and Pb^{2+} within the coordination polyhedra is the same and the ionic radius for

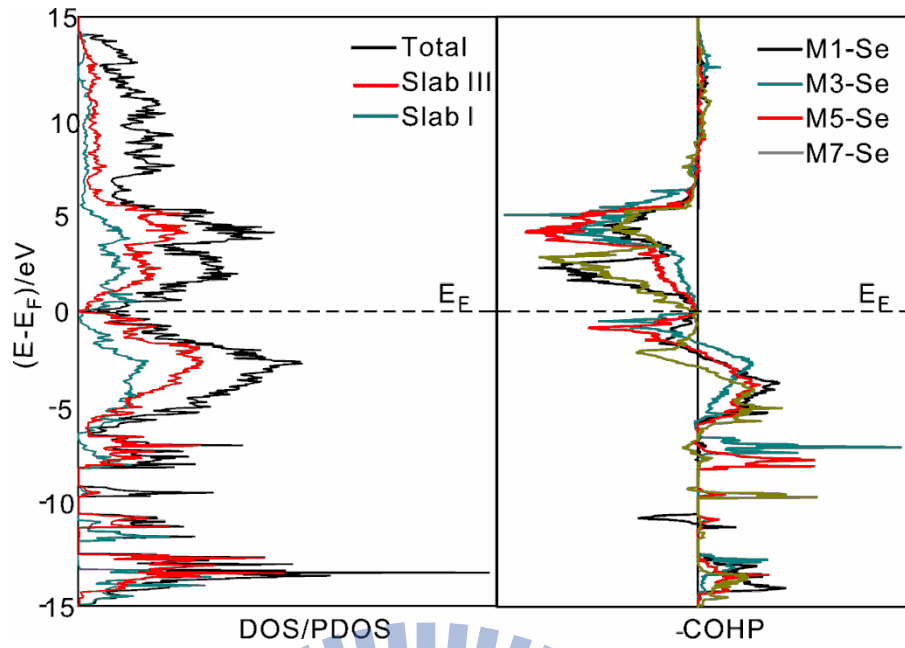


Figure 4.5. Density of states (left), partial density of states, and crystal-orbital hamiltonian populations (COHP) for selected M-Se (M1-Se : black line, M3-Se : blue line, M5-Se : red line and M7-Se : green line) interactions (right) curves of $\text{Sn}_7\text{Pb}_2\text{Bi}_4\text{Se}_{15}$. The horizontal dashed line denotes the Fermi energy (E_F).

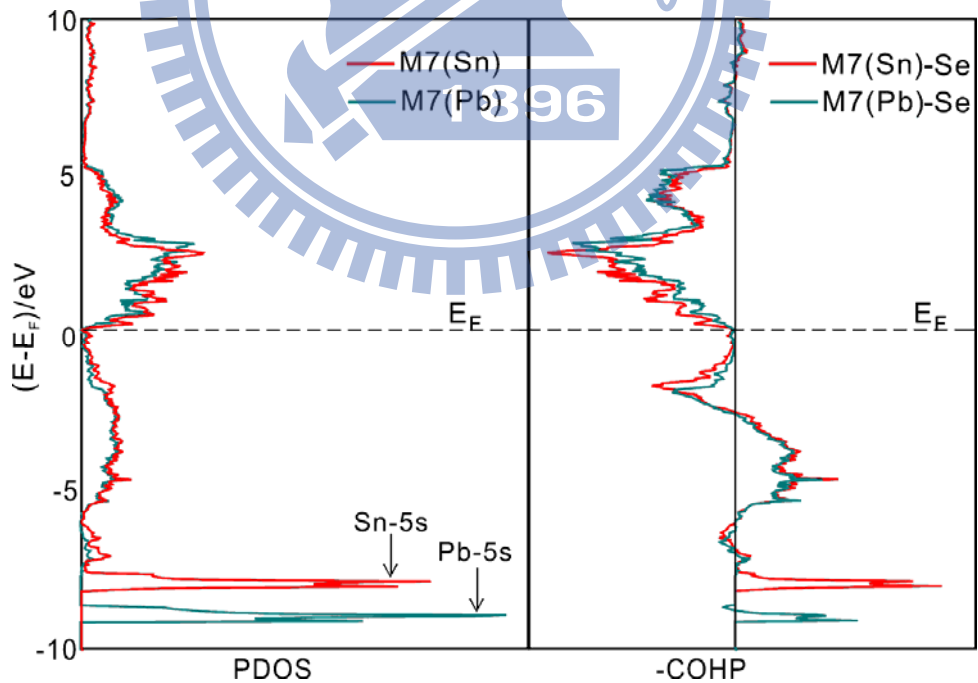


Figure 4.6 PDOS and COHP plots for $\text{Sn}_9\text{Bi}_4\text{Se}_{15}$ (red) and $\text{Sn}_7\text{Pb}_2\text{Bi}_4\text{Se}_{15}$ (blue). a) PDOS for M7 (M = Sn, Pb). b) COHP for M7-Se contact. The horizontal dashed line denotes the Fermi energy (E_F).

Pb^{2+} (1.29 Å) is larger than that for Sn^{2+} (1.22 Å)⁷⁸, the interaction is shifted to lower energy region due to strong Pb-Se interaction. The experiment shows that the as-synthesized $\text{Sn}_{8.65}\text{Pb}_{0.35}\text{Bi}_4\text{Se}_{15}$ contains a M7 site mixed occupied by Pb and Sn atoms. For reactions with $x > 0.5$ in $\text{Sn}_{9-x}\text{Pb}_x\text{Bi}_4\text{Se}_{15}$, stable binary or ternary phases (SnSe_2 , Bi_2Se_3 , PbSe , etc) start to form.

4.2.3. Physical Properties

With a standard four-probe technique, we measured the dependence of resistivity on temperature from 50 to 300 K. The results show that both $\text{Sn}_2\text{Pb}_5\text{Bi}_4\text{Se}_{13}$ and $\text{Sn}_{8.65}\text{Pb}_{0.35}\text{Bi}_4\text{Se}_{15}$ exhibit decreasing resistivity with increasing temperature, hence conforming to a trend typical of a semiconductor (Figure 4.7a). Figure 4.7b reveals the measurement of the Seebeck coefficient for compounds $\text{Sn}_2\text{Pb}_5\text{Bi}_4\text{Se}_{13}$ and $\text{Sn}_{8.65}\text{Pb}_{0.35}\text{Bi}_4\text{Se}_{15}$. Both compounds show a slight temperature dependence of the Seebeck coefficient. The thermopower of $\text{Sn}_2\text{Pb}_5\text{Bi}_4\text{Se}_{13}$ is negative and decreases linearly from $\sim -80 \mu\text{V/K}$ at 308 K to $-184 \mu\text{V/K}$ at 680 K, whereas the thermopower of $\text{Sn}_{8.65}\text{Pb}_{0.35}\text{Bi}_4\text{Se}_{15}$ shows a positive Seebeck coefficient $\sim 179 \mu\text{V/K}$ for the entire range of temperature. The results indicate *n*-type and *p*-type semiconducting behavior for $\text{Sn}_2\text{Pb}_5\text{Bi}_4\text{Se}_{13}$ and $\text{Sn}_{8.65}\text{Pb}_{0.35}\text{Bi}_4\text{Se}_{15}$, respectively.

4.2.4 Thermoanalysis

TG-DSC curves versus temperature for $\text{Sn}_2\text{Pb}_5\text{Bi}_4\text{Se}_{13}$ and $\text{Sn}_{8.65}\text{Pb}_{0.35}\text{Bi}_4\text{Se}_{15}$ are shown in Figure 4.8. The TG-DSC measurements show similar features with exothermic maxima and mass loss beginning at 1031 and 1027 K for $\text{Sn}_2\text{Pb}_5\text{Bi}_4\text{Se}_{13}$ and $\text{Sn}_{8.65}\text{Pb}_{0.35}\text{Bi}_4\text{Se}_{15}$, respectively, corresponding to the decomposition of those compounds. These results were reproduced on heating the powder as synthesized sealed in a quartz ampoule under vacuum and subsequently heated to 1173 K. The PXRD pattern of the residue is indexed as a combination of $\text{Sn}_{0.571}\text{Bi}_{0.286}\text{Se}$, PbSe , BiSe , Se and an amorphous phase in the residual products.

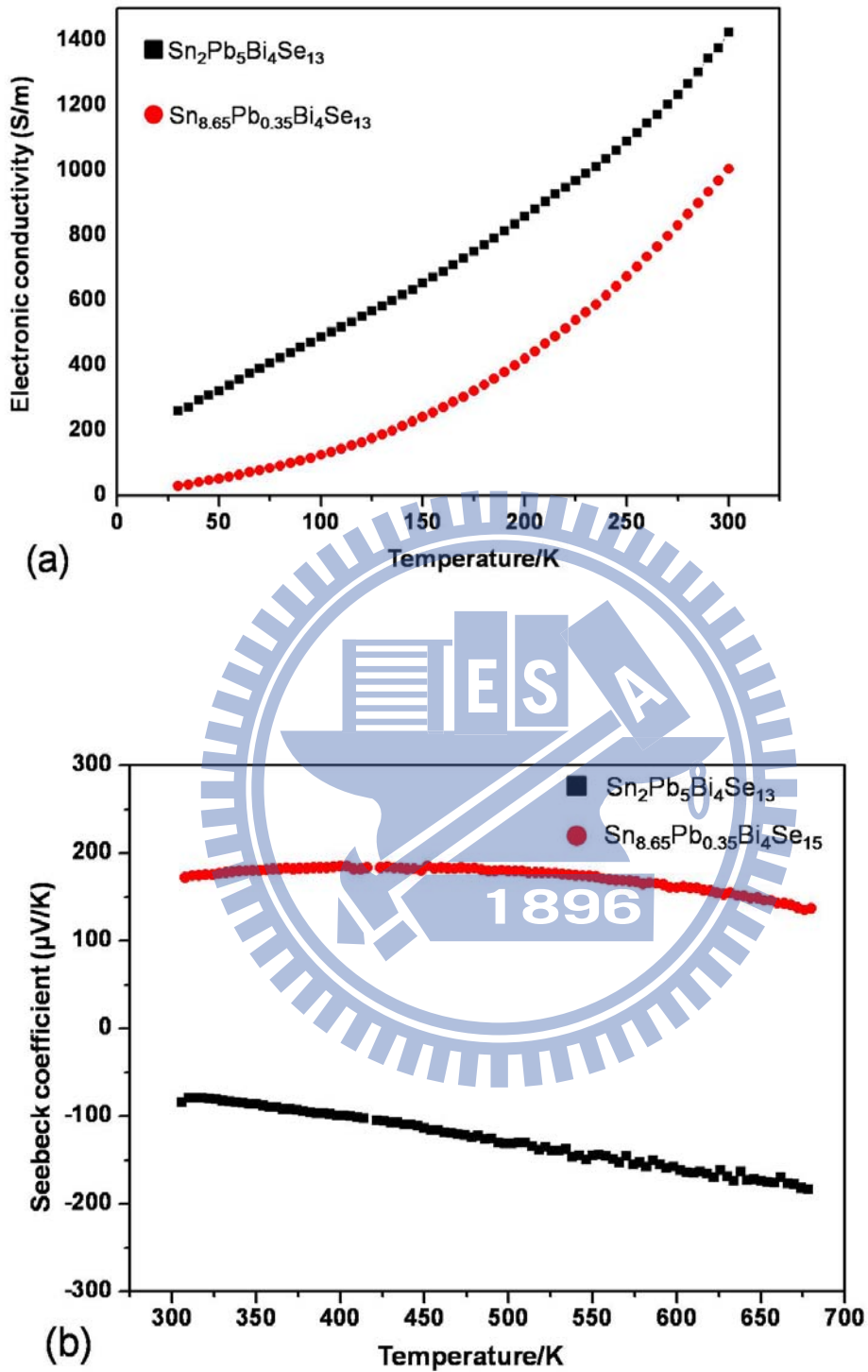


Figure 4.7 Temperature dependence of electrical conductivity (a) and thermoelectric power (b) of $\text{Sn}_2\text{Pb}_5\text{Bi}_4\text{Se}_{13}$ (black) and $\text{Sn}_{8.65}\text{Pb}_{0.35}\text{Bi}_4\text{Se}_{15}$ (red).

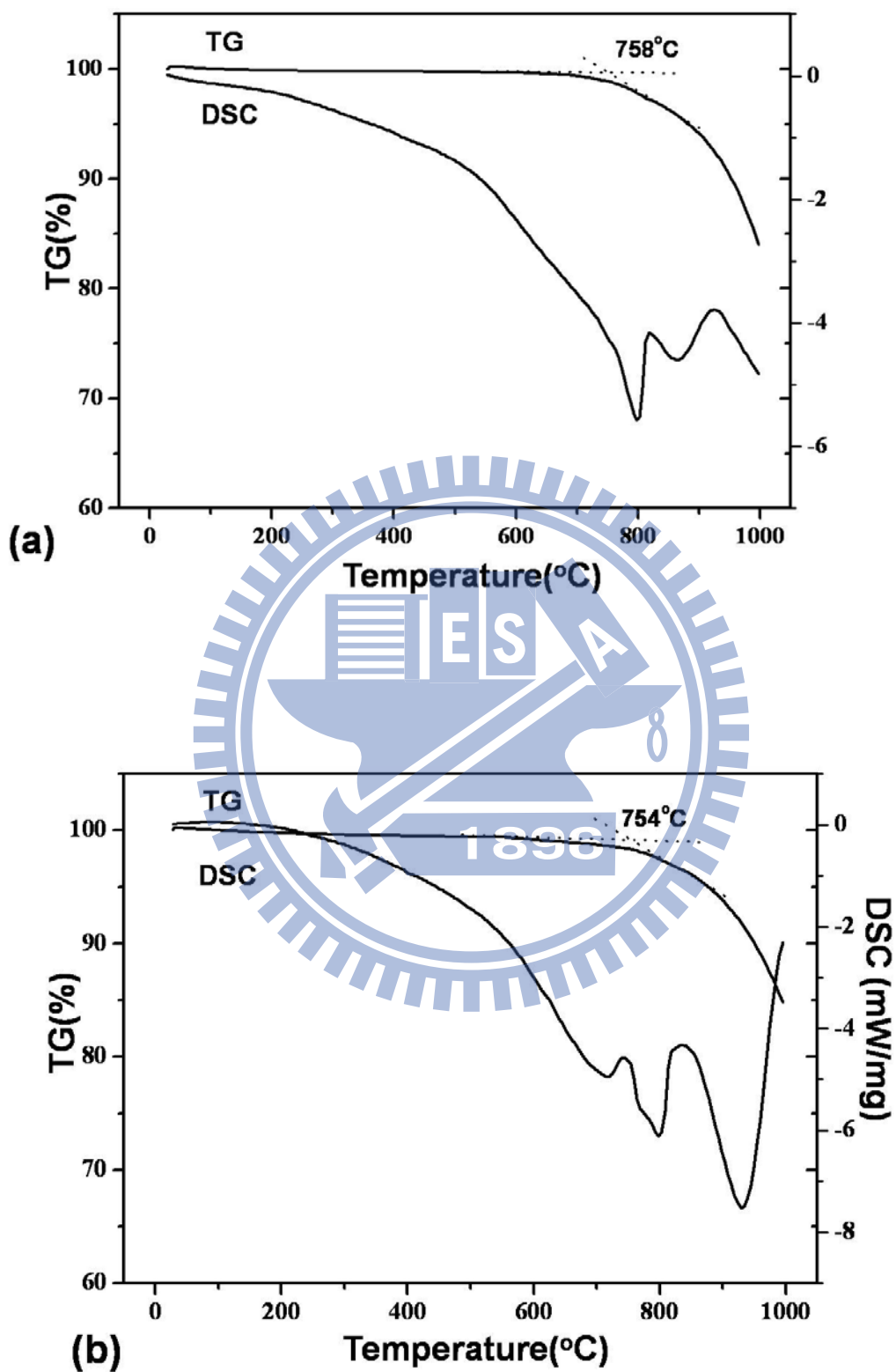


Figure 4.8 Thermal analysis (TG/DSC curves) of $\text{Sn}_2\text{Pb}_5\text{Bi}_4\text{Se}_{13}$ (a) and $\text{Sn}_{8.65}\text{Pb}_{0.35}\text{Bi}_4\text{Se}_{15}$

(b).

4.3 Conclusions

We prepared new quaternary chalcogenides $\text{Sn}_2\text{Pb}_5\text{Bi}_4\text{Se}_{13}$ and $\text{Sn}_{8.65}\text{Pb}_{0.35}\text{Bi}_4\text{Se}_{15}$ in the Sn-Pb-Bi-Se system. The structures of $\text{Sn}_2\text{Pb}_5\text{Bi}_4\text{Se}_{13}$ and $\text{Sn}_{8.65}\text{Pb}_{0.35}\text{Bi}_4\text{Se}_{15}$ contain layers of NaCl (113)-type units with varied thickness, classified as extended lillianite series L(4, 5) and L(4, 7), respectively. $\text{Sn}_2\text{Pb}_5\text{Bi}_4\text{Se}_{13}$ is an n-type, and $\text{Sn}_{8.65}\text{Pb}_{0.35}\text{Bi}_4\text{Se}_{15}$ is a p-type semiconductor with power factors 0.8 and $3.2\mu\text{W}/\text{cmK}^2$ near 300 K, respectively. Both compounds exhibit narrow band gaps that were confirmed by measurements of physical properties and calculations of electronic structure.



Chapter 5

Synthesis and Characterization of Quaternary Selenides $\text{Pb}_{12.92}\text{Sb}_{2.08}\text{Bi}_2\text{Se}_{19}$

Abstract

Quaternary chalcogenides $\text{Pb}_{13}\text{Sb}_{2.08}\text{Bi}_{1.92}\text{Se}_{19}$ was synthesized by solid-state method, and their structures were determined from X-ray diffraction of single crystals. The compound crystallize in monoclinic space group $C2/m$ (No.12) and $P2_1/m$ (No. 11) , with lattice parameters of $\text{Pb}_{13}\text{Sb}_{2.08}\text{Bi}_{1.92}\text{Se}_{19}$: $a = 14.127(3) \text{ \AA}$, $b = 4.2625(8) \text{ \AA}$, $c = 34.477(6) \text{ \AA}$, $\beta = 96.329(4)^\circ$, $R_1/wR_2 = 0.0558/0.0822$, and $GOF = 1.045$. The structure reveal novel structure type and features a three-dimensional framework containing slabs of NaCl-(311) type. $\text{Pb}_{13}\text{Sb}_{2.08}\text{Bi}_{1.92}\text{Se}_{19}$ contains alternate layers of 7 and 8 octahedra wide slabs. Calculations of the band structure, measurements of Seebeck coefficient and electrical conductivity confirm that these compounds are n-type semiconductors with a narrow band gaps.

5. Experiments

5.1.1. Synthesis

All operations were performed in a glove box with a dry nitrogen atmosphere. Chemicals were used as obtained (from Alfa Aesar) – Bi, 99.5 %, powder; Pb, 99.99 %, powder; Sn, 99.9 %; Sb, 99.9 %, powder; Se, 99.95 %, powder. The total masses of samples (all elements combined) were about 0.5 g. All reactants in evacuated fused-silica tubes were placed in resistance furnaces with a controlled temperature.

$\text{Pb}_{12.92}\text{Sb}_{2.08}\text{Bi}_2\text{Se}_{19}$ was first observed on annealing a pressed pellet sample with a reaction molar ratio Pb:Sb:Bi:Se = 4:1:1:7 at 1023K. Cuboid-shaped crystals were observed on the cool side of the silica ampoule. After the structure and composition were confirmed as $\text{Pb}_{12.92}\text{Sb}_{2.08}\text{Bi}_2\text{Se}_{19}$, we attempted to synthesize a pure phase using elements Pb:Sb:Bi:Se = 10.5:2:4.5:19 in stoichiometric proportions, which were heated to 923 K over 12 h and held there for 24 h, followed by cooling at -10 K/h to 823 K, but the product contained impurities BiSe and amorphous phase in small proportions based on powder X-ray diffraction measurements. We subsequently obtained as a pure phase $\text{Pb}_{12.92}\text{Sb}_{2.08}\text{Bi}_2\text{Se}_{19}$ from a reaction with a molar ratio Pb:Sb:Bi:Se = 10.5:2:4.5:19, heating the powder in a pressed-pellet form under vacuum in a tube furnace. The sample was heated to 823 K over 12 h and held at 823 K for 24 h, followed by cooling to 300K naturally in a gradient furnace. The experimental X-ray powder-diffraction pattern (Figure 5.1) of $\text{Pb}_{12.92}\text{Sb}_{2.08}\text{Bi}_2\text{Se}_{19}$ agreed satisfactorily with patterns simulated based on single-crystal data. Energy-dispersive spectra were recorded on the $\text{Pb}_{12.92}\text{Sb}_{2.08}\text{Bi}_2\text{Se}_{19}$ cuboid crystals as synthesized; no impurity from any chemical reactant was detected. This reaction product is stable in air under ambient conditions. Other possible variations of $\text{Pb}_{13}\text{Sb}_2\text{Bi}_2\text{X}_{19}$ (X = S, Se), phase width of $\text{Pb}_{13}\text{Sb}_{4-x}\text{Bi}_x\text{Se}_{19}$ (x = 0, 2, 4) and substituted experiments $\text{M}_{13}\text{Sb}_2\text{Bi}_2\text{Se}_{19}$ (M = Sn) were tested. The products from these reactions are mixtures of binary chalcogenides PbSe or SnSe or Bi_2Se_3 .

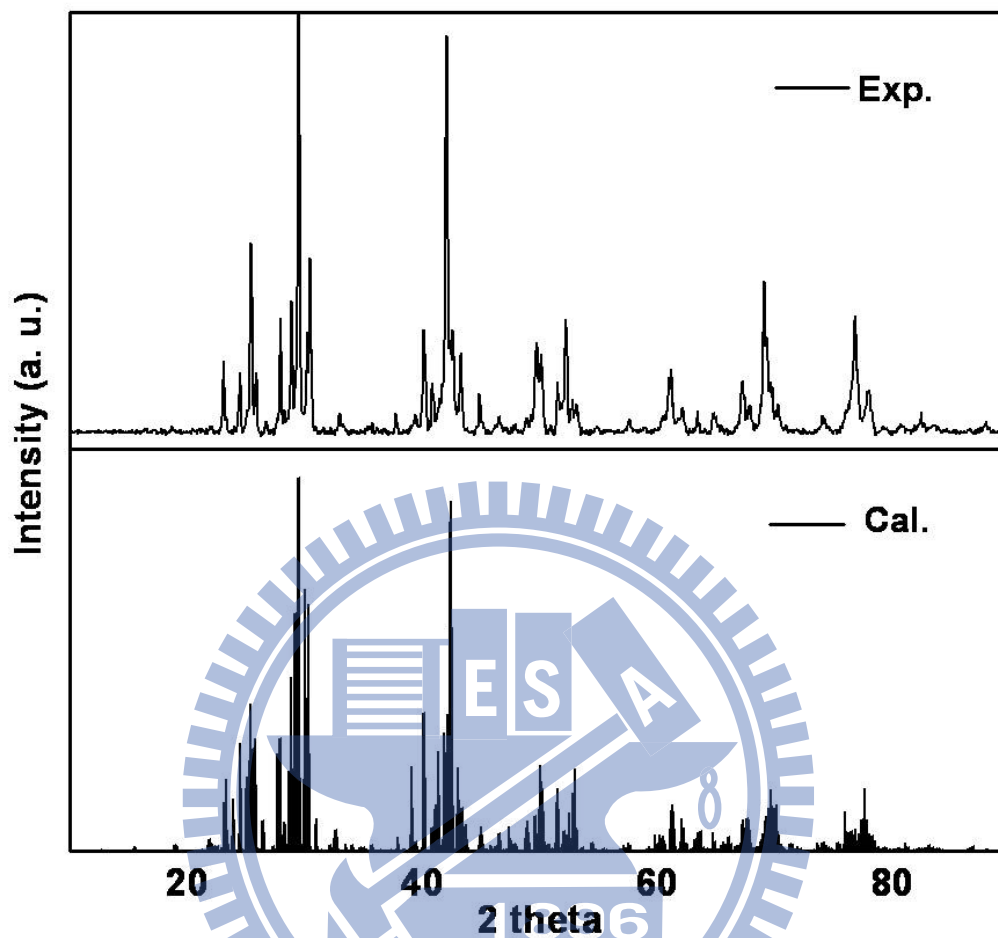


Figure 5.1 Experimental and simulated X-ray powder patterns for $\text{Pb}_{13}\text{Sb}_{2.08}\text{Bi}_{1.92}\text{Se}_{19}$

5.1.2. Single-crystal X-ray diffraction (XRD)

Single crystals of compounds $\text{Pb}_{12.92}\text{Sb}_{2.08}\text{Bi}_2\text{Se}_{19}$ ($0.05 \times 0.04 \times 0.2 \text{ mm}^3$) was mounted on glass fibers with epoxy glue; intensity data were collected on a diffractometer (Bruker APEX CCD) with graphite-monochromated Mo-K α radiation ($\lambda = 0.71073 \text{ \AA}$) at 298(2) K. The distance from the crystal to the detector was 5.038 cm. Data were collected with a scan 0.3° of 600, 600, 435 and 435 frames each at ϕ settings 0° , 90° , 180° and 270° . The duration of exposure was 30 s for both samples; values of 2θ varied between 0.59° -

28.31° and 0.92° - 28.35°, respectively. Diffraction signals obtained from all frames of reciprocal space images were used to determine the parameters of the unit cell. The data were integrated (Siemens SAINT Program) and corrected for Lorentz and polarization effects. Absorption corrections were based on a function fitted to the empirical transmission surface as sampled by multiple equivalent measurements of numerous reflections. The structural model was obtained with direct methods and refined with full-matrix least-square refinement based on F^2 (SHELXTL package). The atomic occupancy for each metal site was determined from the coordination environment compared with literature and a formula valence balance.

The crystal data for the structure determination were selected for a cuboid -shaped crystal that revealed a monoclinic unit cell ($a = 14.127(3) \text{ \AA}$, $b = 4.2625(8) \text{ \AA}$ and $c = 34.477(6) \text{ \AA}$, $V = 2063.4(7) \text{ \AA}^3$); systematic absences indicated space group $C2/m$ (No. 12). Nineteen independent crystallographic sites (M1-9 and Se10-19) were located. The structural refinements displayed unreasonable thermal displacement parameters for sites M2-4 and M6-8, indicative of positions with mixed occupancy of Pb/Sb or Pb/Bi/Sb. The sites (M1, M5), (M2, M6), (M3, M4, M7, M8) and Se7-Se13 were assigned as mixed occupancy of 100% Pb, Pb/Sb, Pb/Bi/Sb and 100 % Se, respectively. The elemental Bi located in M3-4 and M7-8 sites have been constrained according to the bond valence approach model. Assuming Pb^{2+} , Sb^{3+} , Bi^{3+} and Se^{2-} , a near charge-balanced formula $(\text{Pb}^{2+})_{12.92}(\text{Sb}^{3+})_{2.08}(\text{Bi}^{3+})_2(\text{Se}^{2-})_{19}$ was constructed. The final cycle of refinement included anisotropic displacement parameters and a secondary extinction correction performed on F_0^2 with 117 parameters and 2900 independent reflections. Final structural refinements produced $R1/ wR2/ \text{GOF} = 0.0558/0.0822/1.045$.

Crystallographic data and selected bond distances for $\text{Pb}_{13}\text{Sb}_{2.08}\text{Bi}_{1.92}\text{Se}_{19}$ are given in Tables 5.1-5.4.

Table 5.1. Crystallographic Data for $\text{Pb}_{13}\text{Sb}_{2.08}\text{Bi}_{1.92}\text{Se}_{19}$

Empirical formula	$\text{Pb}_{13}\text{Sb}_{2.08}\text{Bi}_{1.92}\text{Se}_{19}$
Formula weight	4848.19
Temperature	300(2) K
Wavelength	0.71073 Å
Crystal system	Monoclinic
Space group	$C2/m$ (No.12)
Unit cell dimensions	$a = 14.127(3)$ Å $b = 4.2625(8)$ Å $c = 34.477(6)$ Å $\beta = 96.329(4)^\circ$.
Volume	$2063.4(7)$ Å ³
Z	2
Density (calculated)	7.803 Mg/m ³
Absorption coefficient	79.074 mm ⁻¹
F(000)	3955
Crystal size	0.05 x 0.04 x 0.2 mm ³
Reflections collected	12288
Independent reflections	2900 [R(int) = 0.0434]
Completeness to theta = 28.24	100.00%
Data / restraints / parameters	2900 / 0 / 117
Goodness-of-fit on F ²	1.045
Final R indices [I > 2sigma(I)]	R1 = 0.0351, wR2 = 0.0739
Largest diff. peak and hole	3.027 and -3.364 e/Å ³

Table 5.2. Fractional Atomic Coordinates and Equivalent Isotropic Atomic DisplacementParameters ($U_{eq} / 10^{-3} \text{ \AA}^2$) and Site Occupancies for $\text{Pb}_{12.92}\text{Sb}_{2.08}\text{Bi}_2\text{Se}_{19}$

	site	x	y	z	sof	U_{eq}^a
M1	2a	0	0	0	100%Pb	21(1)
M2	4i	0.2861(1)	0	0.553(1)	Pb/Sb (0.897(6)/0.103)	20(1)
M3	4i	0.0755(1)	-0.5	0.1124(1)	Pb/Bi/Sb (0.614(5)/0.25/0.136)	22(1)
M4	4i	0.8660(1)	0	0.1645(1)	Pb/Bi/Sb (0.578(6)/0.25/0.21)	24(1)
M5	4i	0.1301(1)	0	0.4727(1)	100%Pb	21(1)
M6	4i	0.8861(1)	-0.5	0.4171(1)	Pb/Sb (0.78(5)/0.22)	20(1)
M7	4i	0.1442(1)	-0.5	0.3604(1)	Pb/Bi/Sb (0.598(6)/0.25/0.16)	23(1)
M8	4i	0.9068(1)	0	0.3086(1)	Pb/Bi/Sb (0.578(6)/0.25/0.211)	25(1)
M9	4i	0.1502(1)	0	0.2357(1)	100%Pb	60(1)
Se10	2d	0	-0.5	0.5		19(1)
Se11	4i	0.1450(1)	-0.5	0.0259(1)		17(1)
Se12	4i	0.9348(1)	0	0.0808(1)		18(1)
Se13	4i	0.0209(1)	0	0.3921(1)		18(1)
Se14	4i	0.2596(1)	-0.5	0.4464(1)		17(1)
Se15	4i	0.2120(1)	0	0.1382(1)		26(1)
Se16	4i	0.7676(1)	-0.5	0.3353(1)		28(1)
Se17	4i	0.0058(1)	-0.5	0.1852(1)		25(1)
Se18	4i	0.7911(1)	0	0.2366(1)		26(1)
Se19	4i	0.0361(1)	-0.5	0.2877(1)		25(1)

^a (U_{eq}) is defined as one third of the trace of the orthogonalized U_{ij} tensor**Table 5.3.** Interatomic Distances for $\text{Pb}_{13}\text{Sb}_{2.08}\text{Bi}_{1.92}\text{Se}_{19}$

M1	—Se11×4	3.022(1)	M2	—Se11×2	3.016(1)	M3	—Se11	3.241(2)
	—Se12×2	3.028(1)		—Se11	3.062(2)		—Se12×2	3.034(1)
				—Se12×2	3.053(1)		—Se15×2	2.945(1)
				—Se15	3.149(2)		—Se17	2.979(2)
M4	—Se12	3.146(2)	M5	—Se10×2	3.0302(5)	M6	—Se10	3.1210(8)
	—Se15×2	3.108(1)		—Se13	3.026(2)		—Se13×2	3.046(1)
	—Se17×2	2.940(1)		—Se14×2	3.014(1)		—Se14×2	3.025(1)
	—Se18	2.806(2)		—Se14	3.040(1)		—Se16	3.119(2)
M7	—Se13×2	3.032(1)	M8	—Se13	3.143(2)	M9	—Se15	3.568(1)
	—Se14	3.224(2)		—Se16×2	3.107(1)		—Se16	3.643(1)
	—Se16×2	2.943(1)		—Se18	2.817(2)		—Se17×2	3.309(2)
	—Se19	2.785(2)		—Se19×2	2.947(1)		—Se18×2	2.915(1)
							—Se19×2	3.315(1)

Table 5.4. Anisotropic Displacement Parameter ($U/10^{-3} \text{ \AA}^2$) for $\text{Pb}_{13}\text{Sb}_{2.08}\text{Bi}_{1.92}\text{Se}_{19}$

	U11	U22	U33	U23	U13	U12
M1	17(1)	21(1)	25(1)	0	1(1)	0
M2	16(1)	18(1)	28(1)	0	1(1)	0
M3	18(1)	21(1)	28(1)	0	3(1)	0
M4	22(1)	23(1)	28(1)	0	2(1)	0
M5	18(1)	20(1)	27(1)	0	2(1)	0
M6	17(1)	18(1)	27(1)	0	5(1)	0
M7	18(1)	23(1)	27(1)	0	1(1)	0
M8	24(1)	23(1)	27(1)	0	2(1)	0
M9	44(1)	35(1)	103(1)	0	12(1)	0
Se10	13(1)	17(1)	27(1)	0	5(1)	0
Se11	12(1)	15(1)	24(1)	0	0(1)	0
Se12	15(1)	17(1)	21(1)	0	1(1)	0
Se13	15(1)	19(1)	21(1)	0	3(1)	0
Se14	14(1)	16(1)	22(1)	0	2(1)	0
Se15	19(1)	19(1)	37(1)	0	-6(1)	0
Se16	25(1)	20(1)	41(1)	0	16(1)	0
Se17	26(1)	26(1)	22(1)	0	1(1)	0
Se18	24(1)	25(1)	28(1)	0	2(1)	0
Se19	26(1)	27(1)	23(1)	0	3(1)	0

The anisotropic displacement factor exponent takes the form $-2\pi^2[h^2a^{*2}U_{11} + k^2b^{*2}U_{22} + l^2c^{*2}U_{33} + 2klb^*c^*U_{23} + 2hla^*c^*U_{13} + 2hka^*b^*U_{12}]$.

5.1.3 Characterization

X-ray powder diffraction analysis of the products was performed using a Bragg–Brentano-type powder diffractometer (Bruker D8 Advance, operated at 40 kV and 40 mA, Cu $K\alpha$, $\lambda = 1.5418 \text{ \AA}$). For phase identification, XRD data were collected over a 2θ range from 5° to 90° with a step interval of 0.05° . The bond valence calculations were performed using valence bond theory with R_0 values of 2.59, 2.67, 2.57, and 2.72 \AA for Sn^{2+} , Pb^{2+} , Sb^{3+} and Bi^{3+} , respectively.

Energy dispersive spectra (SEM/EDX, Hitachi S-4700I High-Resolution Scanning Electron Microscope) were recorded for the cuboid crystalline samples. Semiquantitative EDS analysis of individual crystals of each reaction product confirmed the presence of Sb/Pb/Bi/Se.

Differential thermal analyzer (DTA) and thermogravimetry (TG) measurements were performed using a thermal analyzer (NETZSCH STA 409PC). A powder sample (approximately 30 mg) was placed in an alumina crucible; Al₂O₃ powder served as a reference sample. The sample was heated to 1273 K at 20 K/min under a constant flow of N₂.

5.1.4 Physical Property Measurements

Seebeck coefficients were measured on a cold-pressed bar (1×1×5 mm³) with a commercial thermopower measurement apparatus (MMR Technologies) over the temperature range 300–500 K under a dynamic vacuum (~10⁻² Torr). Constantan served as an internal standard and silver conductive paint was used to create electrical contacts. DC conductivity measurements were performed using a standard four-probe method with a homemade device under vacuum (~10⁻² Torr) over the temperature range 100–300 K. Electrical contacts consisted of four copper wires attached to the bulk with silver glue. Samples were placed under a vacuum for room temperature at least 1 hour to allow the silver glue to dry completely, which improved contact performance. To minimize the effects of grain boundaries in the crystalline powder on the conductivity measurements, each cold-pressed sample was annealed at 773 K for 72 h before measurement.

5.1.5 Calculation of the Electronic Structure

Band calculations with tight-binding linear muffin-tin orbitals (LMTO) were undertaken to understand the electronic structures. The space groups *C2/m* for Pb₁₃Sb₂Bi₂Se₁₉ was used to simulate the observed crystal structures containing mixed-occupancy sites (vide infra). Integration in *k* space were performed with an improved tetrahedron method on grids 16×16×8 unique *k* points in the first Brillouin zone. We analyzed the electronic structure on

extracting information from the band structure, densities of states (DOS), and crystal orbital-hamiltonian population curves (COHP).

5.2 Results and discussion

5.2.1 Crystal Structure

$\text{Pb}_{13}\text{Sb}_{2.08}\text{Bi}_{1.92}\text{Se}_{19}$ crystallizes in a new structure type in monoclinic space group $C2/m$ with two formula units per unit cell. The structure contains nineteen crystallographically inequivalent sites, seven for mixed-occupancy cations ($\text{Pb}^{2+}/\text{Sb}^{3+}$ or $\text{Pb}^{2+}/\text{Bi}^{3+}/\text{Sb}^{3+}$), two for Pb^{2+} and ten for anions (Se^{2-}). Figure 5.2a shows the structure of the $\text{Pb}_{13}\text{Sb}_{2.08}\text{Bi}_{1.92}\text{Se}_{19}$ projection along $[010]$ direction. The structure contains two slabs (I and II) close to NaCl (311) tilt plane with different thickness, which are stitched together by M9-Se to form a three-dimensional framework. Each slab contains octahedral chains that expand alternatively along the c -axis to form ribbon shape units. The refined electronic density map showed that the highest electron accounts (blue atoms in Figure 5.2a) located on slab center of M1, M5 and edge of M9 sites, respectively. The coordination environment of metal sites can be grouped into four types: (i) Site M1 and M5 are hexa-coordinate in a near ideal octahedron with average M-Se distance 3.025 Å, which were refined as fully occupied Pb atoms. (ii) The coordination polyhedral around M2-M3 and M6-M7 sites are distorted octahedral with a square pyramid having one short (~ 2.79 Å), four intermediate (2.94-3.03 Å), and one longer (~ 3.3 Å). These sites are mixed occupied with Pb/Sb or Pb/Bi/Sb. (iii) M4 and M8 sites are six coordinated in trigonal pyramid environment with three short M-Se bonds (~ 2.91 Å) opposite to three longer ones (3.12 Å). These sites are mixed occupied with Pb/Bi/Sb. (iv) The M9 site is occupied by 100%Pb, which located on the edge plane of two slabs that exhibits bi-capped trigonal prism coordination environment.

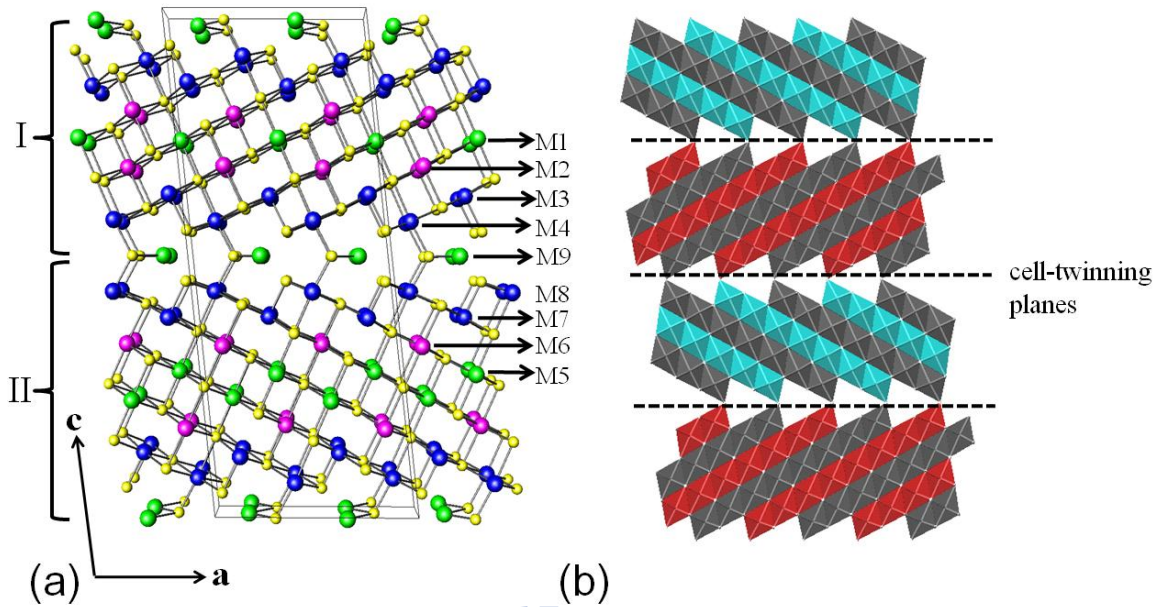


Figure 5.2 Crystal structures of $\text{Pb}_{13}\text{Sb}_{2.08}\text{Bi}_{1.92}\text{Se}_{19}$ (a) projection along $[010]$ direction with slightly perspective and (b) representation using octahedra chains with different slab thickness.

The M-Se distances in $\text{Pb}_{13}\text{Sb}_{2.08}\text{Bi}_{1.92}\text{Se}_{19}$ structures are comparable to a binary system and some multinary selenide chalcogenides in the literature that contain mixed occupancy of Bi/Sb or Pb/Sb, such as $\text{Pb}_4\text{Sb}_4\text{Se}_{10}$ ⁷⁴, PbBi_2Se_4 ⁷⁶, $\text{InSn}_2\text{Bi}_3\text{Se}_8$ ⁶³, and $\text{Sn}_2\text{Pb}_5\text{Bi}_4\text{Se}_{13}$. According to the bond valence calculation, the M1 and M5 sites are favor for +2 charges of Pb atoms. The distorted octahedral environments (M2-M3 and M6-M7 sites) are due to the lone pair effect, as observed in similar (Bi/Sb)-Se or Pb-Se contacts for known chalcogenides with Sb, Bi, Pb as the constituent element. The M-Se distances varying between 2.87 and 3.31 Å in a trigonal prism environment and two long M9-Se contacts between 3.57 and 3.64 Å without bonding interaction.

The structures of $\text{Pb}_{13}\text{Sb}_{2.08}\text{Bi}_{1.92}\text{Se}_{19}$ belong to the lillianite homologous series that are described by the symbol L_n, n' where L indicates a member of the lillianite series and n and n' correspond to the number of octahedra between two sides of the trochochemical cell-twinning plane. The symbol $L(n, n')$ reflects the cation/anion ratio (M/X). The limit of the

ratio M/X is located within 1 (PbS for $L(\infty, \infty)$) and 0.714 (PbBi₄S₇ for $L(2, 1)$). In the same way that the symbol $L(7, 8)$ can be assigned for Pb₁₃Sb_{2.08}Bi_{1.92}Se₁₉ ($M/X = 0.895$). The polysynthetic twinning in NaCl-(311) type exhibits a ratio M/X decreasing with increasing the number of octahedral n . The phase Pb₁₃Sb_{2.08}Bi_{1.92}Se₁₉ represents a new structure type of extended lillianite series. Although $L(7, 8)$ phase has been proposed to be existed in the mineral Ag₂PbBi₂S₅ system by TEM study, neither structure nor bulk material had been isolated.

5.2.2. Electronic Structure

To understand the electronic structure of $L(7, 8)$ phase, a charge-balanced model of Pb₁₃Sb₂Bi₂Se₁₉ was constructed with the cation sites assigned to Pb(M1-2, M4-5, M7-9), Bi(M3) and Sb(M6). Projections of the corresponding total and partial densities of states (DOS, PDOS) for atoms in slabs I and II are presented in Figure 5.3. In general, the DOS curve exhibits filled valence band with narrow band gaps, indicative of a semiconducting property. As seen from the DOS curve, the contributions of metal atoms above the Fermi energy domination from atoms of slab II, while the large maximum below the Fermi level shows nearly equal contribution with slab I and II. The large feature between -6 eV and the Fermi level is dominated by chalcogenide-based filled p orbitals, whereas the bottom of the conduction band is based mainly on empty p orbitals of the main-group metal. The ns states of Pb, Sb and Bi atoms are essentially localized and shown in sharp peaks centered at ca. -7 to -10 eV, which might result from the inert-pair effect commonly observed in heavy main-group elements. The results indicate that bonding states of the (Sb, Pb, Bi)-Se contacts are occupied and well below the Fermi level with small contributions of antibonding interactions near the Fermi level. Despite the antibonding interactions near the Fermi level, the

bonding character remains, with average ICOHP values 0.63, 0.84 and 0.91 eV/bond for Pb-Se, Sb-Se and Bi-Se contacts, respectively.

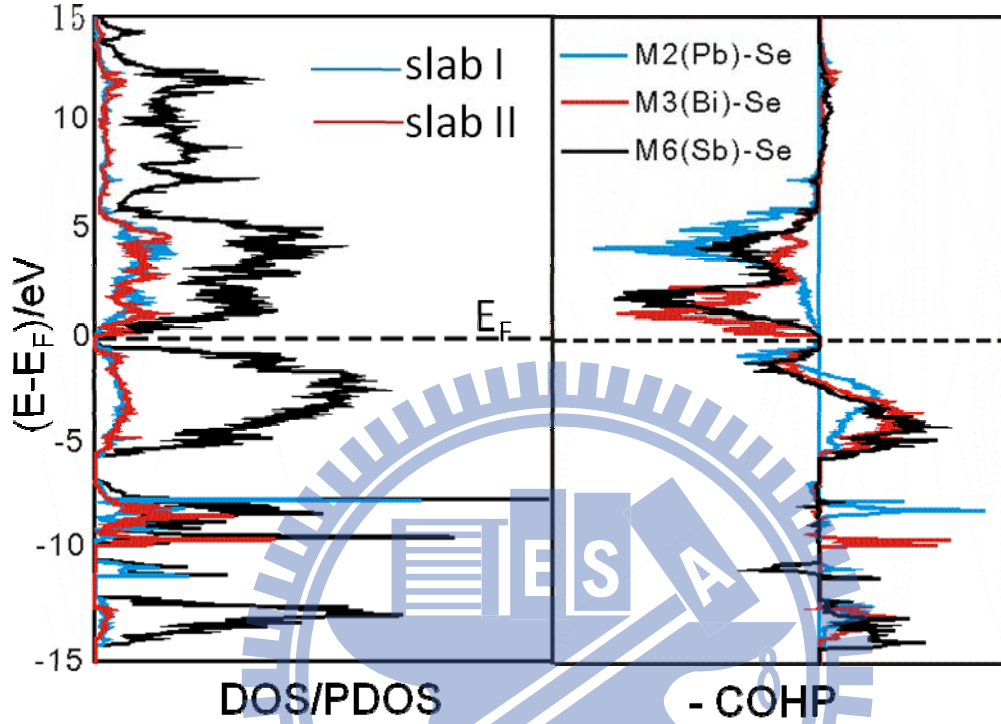


Figure 5.3 Density of states (left), partial density of states, and crystal-orbital hamiltonian populations (COHP) for selected M-Se (M2-Se : blue line, M3-Se : black dashed line, and M6-Se : red line) interactions (right) curves of $\text{Pb}_{13}\text{Sb}_{2.08}\text{Bi}_{1.92}\text{Se}_{19}$. The horizontal dashed line denotes the Fermi energy (E_F). The contributions from slab I (M1 (Pb) + M2 (Pb) + M3 (Bi) + M4 (Pb)) and slab II (M5 (Pb) + M6 (Sb) + M7 (Pb) + M8 (Pb)) are denoted with blue and red lines.

5.2.3 Physical Properties

A standard four-probe technique was used to measure the temperature-dependent resistivity from 100 to 300K. The results show that $\text{Pb}_{13}\text{Sb}_{2.08}\text{Bi}_{1.92}\text{Se}_{19}$ exhibits decreasing resistivity with increasing temperature, hence conforming to a trend typical of a

semiconductor (Figure 5.4). Figure 5.4 reveals the Seebeck coefficient measurement for $\text{Pb}_{13}\text{Sb}_{2.08}\text{Bi}_{1.92}\text{Se}_{19}$. The compound shows slight temperature dependence of the Seebeck coefficient. The thermopower of $\text{Pb}_{13}\text{Sb}_{2.08}\text{Bi}_{1.92}\text{Se}_{19}$ shows negative Seebeck coefficient ~ 74 $\mu\text{V}/\text{K}$ for the whole temperature range which results indicate *n*-type semiconducting behavior.

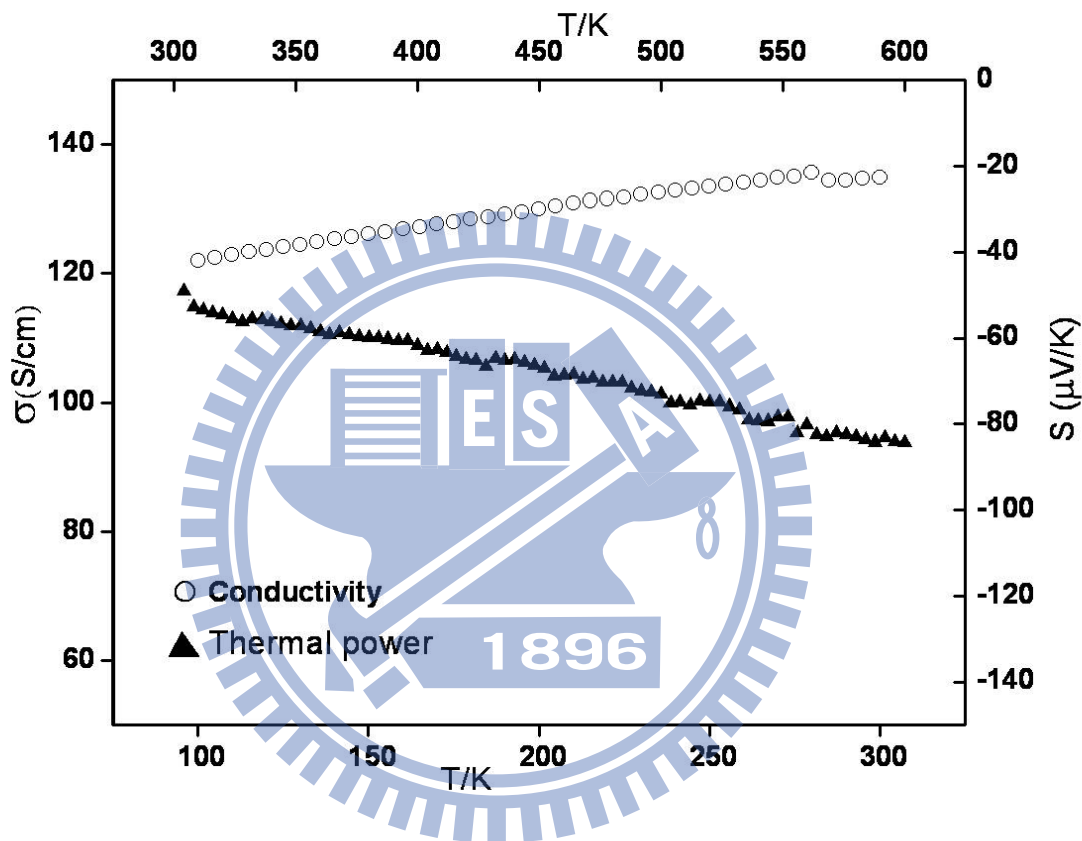


Figure 5.4 Electrical conductivity and thermal power of $\text{Pb}_{13}\text{Sb}_{2.08}\text{Bi}_{1.92}\text{Se}_{19}$

5.2.4 Thermoanalyses

The TG-DSC versus the temperature for $\text{Pb}_{13}\text{Sb}_{2.08}\text{Bi}_{1.92}\text{Se}_{19}$ is shown in Fig. 5.5. The TG-DSC measurements show similar features with the maximum exothermic peaks and mass

loss start at 1132K. These results were reproduced by heating the as-synthesized powder in a quartz ampoule under vacuum and subsequently heating to 900°C. The PXRD pattern of the residue is indexed as a combination of PbSe, Sb₂Se₃, BiSe, Se and amorphous phase in the residual products.

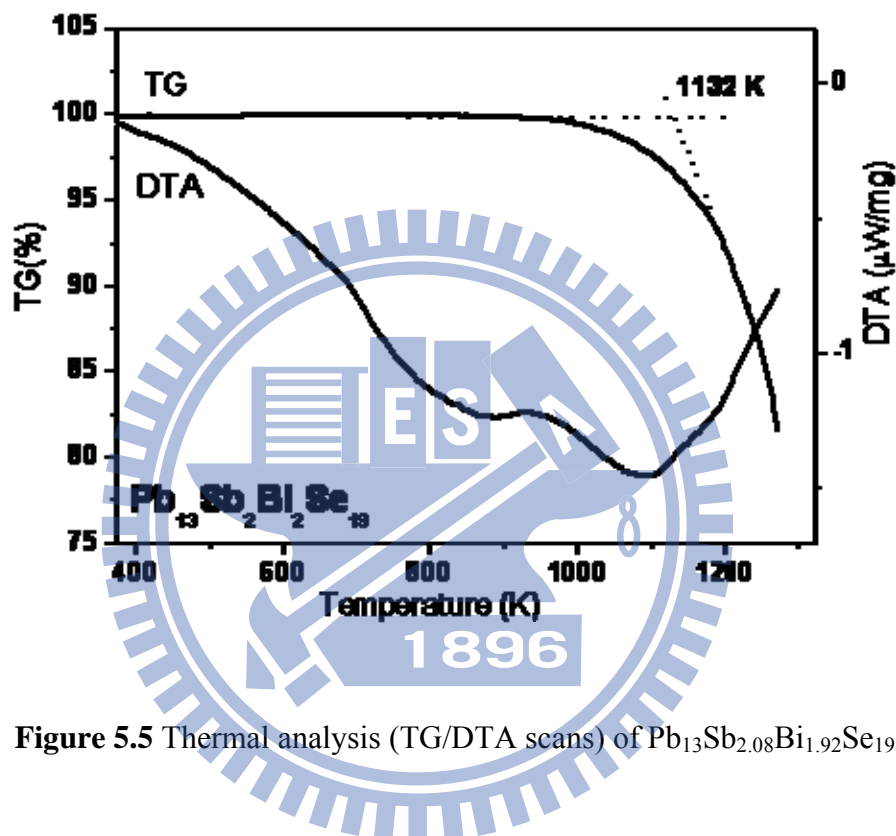


Figure 5.5 Thermal analysis (TG/DTA scans) of Pb₁₃Sb_{2.08}Bi_{1.92}Se₁₉

5.3 Conclusions

We obtained new quaternary chalcogenides Pb₁₃Sb_{2.08}Bi_{1.92}Se₁₉ in Pb-Sb-Bi-Se system. The structure contains layers of NaCl(311)-type units with varies thickness, which can be grouped to extended lillianite series of (L 7, 8) and belongs to new structure type. The physical property shows that p-type semiconductor with power factors of 1.6 μW/cmK² at room temperature. The compounds exhibit narrow band gaps that were confirmed by physical property measurements and electronic structure calculations.

Chapter 6

Synthesis and Characterized of New Quaternary Chalcogenides $\text{Sn}_4\text{Bi}_{10}\text{Se}_{19}$ and $\text{Sn}_{8.5}\text{Pb}_{1.5}\text{Bi}_{18}\text{Se}_{37}$

Abstract

Quaternary chalcogenides $\text{Sn}_4\text{Bi}_{10}\text{Se}_{19}$ and $\text{Sn}_{8.5}\text{Pb}_{1.5}\text{Bi}_{18}\text{Se}_{37}$ were synthesized by solid-state methods, and their structures were determined from X-ray diffraction of single crystals. Both compounds crystallize in monoclinic space group $C2/m$ (No.12), with lattice parameters of $\text{Sn}_4\text{Bi}_{10}\text{Se}_{19}$: $a = 28.201(5) \text{ \AA}$, $b = 4.1641(8) \text{ \AA}$, $c = 21.263(4) \text{ \AA}$, $\beta = 130.995(3)^\circ$, $RI/wR2/GOF = 0.039/0.0824/1.049$; $\text{Sn}_{8.5}\text{Pb}_{1.5}\text{Bi}_{18}\text{Se}_{37}$: $a = 28.201(5) \text{ \AA}$, $b = 4.1641(8) \text{ \AA}$, $c = 21.263(4) \text{ \AA}$, $\beta = 130.995(3)^\circ$, $RI/wR2/GOF = 0.0342/0.0664/0.965$. Both structures reveal novel structure type and analogs to members of new homologous series, $[\text{M}_{2x}\text{Se}_{2x+2}][\text{M}_{2y-2z}\text{Se}_{3y-2z-1}]$. The structures contain NaCl(111)-type unit and NaCl(100)-type units with varied length. The detail purification, physical properties and electronic calculation are progress.

Synthesis

$\text{Sn}_4\text{Bi}_{10}\text{Se}_{19}$ and $\text{Sn}_{8.5}\text{Pb}_{1.5}\text{Bi}_{18}\text{Se}_{37}$ were performed in a dry nitrogen atmosphere glovebox. Chemicals were used as obtained (from Alfa Aesar) – Bi, 99.95 %, powder; Sn, 99.5 %, powder; Pb, 99.9 %, powder; Se, 99.95 %, powder. The total sample masses (all elements combined) were around 0.5 g. All reactant mixtures were placed in evacuated fused silica tubes placed into temperature-controlled resistance furnaces. All reactants in evacuated fused-silica tubes were placed in resistance furnaces with controlled temperature.

$\text{Sn}_4\text{Bi}_{10}\text{Se}_{19}$ was initially observed from a reaction intended to synthesized “ $\text{Sn}_7\text{Bi}_{21}\text{Se}_{37}$ ”. The reaction mixture was heated slowly to 800 °C within 12 h. This temperature was maintained for 18h and finally to about 23 °C on simply terminating the power. The product, observed under the optical microscopy, contained a molten part and cuboids shape crystals. Based on the powder X-ray diffraction experiment, the product ‘ $\text{Sn}_7\text{Bi}_{21}\text{Se}_{37}$ ’ of the reaction is a mixture of $\text{Sn}_4\text{Bi}_{10}\text{Se}_{19}$, Bi_2Se_3 , $\text{Sn}_3\text{Bi}_2\text{Se}_6$ and an unknown phase. Reaction with different ratios of Sn/Bi in $\text{Sn}_{4-x}\text{Bi}_{10+x}\text{Se}_{19}$ and $\text{M}_x\text{Sn}_{4-x}\text{Bi}_{10}\text{Se}_{19}$ (M=Pb) were utilized to carried out the pure phase with the same heating conditions as specified above, but all failed.

$\text{Sn}_{8.5}\text{Pb}_{1.5}\text{Bi}_{18}\text{Se}_{37}$ was initially synthesized in order to stabilize the $\text{Sn}_{10}\text{Bi}_{18}\text{Se}_{36}$ phase and the heating conditions is the same as specified above. The product, observed under the optical microscopy, contained a molten part and cuboids shape crystals. Based on the powder X-ray diffraction experiment, the product contains mixtures of SnSe, Bi_2Se_3 , BiSe and an unknown phase. Measurements on a cuboids shape crystal revealed a quaternary phase with formula of $\text{Sn}_{8.5}\text{Pb}_{1.5}\text{Bi}_{18}\text{Se}_{37}$. Reactions with different ratios of Sn/Pb in $\text{Sn}_{10-x}\text{Pb}_x\text{Bi}_{18}\text{Se}_{37}$ or $(\text{Sn}/\text{Pb})_{10+x}\text{Bi}_{19-x}\text{Se}_{37}$ were utilized to obtain the stable phase with the same heating conditions

as specified above. The products of each reaction revealed silvery, brittle ingots that were neither air nor moisture sensitive and contain mixtures of PbSe, SnSe₂, Sn₃Bi₂Se₆, Bi₂Se₃ and unknown phase.

Single-crystal X-ray diffraction (XRD)

Single crystals of compounds (1) Sn₄Bi₁₀Se₁₉ (0.25 × 0.2 × 0.5 mm³) and (2) Sn_{8.5}Pb_{1.5}Bi₁₈Se₃₇ (0.2 × 0.2 × 0.5 mm³) were mounted on glass fibers with epoxy glue; intensity data were collected on a diffractometer (Bruker APEX CCD) with graphite-monochromated Mo-K α radiation ($\lambda = 0.71073 \text{ \AA}$) at 298(2) K. The distance from crystal to detector was 5.038. Data were collected with a scan 0.3 $^\circ$ in groups of 600 frames each at θ settings 0 $^\circ$, 90 $^\circ$, 180 $^\circ$ and 270 $^\circ$. The duration of exposure was 30s for both samples. The 2θ values varied between 1.27 $^\circ$ and 28.35 $^\circ$. Diffraction signals obtained from all frames of reciprocal space images were used to determine the unit-cell parameters. The data were integrated using the Siemens SAINT program and were corrected for Lorentz and polarization effects. Absorption corrections were based on a function fitted to the empirical transmission surface as sampled by multiple equivalent measurements of numerous reflections. The structural model was obtained with direct methods and refined by full-matrix least-square refinement based on F^2 using the SHELXTL package. The atomic occupancy for each metal site was determined by the coordinated environment which compared with literature and formula valence balance.

1) Sn₄Bi₁₀Se₁₉:

The rod shape crystal of Sn₄Bi₁₀Se₁₉ revealed a monoclinic unit cell ($a = 28.201(5) \text{ \AA}$, $b = 4.1641(8) \text{ \AA}$, $c = 21.263(4) \text{ \AA}$, $\beta = 130.995(3)^\circ$ and $V = 1884.6(6) \text{ \AA}^3$) and the systematic

absences suggested space group of $C2/m$ (No. 12). Seventeen crystallographic sites (M1-7 and Se8-17) were located. The structural refinement displayed exceptionally thermal displacement parameters for site M1-7, indicative of positions with mixed occupancy of Bi/Sn. These site distributions reveal a charge-balanced formula $(\text{Sn}^{2+})_{2.82}(\text{Bi}^{3+})_{10.18}(\text{Se}^{2-})_{19}$. The final cycle of refinement included anisotropic displacement parameters and a secondary extinction correction performed on F_0^2 with 108 parameters and 2657 independent reflections. Final structural refinements produced $RI/wR2/GOF = 0.039/0.0824/1.049$.

2) $\text{Sn}_{8.5}\text{Pb}_{1.5}\text{Bi}_{18}\text{Se}_{37}$:

For $\text{Sn}_{8.5}\text{Pb}_{1.5}\text{Bi}_{18}\text{Se}_{37}$, X-ray measurements on a single crystal revealed a monoclinic unit cell ($a = 32.019(6) \text{ \AA}$, $b = 4.1610(8) \text{ \AA}$, $c = 31.433(7) \text{ \AA}$, $\beta = 117.997(4)^\circ$ and $V = 3698(1) \text{ \AA}^3$) and the systematic absences suggested space group of $C2/m$ (No. 12). Thirty-one crystallographic sites (M1-M14, and Se15-31) were found. The cationic sites M1-M14 have mixed occupation by Bi/Sn and Pb/Sn atoms due to their atypical parameters for thermal displacement when refined with full occupancy by Sn, Pb or Bi. Assuming $\text{Sn}^{2+}/\text{Pb}^{2+}$, Bi^{3+} and Se^{2-} , a charged-balanced formula $(\text{Sn}^{2+})_{8.22}(\text{Pb}^{2+})_{1.74}(\text{Bi}^{3+})_{18.06}(\text{Se}^{2-})_{37}$ was constructed that served to constrain the occupancies of the disordered sites. The final cycle of refinement included anisotropic displacement parameters and a secondary extinction correction performed on F_0^2 with 212 parameters and 5226 independent reflections. Final structural refinements produced $\text{Sn}_{8.65}\text{Pb}_{0.35}\text{Bi}_{18}\text{Se}_{37}$ with $RI/wR2/GOF = 0.0342/0.0664/0.965$. Crystallographic data and selected bond distances for $\text{Sn}_4\text{Bi}_{10}\text{Se}_{19}$ and $\text{Sn}_{8.5}\text{Pb}_{1.5}\text{Bi}_{18}\text{Se}_{37}$ are given in Tables 6.1-6.5.

Table 6.1 Crystallographic Data for $\text{Pb}_4\text{Bi}_{10}\text{Se}_{19}$ and $\text{Sn}_{8.5}\text{Pb}_{1.5}\text{Bi}_{18}\text{Se}_{37}$

Empirical formula	$\text{Sn}_{3.82}\text{Bi}_{10.18}\text{Se}_{19}$	$\text{Sn}_{8.22}\text{Pb}_{1.74}\text{Bi}_{18.06}\text{Se}_{37}$
Formula weight	4064.80	8002.81
Temperature	300(2) K	300(2) K
Wavelength	0.71073 Å	0.71073 Å
Crystal system	Monoclinic	Monoclinic
Space group	$C2/m$ (No.12)	$C2/m$ (No.12)
a / Å	28.201(5)	32.019(6)
b / Å	4.1641(8)	4.1610(8)
c / Å	21.263(4)	31.433(7)
β / deg	130.995(3)	117.997(4)
V / Å ³	1884.6(6)	3698(1)
Z	2	2
$\theta_{\min}, \theta_{\max}$ / deg	1.27, 28.28	0.73, 28.28
Independent(R_{int}),	2657 (0.0556)	5226 (0.0533)
observed reflections	11109	21960
$d_{\text{calcd.}}$ / g cm ⁻³	7.163	7.188
Absorption coefficient	67.443	67.082
Goodness of fit on F^2	1.049	0.965
R_1, wR_2 (all data) ^a	0.0478, 0.0857	0.0553, 0.0740
R_1, wR_2 ($I > 2\sigma(I)$)	0.0390, 0.0824	0.0342, 0.0664

$$^a R_1 = \frac{\sum ||F_0| - |F_c||}{\sum |F_0|} \quad wR_2 = \left\{ \frac{\sum [w(F_0^2 - F_c^2)^2]}{\sum [w(F_0^2)^2]} \right\}^{1/2}$$

Table 6.2 Fractional Atomic Coordinates and Equivalent Isotropic Atomic Displacement Parameters ($U_{eq} / 10^{-3} \text{ \AA}^2$) and Site Occupancies for $\text{Sn}_4\text{Bi}_{10}\text{Se}_{19}$

	x	y	z	sof	U_{eq}
M1	0.3442(1)	0.5	0.3216(1)	Bi/Sn(0.455(8)/0.545)	22(1)
M2	0.2282(1)	0.5	0.4020(1)	Bi/Sn(0.784(8)/0.216)	12(1)
M3	0.4017(1)	0	0.5436(1)	Bi/Sn(0.875(9)/0.125)	14(1)
M4	0.2041(1)	0	0.394(1)	Bi/Sn(0.564(8)/0.436)	14(1)
M5	0.48(1)	0	0.1493(1)	Bi/Sn(0.788(8)/0.212)	14(1)
M6	0.959(1)	0.5	-0.2048(1)	Bi/Sn(0.749(8)/0.251)	13(1)
M7	0.1069(1)	0.5	0.943(1)	Bi/Sn(0.884(8)/0.116)	14(1)
Se(8)	0	0	0		10(1)
Se(9)	0.2004(1)	0	0.1692(1)		14(1)
Se(10)	0.1012(1)	0.5	-0.515(1)		10(1)
Se(11)	0.2991(1)	0.5	0.1211(1)		19(1)
Se(12)	0.970(1)	0.5	0.2235(1)		13(1)
Se(13)	0.2907(1)	0	0.3815(1)		11(1)
Se(14)	0.1683(1)	0	0.4282(1)		9(1)
Se(15)	-0.32(1)	0	0.2775(1)		10(1)
Se(16)	0.4377(1)	0.5	0.4953(1)		12(1)
Se(17)	0.781(1)	0.5	-0.3486(1)		12(1)

(U_{eq}) is defined as one third of the trace of the orthogonalized U_{ij} tensor

Table 6.3 Interatomic Distances for $\text{Sn}_4\text{Bi}_{10}\text{Se}_{19}$.

M1	—Se17×2	2.79693	M4	—Se9	2.83093	M7	—Se8×2	3.08356
	—Se16	2.79591		—Se10×2	3.02237		—Se9×2	2.88414
	—Se13×2	3.27792		—Se11×2	2.90200		—Se10	2.99850
	—Se11	3.56209		—Se11	3.35268		—Se12	2.93683
M2	—Se14	2.78112	M5	—Se8	3.08693			
	—Se14×2	2.95547		—Se10×2	3.07269			
	—Se13×2	2.94018		—Se11×2	2.87324			
	—Se12	3.11014		—Se15	2.87999			
M3	—Se13	2.74205	M6	—Se10	3.16255			
	—Se14×2	3.18356		—Se11×2	3.05950			
	—Se15×2	3.56539		—Se15×2	2.87321			
	—Se14	2.79041		—Se17	2.75472			

Table 6.4 Fractional Atomic Coordinates and Equivalent Isotropic Atomic Displacement Parameters ($U_{eq} / 10^{-3} \text{ \AA}^2$) and Site Occupancies for $\text{Sn}_{8.5}\text{Pb}_{1.5}\text{Bi}_{18}\text{Se}_{37}$

	x	y	z	sof	U(eq)		x	y	z	U(eq)
M1	0.8368(1)	0	-0.451(1)	Bi(0.612)	21(1)	Se15	0.9335(1)	0	0.0103(1)	21(1)
M2	0.7464(1)	0	0.1712(1)	Pb(0.256)	20(1)	Se16	0.6515(1)	0	0.1033(1)	18(1)
M3	0.8237(1)	-0.5	0.2964(1)	Bi(0.575)	19(1)	Se17	0.7285(1)	-0.5	0.2223(1)	18(1)
M4	0.8952(1)	0	0.4232(1)	Pb(0.307)	20(1)	Se18	0.8008(1)	0	0.3446(1)	21(1)
M5	0.0301(1)	0.5	0.4485(1)	Bi(0.832)	19(1)	Se19	0.9749(1)	-0.5	0.2670(1)	22(1)
M6	0.9567(1)	0	0.3190(1)	Bi(0.843)	21(1)	Se20	0.8931(1)	0	0.1334(1)	21(1)
M7	0.8785(1)	-0.5	0.1879(1)	Bi(0.851)	22(1)	Se21	0.8196(1)	0.5	0.0124(1)	28(1)
M8	0.7968(1)	0	0.0637(1)	Bi(0.470)	23(1)	Se22	0.7740(1)	-0.5	0.1169(1)	17(1)
M9	0.9465(1)	0.5	0.753(2)	Bi(0.874)	32(1)	Se23	0.8540(1)	0	0.2442(1)	17(1)
M10	0.0568(1)	0.5	0.2381(1)	Bi(0.777)	22(1)	Se24	0.9281(1)	0.5	0.3721(1)	17(1)
M11	0.2643(1)	0	0.4514(1)	Bi(0.832)	27(1)	Se25	0	0	0.5	17(1)
M12	0.2643(1)	0	0.4514(1)	Bi(0.919)	27(1)	Se26	0.0136(1)	0	0.1637(1)	20(1)
M13	0.1833(1)	0	0.2980(1)	Bi(0.885)	30(1)	Se27	0.1034(1)	0	0.3137(1)	20(1)
M14	0.0825(1)	0	0.1353(1)	Bi(0.857)	24(1)	Se28	0.1890(1)	0	0.4708(1)	20(1)
						Se29	0.2131(1)	-0.5	0.3802(1)	21(1)
						Se30	0.1355(1)	0.5	0.2249(1)	18(1)
						Se31	0.0323(1)	0.5	0.0720(1)	20(1)

Table 6.5 Interatomic Distances for $\text{Sn}_{8.5}\text{Pb}_{1.5}\text{Bi}_{18}\text{Se}_{37}$.

M1	—Se1	2.74864	M6	—Se6	2.91281	M10	—Se7	3.15267
	—Se2×2	2.9092		—Se7×2	2.86904		—Se14×2	2.94439
	—Se9×2	2.97294		—Se11	3.01348		—Se15×2	2.97839
	—Se10	3.18713		—Se12×2	3.06371		—Se18	2.74096
M2	—Se2	2.77543	M7	—Se7	2.91584	M11	—Se6×2	3.40192
	—Se3×2	2.84722		—Se8×2	2.86939		—Se15×2	3.05544
	—Se10*2	3.07095		—Se10	3.02759		—Se16×2	3.04774
	—Se11	3.11594		—Se11×2	3.06306		—Se17	2.77685
M3	—Se3	2.83542	M8	—Se8	2.82274	M12	—Se5	3.26312
	—Se4×2	2.86203		—Se9×2	2.92382		—Se16×2	3.01995
	—Se11×2	3.07495		—Se10	2.96925		—Se17×2	2.92843
	—Se12	3.0626		—Se9	3.35278		—Se16	2.7498
M4	—Se4	2.86776	M9	—Se1×2	2.80561	M13	—Se3	3.31551
	—Se5×2	2.85243		—Se8×2	3.67721		—Se15	2.82491
	—Se12×2	3.09911		—Se9	3.58928		—Se17×2	3.09756
	—Se13	3.08		—Se14×2	3.32688		—Se18×2	2.94274
M5	—Se5	2.90167		—Se19	2.79662	M14	—Se2×2	3.50612
	—Se6×2	2.86597					—Se14	2.74362
	—Se12	3.01109					—Se18×2	3.2638
	—Se13×2	3.05795					—Se19×2	2.8057

Structure description

Figure 6.1 shows the structure of $\text{Sn}_4\text{Bi}_{10}\text{Se}_{19}$ and $\text{Sn}_{8.5}\text{Pb}_{1.5}\text{Bi}_{18}\text{Se}_{37}$ in a projection along the crystallographic b -axis [010]. The building units $[\text{M}_{2x}\text{Se}_{2x+2}]$ and $[\text{M}_{2y-2z}\text{Se}_{3y-2z-1}]$ are corresponding to NaCl(100)-type unit and NaCl(111)-type unit, respectively, where x and y values are the length of the two building units; subsequently, the z controls the type of the NaCl(111)-type module that the $[\text{M}_{2y-2z}\text{Se}_{3y-2z-1}]$ unit diminishes (M_2Se_2) with the z value increased. These compounds will discuss together with other $[\text{M}_{2x}\text{Se}_{2x+2}][\text{M}_{2y-2z}\text{Se}_{3y-2z-1}]$ series compounds that synthesized from our group such as $\text{Sn}_4(\text{In/Sb})_{14}\text{Se}_{25}$, $\text{Sn}_{18}\text{Sb}_{12}\text{Se}_{36}$, $\text{Sn}_{10}(\text{In/Sb})_{18}\text{Se}_{37}$ and $\text{Sn}_8(\text{In/Sb})_{18}\text{Se}_{35}$.

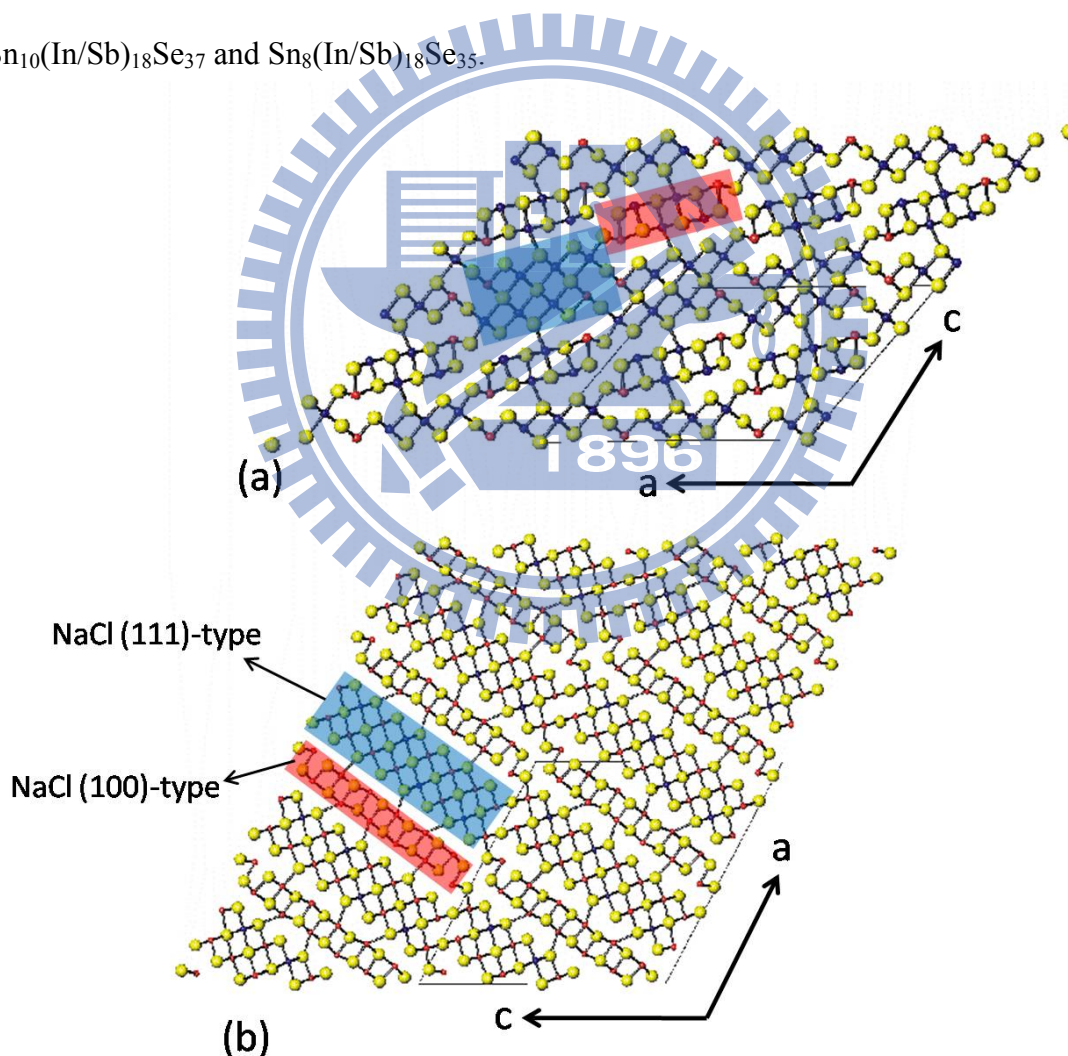


Figure 6.1 show the structure of $\text{Sn}_4\text{Bi}_{10}\text{Se}_{19}$ and $\text{Sn}_{8.5}\text{Pb}_{1.5}\text{Bi}_{18}\text{Se}_{37}$ in a projection along the crystallographic b -axis [010].

Chapter 7

Conclusions

The new selenides $\text{Sn}_{3-\delta}\text{Pb}_\delta\text{Bi}_2\text{Se}_6$ ($\delta = 0 - 0.7$), $\text{Pb}_x\text{Sn}_{6-x}\text{Bi}_2\text{Se}_9$ ($x=0 - 4.36$), $\text{Sn}_2\text{Pb}_5\text{Bi}_4\text{Se}_{13}$, $\text{Sn}_{8.65}\text{Pb}_{0.35}\text{Bi}_4\text{Se}_{15}$ and $\text{Pb}_{13}\text{Sb}_{2.08}\text{Bi}_{1.92}\text{Se}_{19}$ have been synthesized and characterized. These compounds exhibit slabs of NaCl (311) tilt planes with disparate thickness, and the structures are defined with topochemical cell-twinning symbols L(4,4), L(7,7), L(4,5), L(4,7) and L(7,8).

The quaternary chalcogenides $\text{Sn}_{3-\delta}\text{Pb}_\delta\text{Bi}_2\text{Se}_6$ ($\delta = 0.1-0.7$) were synthesized and their structures are related to that of $\text{Pb}_3\text{Bi}_2\text{S}_6$ with an atomic position near the cell-twinning plane. Single-crystal analysis of these new phases identified a different space group, *Pnma* (No. 62), that contained a metal site close to the mirror plane. The percent composition of Pb was gradually changed to study the effects of Pb on the structure and coordination environments of metal sites. Electronic calculations were also carried out to evaluate the effects of the Pb^{2+} ion on the structure and coordination environments of the cations.

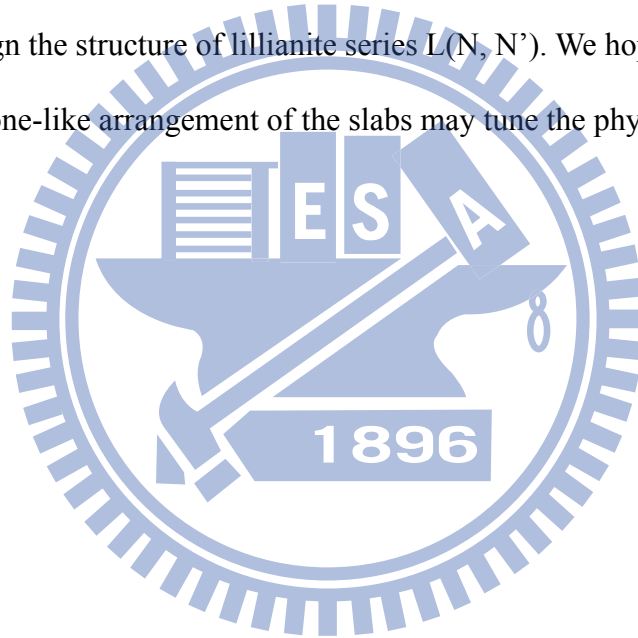
The Solid-solution $\text{Pb}_x\text{Sn}_{6-x}\text{Bi}_2\text{Se}_9$ ($x=0 - 4.36$) belong to mineral, heyrovskiyite. Theoretical calculation exhibits that the average ICOHP for Sn-Se (4.25) is greater than Pb-Se (4.00) contact, indicative of strong bonding strength for Sn-Se compared with Pb-Se contact, which consistent with the experimental results.

New quaternary chalcogenides $\text{Sn}_2\text{Pb}_5\text{Bi}_4\text{Se}_{13}$ and $\text{Sn}_{8.65}\text{Pb}_{0.35}\text{Bi}_4\text{Se}_{15}$ were synthesized in the Sn-Pb-Bi-Se system. No possible phase width in these two systems were confirmed after react with varied ratios Pb/Sn in $\text{Sn}_x\text{Pb}_{7-x}\text{Bi}_4\text{Se}_{13}$ ($x = 0, 2, 4, 6, 7$) and $\text{Sn}_x\text{Pb}_{9-x}\text{Bi}_4\text{Se}_{15}$ ($x = 0, 0.35, 0.5, 1, 9$). The Seebeck results indicate *n*-type and *p*-type semiconducting behavior for

$\text{Sn}_2\text{Pb}_5\text{Bi}_4\text{Se}_{13}$ and $\text{Sn}_{8.65}\text{Pb}_{0.35}\text{Bi}_4\text{Se}_{15}$, respectively.

The new structure type of quaternary chalcogenides $\text{Pb}_{13}\text{Sb}_{2.08}\text{Bi}_{1.92}\text{Se}_{19}$ was synthesized by solid-state methods. Calculations of the band structure, measurements of Seebeck coefficient and electrical conductivity confirm that $\text{Pb}_{13}\text{Sb}_{2.08}\text{Bi}_{1.92}\text{Se}_{19}$ is an n-type semiconductor with small band gap.

These materials of thermoelectric applications were limited due to small thermal power. In future work, synthesis of Te-doped selenides or new Te-based chalcogenides is the way to increase thermal power that enhances figures of merit ZT. The other future work of our research is to design the structure of lillianite series $L(N, N')$. We hope that varying the thickness of fishbone-like arrangement of the slabs may tune the physical properties.



References

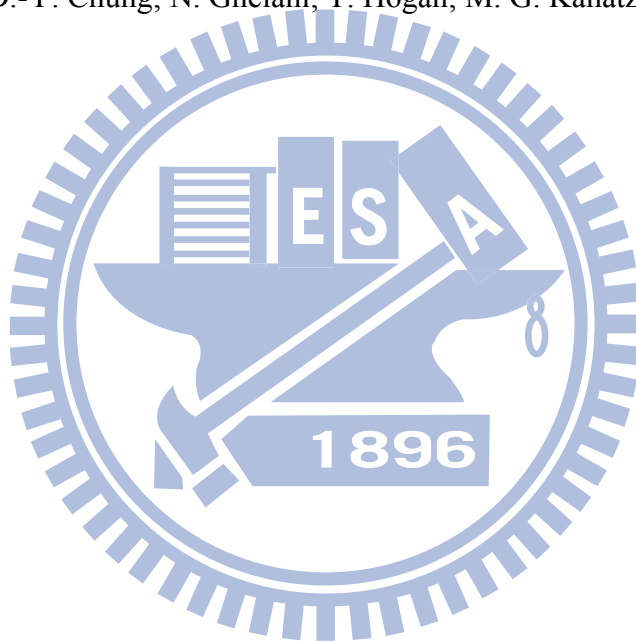
1. D. M. Rowe, *Thermoelectrics Handbook – Macro to Nano*. CRC Taylor & Francis Group: 2006.
2. C. Wood, *Energy Convers. Manage.* **1984**, 24.
3. T. J. Seebeck, *Abhand Deut. Akad. Wiss.* **1822**, (Berlin), 265-373.
4. J. C. Peltier, *Ann. Chem.* **1834**, (LVI), 371-387.
5. W. Thomson, *Proc.Roy.Soc.Edinburgh* **1851**, 91-98.
6. G. J. Snyder; E. S. Toberer, *Nature Mater.* **2008**, 7, 105-114.
7. E. Altenkirch, *Physikalische Zeitschrift* **1909**, 10, 560-580.
8. E. Altenkirch, *Physikalische Zeitschrift* **1991**, 12, 920-924.
9. D. M. Rowe, *CRC Handbook of Thermoelectrics*. Boca Raton, FL :CRC Press: 1995.
10. H. Kawamoto, *Sci. & Technol.* **2009**, 30, 54-69.
11. C. D-Y; M. G. Kanatzidis, *J. AM. CHEM. SOC* **2004**, 126, 6414.
12. D. T. Morelli; T. Caillat; J.-P. Fleurial; A. Borshchevsky; J. Vandersande; B. Chen; C. Uher, *Phys. Rev. B: Condens. Matter Mater. Phys.* **1995**, 51, 9622.
13. G. S. Nolas; D. T. Morelli; T. M. Tritt, *Annu. Rev. Mater. Sci.* **1999**, 29, 89.
14. T. Caillat; A. Borshchevsky; J.-P. Fleurial, *J. Appl. Phys.* **1996**, 80, 4442.
15. K. F. Hsu; S. Loo; F. Guo; W. Chen; J. S. Dyck; C. Uher; T. Hogan; E. K. Polychroniadis; M. G. Kanatzidis, *Science* **2004**, 303, 818.
16. M. S. Dresselhaus; G. Chen; M. Y. Tang; R. G. Yang; H. Lee; D. Z. Wang; Z. F. R. P. Fleurial; P. Gogna, *Materials and Technologies for Direct Thermal-to-Electric Energy Conversion, MRS Symp. Proc.* Materials Research Society Press: 2005.
17. K. F. Hsu; S. Loo; F. Guo; W. Chen; J. S. Dyck; C. Uher; T. Hogan; E. K. Polychroniadis; M. G. Kanatzidis, *Science* **2004**, 303, (5659), 818-821.
18. D.-Y. Chung; T. Hogan; P. Brazis; M. Rocci-Lane; C. Kannewurf; M. Bastea; C. Uher; M. G. Kanatzidis, *Science* **2000**, 287, (5455), 1024-1027.
19. C. L. Condon; S. M. Kauzlarich; T. Ikeda; G. J. Snyder; F. Haarmann; P. Jeglic, *Inorg. Chem.* **2008**, 47, 8204-8212.
20. S. Johnsen; A. Bentien; G. K. Madsen; B. B. Iversen, *Chem. Mater.* **2006**, 18, 4633-4642.
21. S. Johnsen; A. Bentien; G. K. Madsen; B. B. Iversen, *Chem. Mater.* **2006**, 18, 4639-4645.
22. Y. Liang; H. Borrmann; M. Baenitz; W. Schnelle; S. Budnyk; J. T. Zhao; Y. Grin, *Inorg. Chem.* **2008**, 47, 9489-9496.
23. B. C. Sales; D. R. Mandrus; K. Williams, *Science* **1996**, 272, 1325.
24. G. Ferraris; E. Makovicky; S. Merlino, *Crystallography of Modular Materials; International Union of Crystallography Monographs on Crystallography*. Oxford University

Press: Oxford, U.K.: 2004; Vol. 15.

25. S. Anderson; B. G. Hyde, *J. Solid State Chem* **1974**, 9, 92-101.
26. B. Aurivillius, *Ark. Kemi* **1949**, 1, 463-480.
27. B. Frit; J. P. Mercurio, *J. Alloys Compd.* **1992**, 188, 27-35.
28. E. I. Hladyshevsky; K. P. I., *Acta Crystallogr.* **1972**, A28, 97.
29. S. E. Lattuner; M. G. Kanatzidis, *Chem. Commun.* **2003**, 18, 2340-234.
30. Y. Moelo; J. L. Jambor; D. C. Harris, *Can. Mineral* **1984**, 22, 219-226.
31. W. G. Mumme, *Neues Jahrb. Mineral.* **1990**, 5, 193-204.
32. A. Pring; M. Jercher; M. E., *Mineral. Mag.* **1999**, 63, 917-926.
33. J. S. Swinnea; H. Steinfink, *J. Solid State Chem* **1982**, 41, 114-123.
34. M. G. Kanatzidis, *Acc. Chem. Res.* **2003**, 36, 111-119.
35. M. G. Kanatzidis, *Acc. Chem. Res.* **2005**, 38, 359-368.
36. A. Mrotzek; M. G. Kanatzidis, *Inorg. Chem.* **2003**, 42, 7200-7206.
37. J. Takagi; Y. Takeuchi, *Acta Crystallogr. Sect. B: Struct. Sci* **1972**, 28, 649-651.
38. E. Makovicky; S. Karup-Moeller, *Neues Jahrb. Mineral. Abh.* **1977**, 131, 56-82.
39. E. Makovicky; W. G. Mumme; I. C. Madsen, *Neues Jahrb. Mineral. Abh.* **1992**, 10, 454-468.
40. E. Makovicky; S. Karup-Moeller, *Neues Jahrb. Mineral., Abh.* **1977**, 131, 56-82.
41. E. Makovicky, *Neues Jahrb. Mineral., Abh.* **1977**, 131, 187-207.
42. T. J. McCarthy; M. G. Kanatzidis, *Inorg. Chem.* **1995**, 34, 1257-1267.
43. L. Iordanidis; D. Bilic; S. D. Mahanti; M. G. Kanatzidis, *J. Am. Chem. Soc.* **2003**, 125, 13741-13752.
44. K. S. Choi; D. Y. Chung; A. Mrotzek; P. Brazis; C. R. Kannewurf; C. Uher; W. Chen; T. Hogan; M. G. Kanatzidis, *Chem. Mater.* **2001**, 13, 756-764.
45. J. H. Liao; G. A. Marking; K. F. Hsu; Y. Matsushita; M. D. Ewbank; R. Borwick; P. Cunningham; M. J. Rosker; M. G. Kanatzidis, *J. Am. Chem. Soc.* **2003**, 125, 9484-9493.
46. M. Tampier; D. Johrendt, *J. Solid State Chem.* **2001**, 158, 343-348.
47. J. O. Sofo; G. D. Mahan, *Phys. Rev.* **1994**, B49, 4565-4570.
48. F. J. DiSalvo, *Science* **1999**, 285, 703-706.
49. M. G. Kanatzidis, *Semicond. Semimet* **2001**, 69, 51-100.
50. B. G. Hyde; S. Andersson; M. Bakker; C. M. Plug; M. O'Keeffe, *Prog. Solid State Chem.* **1980**, 12, 273-327.
51. S. Misra; H. C. Padhi, *J. Appl. Phys.* **1994**, 75, 4576.
52. C. D. Lokhande; V. S. Yermune; S. H. Pawar, *J. Electrochem. Soc.* **1991**, 138, 624.
53. Y. Takeuchi; J. Takagi; T. Yamanaka, *Proc. Jpn. Acad.* **1974**, 50, 317-321.
54. M. Ohmasa; W. Nowacki, *Z. Kristallogr.* **1973**, 137, 422-432.
55. M. Ohmasa, *Neues Jahrb. Mineral. Monatsh.* **1973**, 227-233.
56. J. H. Kim; D. Y. Chung; D. Bilic; S. Loo; J. Short; S. D. Mahanti; T. Hogan; M. G.

- Kanatzidis, *Chem. Mater.* **2005**, 17, 3606-3614.
57. L. A. Olsen; T. Balić-Zunić; E. Makovicky, *Inorg. Chem.* **2008**, 47, 6756-6762.
58. K. Bente; M. Engel; M. Steins, *Z. Kristallogr.* **1993**, 205, 327-328.
59. H. Sawada; I. Kawada; E. Hellner; M. Tokonami, *Z. Kristallogr.* **1987**, 180, 141-150.
60. Y. Takeuchi; J. Takagi, *Proc. Jpn. Acad.* **1974**, 50, 76-79.
61. H. K. Herbert; W. G. Mumme, *Neues Jahrb. Mineral. Abh.* **1981**, 69-80.
62. S. Karup-Moller; E. Makovicky, *Bull. Geol. Soc. Denmark* **1977**, 26, 41-68.
63. M. F. Wang; S. M. Jang; J. C. Huang; C. S. Lee, *J. Solid State Chem.* **2009**, 182, 1450-1456.
64. M. F. Wang; W. H. Huang; C. S. Lee, *Inorg. Chem.* **2009**, 48, 6402-6408.
65. *SAINTE Version 6.22*. Version 4 ed.; Siemens Analytical X-ray Instruments Inc.: Madison, WI., 2001.
66. *SHELXTL Version 6.10*. Reference Manual; Siemens Analytical X-Ray Systems, Inc.: Madison, WI., 2000.
67. U. D. Altermatt; I. D. Brown, *Acta Crystallogr. Sect. A: Found. Crystallogr.* **1987**, 43, 125-130.
68. O. K. Andersen, *Phys. Rev. B* **1975**, 12, 3060-3083.
69. H. L. Skriver, *The LMTO Method*. Springer: Berlin, 1984.
70. U. van Barth; L. Hedin, *J. Phys. C* **1971**, 4, 2064.
71. P. E. Blöchl; O. Jepsen; O. K. Andersen, *Phys. Rev. B* **1994**, 49, (23), 16223-16233.
72. O. Jepsen; O. K. Andersen, *Z. Phys.* **1995**, 97, 25.
73. R. Dronskowski; P. E. Blöchl, *J. Phys. Chem.* **1993**, 97, 8617-8624.
74. A. Skowron; I. D. Brown, *Acta Crystallogr. Sect. C* **1990**, 46, 2287-2291.
75. S. V. Ovsyannikov; V. V. Shchennikov; A. Y. Manakov; A. Y. Likhacheva; I. F. Berger; A. I. Ancharov; M. A. Sheromov, *Phys. Status Solidi B* **2007**, 244, 279-284.
76. K. A. Agaev; S. A. Semiletov, *Kristallografiya* **1968**, 13, 258-260.
77. K. B. Chen; C. S. Lee, *Solid State Sci.* **2009**, 11, 1666-1672.
78. R. D. Shannon, *Acta Crystallogr., Sect. A: Cryst. Phys., Diffr., Theor. Gen. Cryst.* **1976**, 32, 751-767.
79. R. D. Shannon, *Acta Crystallogr. Sect. A: Cryst. Phys. Diffr. Theor. Gen. Cryst.* **1976**, 32, 751-767.
80. D. I. Bilc; S. D. Mahanti; M. G. Kanatzidis, *Phys. Rev. B* **2006**, 74, (12), 125202.
81. K. A. Agaev; A. G. Talybov; S. A. Semiletov, *Kristallografiya* **1966**, 11, 736-740.
82. A. Sher; I. Odin; A. Novoselova, *Russ. J. Inorg. Chem.* **1986**, 31, 575.
83. B. Palosz; E. Salje, *J. Appl. Crystallogr.* **1989**, 22, 622-623.
84. J. W. Earley, *Am. Mineral.* **1950**, 35, 337-364.
85. E. Y. Atabaeva; S. A. Mashkov; S. V. Popova, *Kristallografiya* **1973**, 18, 173-174.
86. K. Adouby; C. Perez-Vicente; J. C. Jumas, *Z. Kristallogr.* **1998**, 213, 343-349.

87. Y. Iitaka; W. Nowacki, *Acta Crystallogr.* **1962**, 15, 691.
88. G. Weitz; E. Hellner, *Z. Kristallogr.* **1960**, 113, 385-402.
89. A. Skowron; F. W. Boswell; J. M. Corbett; N. J. Taylor, *J. Solid State Chem.* **1994**, 112, 251-254.
90. L. Chang, *Acta Geol. Taiwan* **1987**, 25, 7.
91. A. Mukherjee, *Indian J. Pure Appl. Phys.* **1982**, 20, 681.
92. P. P. K. Smith; B. G. Hyde, *Acta Crystallogr., Sect. C: Cryst. Struct. Commun.* **1983**, 39, 1498-1502.
93. E. Makovicky; W. G. Mumme; I. C. Madsen, *Neues Jahrb. Mineral., Abh.* **1992**, (10), 454-468.
94. J. Sejkora; P. Berlepsch; E. Makovicky; T. Balic-Zunic; J. Litochleb, *Neues Jahrb. Mineral., Abh.* **2002**, 177, 163-180.
95. A. Mroczek; D.-Y. Chung; N. Ghelani; T. Hogan; M. G. Kanatzidis, *Chem. Eur. J.* **2001**, 7.



Appendix

The reactions compound and product identification

No.	Nominocomposition	React. Temp.	Products
1	$\text{Sn}_{10}\text{Bi}_{18}\text{Se}_{37}$	1098 K	$\text{Sn}_{10}\text{Bi}_{18}\text{Se}_{37}$, unknown phase
2	$\text{Sn}_5\text{Bi}_6\text{Se}_{14}$	1098 K	SnSe_2 , $\text{Sn}_3\text{Bi}_2\text{Se}_6$, unknown phase
3	$\text{Sn}_7\text{Bi}_{21}\text{Se}_{37}$	1098 K	Bi_2Se_3 , SnSe_2
4	$\text{Sn}_{5.6}\text{Bi}_{22.4}\text{Se}_{37}$	1098 K	Bi_2Se_3 , unknown phase
5	$\text{Sn}_{14}\text{Bi}_{14}\text{Se}_{37}$	1098 K	SnSe_2 , BiSe , unknown phase
6	$\text{AgSn}_4\text{Bi}_4\text{S}_{10}$	1098 K	SnS , Bi_2S_3
7	$\text{AgPbBi}_3\text{Se}_6$	948 K	AgBiSe_2 , $\text{Pb}_2\text{Bi}_2\text{Se}_5$
8	$\text{AgPb}_4\text{Bi}_4\text{S}_{10}$	1073 K	Bi_2S_3 , AgBi_3S_5 , PbS
9	$\text{AgSnBi}_3\text{Te}_6$	1073 K	AgTe , Bi_2Te_3
10	$\text{AgSn}_4\text{Bi}_4\text{Te}_{10}$	1073 K	AgTe , Bi_2Te_3 , SnTe
11	$\text{AgPbBi}_3\text{Te}_6$	1073 K	AgTe , Bi_2Te_3
12	$\text{AgPb}_4\text{Bi}_4\text{Te}_{10}$	1073 K	PbTe , PbBi_4Te_7
13	$\text{CuSnBi}_3\text{S}_6$	1073 K	Bi_2S_3 , $\text{Cu}_{3.2}\text{Bi}_{4.8}\text{S}_9$
14	$\text{CuSnBi}_3\text{Se}_6$	1073 K	Cu_2Se , $\text{Cu}_{1.6}\text{Bi}_{4.8}\text{Se}_8$
15	$\text{CuSn}_4\text{Bi}_4\text{S}_{10}$	1073 K	SnS , Bi_2S_3
16	$\text{CuSn}_4\text{Bi}_4\text{Se}_{10}$	1073 K	Cu_2Se , $\text{Sn}_{0.571}\text{Bi}_{0.286}\text{Se}$, BiSe
17	$\text{CuSnBi}_3\text{Te}_6$	1073 K	Bi_2Te_3 , SnTe
18	$\text{CuSn}_4\text{Bi}_4\text{Te}_{10}$	1073 K	SnTe , Bi_2Te_3
19	$\text{Sn}_5\text{Bi}_6\text{Te}_{14}$	1073 K	SnTe , Bi_2Te_3
20	$\text{Sn}_3\text{Bi}_2\text{Se}_6$	1073 K	$\text{Sn}_3\text{Bi}_2\text{Se}_6$, SnSe_2
21	$\text{Sn}_3\text{Bi}_2\text{S}_6$	1073 K	Bi_2S_3 , $\text{Bi}_2\text{Sn}_{5-x}\text{S}_9$
22	$\text{Sn}_{18}\text{Bi}_9\text{Se}_{37}$	1073 K	SnSe_2 , BiSe
23	$\text{Sn}_{21}\text{Bi}_7\text{Se}_{37}$	1073 K	SnSe_2 , $\text{Sn}_{0.571}\text{Bi}_{0.286}\text{Se}$, BiSe
24	$\text{Sn}_{22.4}\text{Bi}_{5.6}\text{Se}_{37}$	1073 K	SnSe_2 , SnSe , $\text{Sn}_{0.571}\text{Bi}_{0.286}\text{Se}$
25	$\text{Sn}_2\text{Bi}_2\text{Se}_5$	1073 K	$\text{Sn}_3\text{Bi}_9\text{Se}_{13}$, BiSe , unknown phase
26	$\text{Sn}_2\text{Bi}_2\text{S}_5$	1073 K	SnBi_2S_4 , SnS
27	$\text{Sn}_{10.9}\text{Bi}_{8.8}\text{Se}_{24}$	1073 K	$\text{Sn}_3\text{Bi}_2\text{Se}_6$ pure phase
28	$\text{Sn}_{9.5}\text{Bi}_{10.5}\text{Se}_{24}$	1073 K	$\text{Sn}_3\text{Bi}_2\text{Se}_6$ pure phase
29	$\text{AgSn}_4\text{Bi}_4\text{Se}_{10}$	1073 K	AgBiSe_2 , Bi_2Se_3 , SnSe_2
30	$\text{AgBi}_3\text{S}_5 + \text{SnS}_2 + \text{NaCl}$	1073 K	Bi_2S_3 , SnS

The reactions compound and product identification — *Continued*

No.	React. Formula	React. Temp.	Products
31	$\text{Sn}_3\text{Bi}_2\text{Se}_6$	1073 K quench	$\text{Sn}_3\text{Bi}_2\text{Se}_6$ pure phase
32	$\text{Sn}_3\text{Bi}_2\text{Se}_6 + \text{NaCl}$	1073 K	$\text{Sn}_3\text{Bi}_2\text{Se}_6$, SnSe_2
33	$\text{Sn}_{10.9}\text{Bi}_{8.8}\text{Se}_{24}$	1073 K quench	$\text{Sn}_3\text{Bi}_2\text{Se}_6$ pure phase
34	$\text{AgSnBi}_3\text{S}_6$	1073 K quench	$\text{AgSnBi}_3\text{S}_6$, SnS
35	$\text{Sn}_3\text{Bi}_2\text{S}_6$	1073 K quench	$\text{Sn}_3\text{Bi}_2\text{S}_6$ pure phase
36	$\text{Sn}_{10.9}\text{Bi}_{8.8}\text{S}_{24}$	1073 K quench	$\text{Sn}_3\text{Bi}_2\text{S}_6$ pure phase
37	$\text{AgSnBi}_3\text{Se}_6$	1073 K quench	$\text{Sn}_{0.571}\text{Bi}_{0.286}\text{Se}$, SnSe_2
38	$\text{Pb}_3\text{Bi}_2\text{S}_6$	1073 K quench	$\text{Pb}_6\text{Bi}_2\text{S}_9$, $\text{Pb}_{5.48}\text{Bi}_{2.34}\text{S}_9$
39	$\text{Pb}_{9.5}\text{Bi}_{10.5}\text{S}_{24}$	1073 K	$\text{Pb}_3\text{Bi}_2\text{S}_6$, $\text{Pb}_4\text{Bi}_6\text{S}_{13}$, unknown phase
40	$\text{Sn}_9\text{Bi}_{11}\text{Se}_{24}$	1073 K quench	$\text{Sn}_3\text{Bi}_2\text{Se}_6$, unknown phase
41	$\text{Sn}_8\text{Bi}_{12}\text{Se}_{24}$	1073 K quench	$\text{Sn}_3\text{Bi}_2\text{Se}_6$, unknown phase
42	$\text{Sn}_{13}\text{Bi}_7\text{Se}_{24}$	1073 K quench	$\text{Sn}_{0.571}\text{Bi}_{0.286}\text{Se}$, SnSe_2
43	$\text{Sn}_{14}\text{Bi}_6\text{Se}_{24}$	1073 K quench	$\text{Sn}_{0.571}\text{Bi}_{0.286}\text{Se}$, SnSe_2
44	$\text{Sn}_{12.5}\text{Bi}_{7.5}\text{Se}_{24}$	1073 K quench	$\text{Sn}_{0.571}\text{Bi}_{0.286}\text{Se}$, SnSe_2
45	$\text{Sn}_{11}\text{Bi}_9\text{Se}_{24}$	1073 K quench	$\text{Sn}_3\text{Bi}_2\text{S}_6$ pure phase
46	$\text{Sn}_{9.2}\text{Bi}_{10.8}\text{Se}_{24}$	1073 K quench	$\text{Sn}_3\text{Bi}_2\text{Se}_6$, BiSe
47	$\text{Pb}_{10}\text{Bi}_{10}\text{S}_{24}$	1073 K	$\text{Pb}_3\text{Bi}_2\text{S}_6$ pure phase
48	$\text{Sn}_{10}\text{Bi}_{18}\text{Se}_{37}$	1073 K quench	unknown phase
49	$\text{Sn}_4\text{Bi}_{10}\text{Se}_{19}$	1073 K quench	unknown phase
50	$\text{Sn}_4\text{Bi}_{10}\text{Se}_{19}$	1073 K	unknown phase
51	$\text{Sn}_{9.5}\text{Bi}_{10.5}\text{S}_8\text{Se}_{16}$	1073 K	$\text{Sn}_3\text{Bi}_2\text{Se}_6$, unknown phase
52	$\text{Sn}_{9.5}\text{Bi}_{10.5}\text{S}_8\text{Te}_{16}$	973 K	Bi_2Te_3 , unknown phase
53	$\text{Sn}_{9.5}\text{Bi}_{10.5}\text{Se}_8\text{Te}_{16}$	973 K	$\text{Bi}_4(\text{Te},\text{S})_3$
54	$\text{Sn}_{9.5}\text{Bi}_{10.5}\text{Te}_{24}$	973 K	Bi_4PbTe_7 , Bi_3Te_4
55	$\text{Sn}_4\text{Bi}_6\text{Se}_{13}$	1073 K	unknown phase
56	$\text{Sn}_{10}\text{Bi}_{22}\text{Se}_{43}$	1073 K	unknown phase
57	$\text{Sn}_{10}\text{Bi}_{28}\text{Se}_{52}$	1073 K	unknown phase
58	$\text{Sn}_{10}\text{Bi}_{18}\text{Se}_{37}$	1123 K quench	unknown phase
59	$\text{Sn}_{10}\text{Bi}_{18}\text{Se}_{37}$	1023 K quench	unknown phase
60	$\text{Sn}_{9.5}\text{Bi}_{10.5}\text{S}_{16}\text{Se}_8$	1073 K	$\text{Sn}_3\text{Bi}_2\text{S}_6$, unknown phase
61	$\text{Sn}_{9.5}\text{Bi}_{10.5}\text{S}_8\text{Se}_{16}$	1073 K quench	$\text{Sn}_3\text{Bi}_2\text{Se}_6$ pure phase
62	$\text{Sn}_{10}\text{Bi}_{18}\text{Se}_{37}$	973 K quench	$\text{Sn}_{10}\text{Bi}_{18}\text{Se}_{37}$, unknown phase
63	$\text{Sn}_{9.5}\text{Bi}_{10.5}\text{S}_{16}\text{Se}_8$	1073 K quench	$\text{Sn}_3\text{Bi}_2\text{Se}_6$ pure phase
64	$\text{Sn}_{9.5}\text{Bi}_{10.5}\text{S}_8\text{Te}_{16}$	1073 K quench	unknown phase
65	$\text{Sn}_{9.5}\text{Bi}_{10.5}\text{Se}_8\text{Te}_{16}$	1073 K quench	Bi_2SeTe_2 , Bi_2Se_3

The reactions compound and product identification — *Continued*

No.	React. Formula	React. Temp.	Products
66	$\text{Sn}_{9.5}\text{Bi}_{10.5}\text{Te}_{24}$	1073 K quench	SnTe, Bi_2Te_3
67	$\text{Sn}_{9.5}\text{Bi}_{10.5}\text{S}_{12}\text{Se}_{12}$	1073 K quench	$\text{Sn}_3\text{Bi}_2\text{S}_6$, unknown phase
68	$\text{Sn}_4\text{Bi}_{10}\text{Se}_{19}$	873 K quench	BiSe, SnSe ₂ , unknown phase
69	$\text{Sn}_3\text{Bi}_2\text{Se}_6 + \text{I}_2$	1073 K	$\text{Sn}_3\text{Bi}_2\text{Se}_6$, SnSe ₂
70	$\text{Sn}_{10}\text{Bi}_{18}\text{Se}_{37} + \text{I}_2$	1073 K	SnSe ₂ , Bi_2Se_3
71	$\text{Sn}_4\text{Bi}_{10}\text{Se}_{19} + \text{I}_2$	1073 K	SnSe ₂ , BiSe
72	$\text{Sn}_{9.5}\text{Bi}_{10.5}\text{S}_6\text{Se}_{18}$	1073 K quench	$\text{Sn}_3\text{Bi}_2\text{Se}_6$, unknown phase
73	$\text{Sn}_{10}\text{Bi}_{18}\text{Se}_{37}$	923 K quench	$\text{Sn}_{10}\text{Bi}_{18}\text{Se}_{37}$, unknown phase
74	$\text{Sn}_{10}\text{Bi}_{18}\text{Se}_{37}$	873 K quench	$\text{Sn}_{10}\text{Bi}_{18}\text{Se}_{37}$, unknown phase
75	$\text{Sn}_{10}\text{Bi}_{18}\text{Se}_{37}$	823 K quench	$\text{Sn}_{10}\text{Bi}_{18}\text{Se}_{37}$, unknown phase
76	$\text{Sn}_{9.5}\text{Bi}_{10.5}\text{S}_{24}$	1073 K quench	$\text{Sn}_3\text{Bi}_2\text{S}_6$
77	$\text{Sn}_{10}\text{Bi}_{18}\text{Se}_{37} + \text{I}_2$	923 K	Bi_2Se_3 , SnSe ₂
78	$\text{Sn}_4\text{Bi}_{10}\text{Se}_{19} + \text{I}_2$	923 K	SnSe ₂ , BiSe, unknown phase
79	$\text{Sn}_{9.5}\text{Bi}_{10.5}\text{Se}_{20}\text{Te}_4$	1073 K quench	SnTe, Bi_2Se_3 , SnSe ₂
80	$\text{Sn}_{9.5}\text{Bi}_{10.5}\text{Se}_{22}\text{Te}_2$	1073 K quench	Bi_2Se_3 , SnSe ₂
81	$\text{Sn}_{9.5}\text{Bi}_{10.5}\text{Se}_{23}\text{Te}_1$	1073 K quench	$\text{Sn}_3\text{Bi}_2\text{Se}_6$, SnSe ₂
82	$\text{Sn}_4\text{Bi}_{10}\text{Se}_{19}$	923 K quench	unknown phase
83	$\text{Sn}_4\text{Bi}_{10}\text{Se}_{19}$	873 K quench	unknown phase
84	$\text{Sn}_4\text{Bi}_{10}\text{Se}_{19}$	823 K quench	unknown phase
85	$\text{Sn}_{7.6}\text{Bi}_{20.4}\text{Se}_{38}$	873 K quench	unknown phase
86	$\text{Sn}_{22.8}\text{Bi}_{33.2}\text{Se}_{74}$	873 K quench	$\text{Sn}_{10}\text{Bi}_{18}\text{Se}_{37}$, unknown phase
87	$\text{Sn}_{21.4}\text{Bi}_{34.6}\text{Se}_{74}$	873 K quench	$\text{Sn}_{10}\text{Bi}_{18}\text{Se}_{37}$, unknown phase
88	$\text{Se}_{24.2}\text{Bi}_{31.8}\text{Se}_{74}$	873 K quench	$\text{Sn}_{10}\text{Bi}_{18}\text{Se}_{37}$, unknown phase
89	$\text{Sn}_{4.2}\text{Bi}_{9.8}\text{Se}_{19}$	873 K quench	unknown phase
90	$\text{Sn}_{10.5}\text{Bi}_{9.5}\text{Se}_{24}$	1073 K	$\text{Sn}_3\text{Bi}_2\text{Se}_6$ pure phase
91	$\text{Sn}_{2.3}\text{Pb}_{0.7}\text{Bi}_2\text{Se}_6$	1073 K	$\text{Sn}_3\text{Bi}_2\text{Se}_6$ pure phase
92	$\text{Sn}_{2.3}\text{Pb}_{0.7}\text{Bi}_2\text{Se}_6$	1073 K quench	$\text{Sn}_3\text{Bi}_2\text{Se}_6$ pure phase
93	$\text{Sn}_{2.4}\text{Pb}_{0.8}\text{Bi}_{1.8}\text{Se}_6$	1073 K	$\text{Sn}_3\text{Bi}_2\text{Se}_6$ pure phase
94	$\text{Sn}_{2.4}\text{Pb}_{0.8}\text{Bi}_{1.8}\text{Se}_6$	1073 K quench	$\text{Sn}_3\text{Bi}_2\text{Se}_6$ pure phase
95	$\text{Sn}_{2.5}\text{Pb}_{0.5}\text{Bi}_2\text{Se}_6$	1073 K	$\text{Sn}_3\text{Bi}_2\text{Se}_6$ pure phase
96	$\text{Sn}_{2.7}\text{Pb}_{0.3}\text{Bi}_2\text{Se}_6$	1073 K	$\text{Sn}_3\text{Bi}_2\text{Se}_6$ pure phase
97	$\text{Sn}_{2.1}\text{Pb}_{0.9}\text{Bi}_2\text{Se}_6$	1073 K	$\text{Sn}_3\text{Bi}_2\text{Se}_6$, unknown phase
98	$\text{Sn}_{1.9}\text{Pb}_{1.1}\text{Bi}_2\text{Se}_6$	1073 K	$\text{Sn}_3\text{Bi}_2\text{Se}_6$, unknown phase
99	$\text{Sn}_{2.5}\text{Pb}_{0.9}\text{Bi}_{1.6}\text{Se}_6$	1073 K	$\text{Sn}_3\text{Bi}_2\text{Se}_6$, unknown phase
100	$\text{Sn}_{2.6}\text{Pb}_{1.0}\text{Bi}_{1.4}\text{Se}_6$	1073 K	$\text{Sn}_3\text{Bi}_2\text{Se}_6$, unknown phase

The reactions compound and product identification — *Continued*

No.	React. Formula	React. Temp.	Products
101	$\text{Sn}_{2.7}\text{Pb}_{1.1}\text{Bi}_{1.2}\text{Se}_6$	1073 K	$\text{Sn}_3\text{Bi}_2\text{Se}_6$, unknown phase
102	$\text{Sn}_{3.5}\text{Pb}_{0.5}\text{Bi}_{10}\text{Se}_{19}$	973 K	Bi_2Se_3 , unknown phase
103	$\text{Sn}_3\text{Pb}_1\text{Bi}_{10}\text{Se}_{19}$	973 K	Bi_2Se_3 , PbSe, unknown phase
104	$\text{Sn}_{2.5}\text{Pb}_{1.5}\text{Bi}_{10}\text{Se}_{19}$	973 K	Bi_2Se_3 , PbSe, unknown phase
105	$\text{Sn}_{8.5}\text{Pb}_{1.5}\text{Bi}_{18}\text{Se}_{37}$	973 K	SnSe ₂ , Bi_2Se_3 , BiSe, $\text{Sn}_{10}\text{Bi}_{18}\text{Se}_{37}$
106	$\text{Sn}_7\text{Pb}_3\text{Bi}_{18}\text{Se}_{37}$	973 K	SnSe ₂ , Bi_2Se_3 , BiSe, $\text{Sn}_{10}\text{Bi}_{18}\text{Se}_{37}$
107	$\text{Sn}_{5.5}\text{Pb}_{4.5}\text{Bi}_{18}\text{Se}_{37}$	973 K	SnSe ₂ , Bi_2Se_3 , BiSe, $\text{Sn}_{10}\text{Bi}_{18}\text{Se}_{37}$
108	$\text{Sn}_{2.4}\text{Pb}_{1.0}\text{Bi}_{1.6}\text{Se}_6$	1073 K	SnSe ₂ , PbSe, BiSe
109	$\text{Sn}_{2.4}\text{Pb}_{1.3}\text{Bi}_{1.3}\text{Se}_6$	1073 K	PbSe, SnSe ₂ , BiSe
110	$\text{Sn}_{2.4}\text{Pb}_{1.6}\text{Bi}_{1.0}\text{Se}_6$	1073 K	PbSe, SnSe ₂ , BiSe
111	$\text{Sn}_{2.4}\text{Pb}_{1.9}\text{Bi}_{0.7}\text{Se}_6$	1073 K	PbSe, SnSe ₂ , BiSe
112	$\text{Sn}_{2.4}\text{Pb}_{2.2}\text{Bi}_{0.4}\text{Se}_6$	1073 K	PbSe, SnSe ₂
113	$\text{Sn}_{2.4}\text{Pb}_{0.6}\text{Bi}_2\text{Se}_6$	1073 K	$\text{Sn}_3\text{Bi}_2\text{Se}_6$ pure phase
114	$\text{Sn}_{2.4}\text{Pb}_{0.3}\text{Bi}_{2.3}\text{Se}_6$	1073 K	$\text{Pb}_2\text{Bi}_2\text{Se}_5$, unknown phase
115	$\text{Sn}_{1.7}\text{Pb}_{1.3}\text{Bi}_2\text{Se}_6$	1073 K	PbSe, $\text{Sn}_3\text{Bi}_2\text{Se}_6$
116	$\text{Sn}_{1.4}\text{Pb}_{1.6}\text{Bi}_2\text{Se}_6$	1073 K	PbSe, $\text{Sn}_3\text{Bi}_2\text{Se}_6$
117	$\text{Sn}_{1.1}\text{Pb}_{1.9}\text{Bi}_2\text{Se}_6$	1073 K	PbSe, $\text{Sn}_3\text{Bi}_2\text{Se}_6$
118	$\text{Sn}_{0.8}\text{Pb}_{2.2}\text{Bi}_2\text{Se}_6$	1073 K	$\text{Sn}_3\text{Bi}_9\text{Se}_{13}$, $\text{Sn}_2\text{Pb}_5\text{Bi}_4\text{Se}_{13}$, SnSe
119	$\text{Sn}_{2.9}\text{Pb}_{0.1}\text{Bi}_2\text{Se}_6$	1073 K	$\text{Sn}_3\text{Bi}_2\text{Se}_6$ pure phase
120	$\text{Sn}_{2.07}\text{Pb}_{4.83}\text{Bi}_{4.09}\text{Se}_{13}$	1073 K	$\text{Sn}_2\text{Pb}_5\text{Bi}_4\text{Se}_{13}$
121	$\text{Sn}_2\text{Pb}_5\text{Bi}_4\text{Se}_{13}$	1073 K	$\text{Sn}_2\text{Pb}_5\text{Bi}_4\text{Se}_{13}$
122	$\text{Sn}_{8.48}\text{Pb}_{0.34}\text{Bi}_{4.18}\text{Se}_{15}$	1073 K	$\text{Sn}_{8.5}\text{Pb}_{0.5}\text{Bi}_4\text{Se}_{15}$
123	$\text{Sn}_{8.5}\text{Pb}_{0.5}\text{Bi}_4\text{Se}_{15}$	1073 K	$\text{Sn}_{8.5}\text{Pb}_{0.5}\text{Bi}_4\text{Se}_{15}$, unknown peak
124	$\text{Sn}_2\text{Pb}_5\text{Bi}_4\text{Se}_{13}$ Al ₂ O ₃ tube	1073 K	$\text{Sn}_2\text{Pb}_5\text{Bi}_4\text{Se}_{13}$
125	$\text{Sn}_7\text{Pb}_3\text{Bi}_{18}\text{Se}_{37}$	1003 K	$\text{Sn}_{10}\text{Bi}_{18}\text{Se}_{37}$, unknown phase
126	$\text{Sn}_{8.2}\text{Pb}_{3.4}\text{Bi}_{16.4}\text{Se}_{37}$	873 K quench	$\text{Sn}_{10}\text{Bi}_{18}\text{Se}_{37}$, unknown phase
127	$\text{Sn}_{8.2}\text{Pb}_{3.4}\text{Bi}_{16.4}\text{Se}_{37}$	873 K	$\text{Sn}_{10}\text{Bi}_{18}\text{Se}_{37}$, unknown phase
128	$\text{Sn}_{11}\text{Bi}_{17}\text{Se}_{37}$	873 K quench	$\text{Sn}_{10}\text{Bi}_{18}\text{Se}_{37}$, unknown phase
129	$\text{Sn}_{8.5}\text{Pb}_{1.5}\text{Bi}_{18}\text{Se}_{37}$	873 K quench	$\text{Sn}_{10}\text{Bi}_{18}\text{Se}_{37}$, unknown phase
130	$\text{Sn}_{8.2}\text{Pb}_{1.23}\text{Bi}_{8.57}\text{Se}_{37}$	873 K quench	$\text{Sn}_{10}\text{Bi}_{18}\text{Se}_{37}$, unknown phase
131	$\text{Sn}_{8.2}\text{Pb}_{1.23}\text{Bi}_{8.37}\text{Se}_{37}$	873 K	$\text{Sn}_{10}\text{Bi}_{18}\text{Se}_{37}$, unknown phase
132	$\text{Sn}_2\text{Pb}_5\text{Bi}_4\text{Se}_{13}$ carbon tube	1073 K	$\text{Sn}_2\text{Pb}_5\text{Bi}_4\text{Se}_{13}$
133	$\text{Sn}_{11.4}\text{Bi}_{16.6}\text{Se}_{37}$	873 K quench	$\text{Sn}_{10}\text{Bi}_{18}\text{Se}_{37}$, unknown phase
134	$\text{Sn}_{11.4}\text{Bi}_{16.6}\text{Se}_{37}$	923 K quench	$\text{Sn}_{10}\text{Bi}_{18}\text{Se}_{37}$, unknown phase
135	$\text{Sn}_{8.2}\text{Pb}_{2.0}\text{Bi}_{17.8}\text{Se}_{34}$	903 K quench	$\text{Sn}_{10}\text{Bi}_{18}\text{Se}_{37}$, unknown phase

The reactions compound and product identification — *Continued*

No.	React. Formula	React. Temp.	Products
136	AgGeBi ₃ S ₆	973 K	Bi ₂ S ₃ , AgBi ₃ S ₅ , GeS ₂
137	AgGeBi ₃ Se ₆	973 K	AgBiSe ₂ , Bi ₂ Se ₃ , GeSe ₂
138	AgGeBi ₃ Te ₆	973 K	GeBi ₂ Te ₄ , AgBiTe
139	Sn ₁₆ Bi ₂₆ Se ₅₅	973 K	unknown phase
140	Sn ₁₆ Bi ₂₆ Se ₅₅	973 K quench	unknown phase
141	Sn ₄₆ Bi ₅₄ Se ₁₂₇	973 K	unknown phase
142	Sn ₄₆ Bi ₅₄ Se ₁₂₇	973 K quench	unknown phase
143	Sn ₁₂ Bi ₃₄ Se ₇₃	973 K	unknown phase
144	Sn ₁₂ Bi ₃₄ Se ₇₃	973 K quench	unknown phase
145	Sn ₁₁ Pb ₅ Bi ₂₆ Se ₅₅	973 K	Sn ₃ Bi ₂ Se ₆ , unknown phase
146	Pb ₇ Bi ₄ Se ₁₃	1073 K	PbSe, Bi ₂ Se ₃
147	Sn ₇ Bi ₄ Se ₁₃	1073 K	SnSe ₂ , Sn _{0.571} Bi _{0.286} Se
148	Sn ₂ Pb ₅ Bi ₄ S ₁₃	1073 K	SnBi ₂ S ₄ , Pb _{2.58} Bi _{1.94} S _{5.48}
149	Sn ₂ Pb ₅ Sb ₄ Se ₁₃	1073 K	PbSe, Bi ₂ Se ₃ , Pb _{3.58} Sb _{4.42} Se ₁₀
150	Sn ₂ Pb ₅ Sb ₄ S ₁₃	1073 K	Sn _{1.6} Pb _{1.5} Sb ₈ S ₁₅ , PbSe
151	SnPb ₆ Bi ₄ Se ₁₃	1073 K	Sn ₂ Pb ₅ Bi ₄ Se ₁₃ , unknown phase
152	Sn ₃ Pb ₄ Bi ₄ Se ₁₃	1073 K	Sn ₂ Pb ₅ Bi ₄ Se ₁₃ , unknown phase
153	Sn ₉ Bi ₄ Se ₁₅	1073 K	Sn ₂ BiSe ₄
154	Pb ₉ Bi ₄ Se ₁₅	1073 K	PbSe, Bi ₂ Se ₃
155	Sn _{8.65} Pb _{0.35} Bi ₄ S ₁₅	1073 K	Sn ₁₇ Bi ₆ S ₂₉
156	Sn _{8.65} Pb _{0.35} Sb ₄ Se ₁₅	1073 K	Sn ₄ Sb ₄ Se ₁₀ , SnSe ₂
157	Sn _{8.65} Pb _{0.35} Sb ₄ S ₁₅	1073 K	Sn ₂ Sb ₂ S ₅ , SnS
158	Sn ₂ Pb ₂ Bi ₂ Se ₇	1023 K	Sn _{6-x} Pb _x Bi ₄ Se ₉ , unknown phase
159	SnPb ₃ Bi ₂ Se ₇	1023 K	Sn _{6-x} Pb _x Bi ₄ Se ₉ , unknown phase
160	Pb ₄ SbBiSe ₇	1023 K	Sn _{6-x} Pb _x Bi ₄ Se ₉ , unknown phase
161	Sn ₃ PbBi ₂ Se ₇	1023 K	Sn _{6-x} Pb _x Bi ₄ Se ₉ , unknown phase
162	Sn ₃ Pb ₈ Bi ₄ Se ₁₇	1023 K	Sn _{6-x} Pb _x Bi ₄ Se ₉ , unknown phase
163	Sn ₈ Pb ₃ Bi ₄ Se ₁₇	1023 K	Sn _{6-x} Pb _x Bi ₄ Se ₉ , unknown phase
164	Pb ₁₁ Bi ₂ Sb ₂ Se ₁₇	1023 K	PbSe, Bi ₂ Se ₃
165	Sn ₆ Pb ₅ Bi ₄ Se ₁₇	1023 K	Sn _{6-x} Pb _x Bi ₄ Se ₉ , unknown phase
166	Sn ₃ Pb ₂ Bi ₂ Se ₈	1023 K	Sn _{6-x} Pb _x Bi ₄ Se ₉ , unknown phase
167	Sn ₄ PbBi ₂ Se ₈	1023 K	Sn _{6-x} Pb _x Bi ₄ Se ₉ , unknown phase
168	SnPb ₄ Bi ₂ Se ₈	1023 K	Sn _{6-x} Pb _x Bi ₄ Se ₉ , unknown phase
169	Pb ₅ SbBiSe ₈	1023 K	unknown phase
170	Pb ₁₃ Bi ₂ Sb ₂ Se ₁₉	1023 K	PbSe

The reactions compound and product identification — *Continued*

No.	React. Formula	React. Temp.	Products
171	Pb ₁₃ Bi ₂ Sb ₂ S ₁₉	1023 K	PbS
172	Pb ₁₃ Bi ₂ Sb ₂ Te ₁₉	1023 K	PbTe
173	Pb _{13.08} Bi _{1.87} Sb _{2.13} S ₁₉	1023 K	PbS
174	Pb _{13.08} Bi _{1.87} Sb _{2.13} Se ₁₉	1023 K	PbSe
175	Pb _{13.08} Bi _{1.87} Sb _{2.13} Te ₁₉	1023 K	PbTe
176	Sn ₁₃ Bi ₂ Sb ₂ Se ₁₉	1023 K	SnSe, Bi ₂ Se ₃
177	Pb _{12.31} Bi _{2.56} Sb _{2.13} Se ₁₉	1023 K	PbSe, Bi ₂ Se ₃
178	Pb _{10.75} Bi _{4.12} Sb _{2.13} Se ₁₉	1023 K	Pb ₁₂ Bi ₂ Sb ₂ Se ₁₉ , Se, BiSe
179	Pb _{8.96} Bi _{5.91} Sb _{2.13} Se ₁₉	1023 K	Pb ₁₂ Bi ₂ Sb ₂ Se ₁₉ , Se, BiSe
180	Pb _{7.28} Bi _{7.58} Sb _{2.13} Se ₁₉	1023 K	Pb ₁₂ Bi ₂ Sb ₂ Se ₁₉ , Se, BiSe
181	Pb _{5.71} Bi _{9.14} Sb _{2.13} Se ₁₉	1023 K	Pb ₁₂ Bi ₂ Sb ₂ Se ₁₉ , Se, BiSe
182	Pb ₁₀ Bi ₅ Sb ₂ Se ₁₉	1023 K	Pb ₁₂ Bi ₂ Sb ₂ Se ₁₉ , Se, BiSe
183	Pb ₁₁ Bi ₄ Sb ₂ Se ₁₉	1023 K	Pb ₁₂ Bi ₂ Sb ₂ Se ₁₉ , BiSe, PbSe
184	Pb _{10.5} Bi _{4.5} Sb ₂ Se ₁₉	1023 K	Pb ₁₂ Bi ₂ Sb ₂ Se ₁₉ , Se, BiSe
185	Pb ₁₃ Bi ₄ Se ₁₉	1023 K	PbSe
186	Pb ₁₃ Bi ₃ SbSe ₁₉	1023 K	PbSe
187	Pb ₁₃ BiSb ₃ Se ₁₉	1023 K	PbSe
188	Pb ₁₃ Sb ₄ Se ₁₉	1023 K	PbSe
189	Sn _{10.5} Bi _{4.5} Sb ₂ Se ₁₉	1023 K	SnSe, Sb ₂ Se ₃
190	Sn ₈ PbBi ₄ Se ₁₅	1073 K	Sn ₃ Bi ₉ Se ₁₃ , SnSe
191	Sn ₆ Pb ₃ Bi ₄ Se ₁₅	1073 K	Sn ₃ Bi ₉ Se ₁₃ , SnSe
192	Sn ₃ Sb _{0.1} Bi _{1.9} Se ₆	1023 K	SnSe, BiSe, Sn _{0.57} Bi _{0.286} Se
193	Sn ₃ Sb _{0.3} Bi _{1.7} Se ₆	1023 K	SnSe, BiSe, Sn _{0.57} Bi _{0.286} Se
194	Sn ₃ Sb _{0.5} Bi _{1.5} Se ₆	1023 K	SnSe, BiSe, Sn _{0.57} Bi _{0.286} Se
195	Sn ₃ Sb _{0.7} Bi _{1.3} Se ₆	1023 K	SnSe, Sn ₄ Sb ₄ Se ₁₀
196	Sn _{3.26} Pb _{8.74} Bi ₄ Se ₁₈	1023 K	Sn _{6-x} Pb _x Bi ₄ Se ₉ pure phase
197	Sn ₆ Pb ₆ Bi ₄ Se ₁₈	1023 K	Sn _{6-x} Pb _x Bi ₄ Se ₉ pure phase
198	Sn _{8.52} Pb _{3.48} Bi ₄ Se ₁₈	1023 K	Sn _{6-x} Pb _x Bi ₄ Se ₉ pure phase
199	Pb ₁₂ Bi ₄ Se ₁₈	1023 K	PbSe, BiSe
200	Sn ₆ Pb ₆ Bi ₄ Se ₁₈	1023 K	Sn _{6-x} Pb _x Bi ₄ Se ₉ pure phase
201	Sn ₇ Pb ₅ Bi ₄ Se ₁₈	1023 K	Sn _{6-x} Pb _x Bi ₄ Se ₉ pure phase
202	Sn _{2.26} Pb _{9.74} Bi ₄ Se ₁₈	1023 K	Sn _{6-x} Pb _x Bi ₄ Se ₉ , unknown phase
203	Sn _{1.26} Pb _{10.74} Bi ₄ Se ₁₈	1023 K	Sn _{6-x} Pb _x Bi ₄ Se ₉ , unknown phase
204	Sn ₁₂ Bi ₄ Se ₁₈	1023 K	Sn _{6-x} Pb _x Bi ₄ Se ₉ pure phase
205	Sn _{3.26} Pb _{8.74} Bi ₄ Se ₁₈	1023 K	Sn _{6-x} Pb _x Bi ₄ Se ₉ , PbSe

The reactions compound and product identification — *Continued*

No.	React. Formula	React. Temp.	Products
206	$\text{Sn}_9\text{Pb}_4\text{Bi}_4\text{Se}_{18}$	1023 K	$\text{Sn}_{6-x}\text{Pb}_x\text{Bi}_4\text{Se}_9$ pure phase
207	$\text{Sn}_{10}\text{Pb}_2\text{Bi}_4\text{Se}_{18}$	1023 K	$\text{Sn}_{6-x}\text{Pb}_x\text{Bi}_4\text{Se}_9$ pure phase
208	$\text{Sn}_2\text{Pb}_{10}\text{Bi}_4\text{Se}_{18}$	1023 K	$\text{Sn}_{6-x}\text{Pb}_x\text{Bi}_4\text{Se}_9$, PbSe
209	$\text{Sn}_{11}\text{Pb}_1\text{Bi}_4\text{Se}_{18}$	1023 K	$\text{Sn}_{6-x}\text{Pb}_x\text{Bi}_4\text{Se}_9$ pure phase
210	$\text{Sn}_{5.5}\text{Pb}_{6.5}\text{Bi}_4\text{Se}_{18}$	1023 K	$\text{Sn}_{6-x}\text{Pb}_x\text{Bi}_4\text{Se}_9$ pure phase
211	$\text{Sn}_5\text{Pb}_7\text{Bi}_4\text{Se}_{18}$	1023 K	$\text{Sn}_{6-x}\text{Pb}_x\text{Bi}_4\text{Se}_9$ pure phase
212	$\text{Sn}_{4.5}\text{Pb}_{7.5}\text{Bi}_4\text{Se}_{18}$	1023 K	$\text{Sn}_{6-x}\text{Pb}_x\text{Bi}_4\text{Se}_9$ pure phase
213	$\text{Sn}_4\text{Pb}_8\text{Bi}_4\text{Se}_{18}$	1023 K	$\text{Sn}_{6-x}\text{Pb}_x\text{Bi}_4\text{Se}_9$ pure phase
214	$\text{Sn}_3\text{Pb}_9\text{Bi}_4\text{Se}_{18}$	1023 K	$\text{Sn}_{6-x}\text{Pb}_x\text{Bi}_4\text{Se}_9$, unknown phase
215	$\text{Sn}_2\text{Pb}_{10}\text{Bi}_4\text{Se}_{18}$	1023 K	$\text{Sn}_{6-x}\text{Pb}_x\text{Bi}_4\text{Se}_9$, unknown phase
216	$\text{Sn}_{2.67}\text{Bi}_{2.26}\text{Se}_6$	1023 K	$\text{Sn}_3\text{Bi}_2\text{Se}_6$ pure phase
217	$\text{Sn}_{2.74}\text{Bi}_{2.26}\text{Se}_6$	1023 K	$\text{Sn}_3\text{Bi}_2\text{Se}_6$ pure phase
218	$\text{Sn}_{0.5}\text{Pb}_{2.5}\text{Bi}_2\text{Se}_6$	1073 K	$\text{Sn}_2\text{Pb}_5\text{Bi}_4\text{Se}_{13}$, unknown phase

